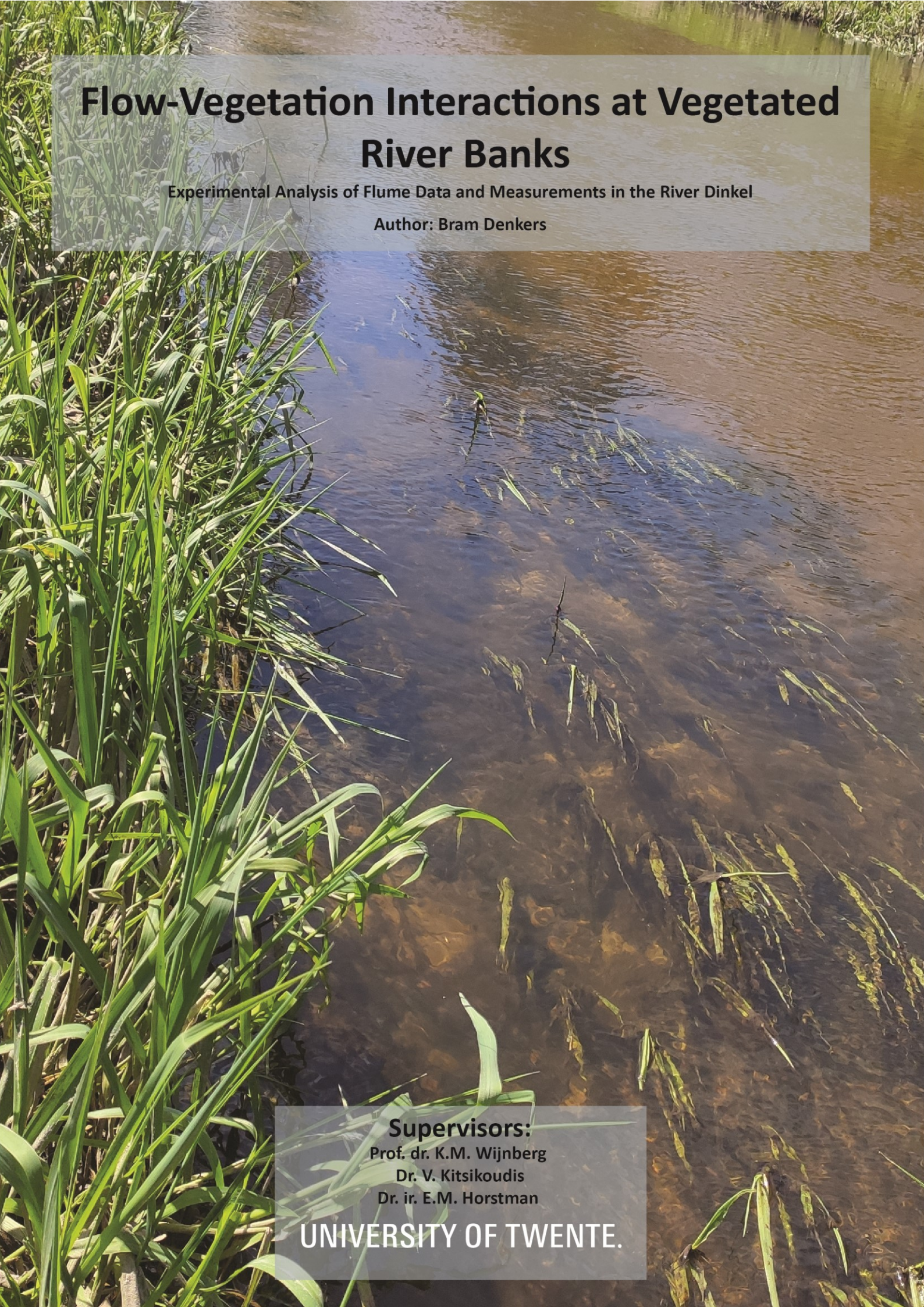

Flow-Vegetation Interactions at Vegetated River Banks

Experimental Analysis of Flume Data and Measurements in the River Dinkel

Author: Bram Denkers

Supervisors:
Prof. dr. K.M. Wijnberg
Dr. V. Kitsikoudis
Dr. ir. E.M. Horstman

UNIVERSITY OF TWENTE.

Flow-Vegetation Interactions at Vegetated Riverbanks

Experimental Analysis of Flume Data and Measurements in the River Dinkel

By

Bram Denkers

To obtain the degree of Master of Science at the University of Twente,
to be defended publicly on 29 August 2023.

Daily Supervisors	Dr. V. Kitsikoudis (Vasileios) Dr. ir. E.M. Horstman (Erik)
Head Graduation Committee	Prof. dr. K.M. Wijnberg (Kathelijne)
Institution	University of Twente - Faculty of Engineering Technology
Department	Civil Engineering and Management (CEM)
Chair	Marine and Fluvial System - Coastal Systems and Nature-Based Engineering
Document Version	Final Version (21/08/2023)
Project Duration	February 2023 – Augustus 2023

Cover Image: Bram Denkers - Vegetated Riverbanks of the Dinkel near Glane.

Summary

Riverbank vegetation has numerous positive effects on water quality, biodiversity and riverbank stability. However, it could also obstruct natural water flow and thereby contribute to flooding. To make informed decisions on the management of riverbank vegetation in natural streams, it is crucial to understand the complex flow-vegetation interaction. Previous research into flow-vegetation interactions has mostly relied on simplified laboratory experiments, which may not fully represent real-world conditions. Therefore, further investigation is needed to accurately study and compare the flow dynamics within and around natural riverbank vegetation in order to inform better management practices. Furthermore, this study aims to investigate the representativeness of the idealised derived formulae from flume studies when applied under real-world conditions.

In order to get insight into the effect of the spatial configuration of flexible vegetation patches in a flume on the longitudinal and cross-sectional development of the mean flow velocities, the flow in and around two submerged macrophytes species, *Callitriche platycarpa* (dense patch) and *Groenlandia densa* (sparse patch) were analysed to investigate the flow-vegetation interaction in aquatic habitats. The frontal area per canopy volume, which represents the ratio of the cross-sectional area of the vegetation patch perpendicular to the flow direction to the volume of the vegetation patch, is 7.70 and 1.30 for the dense and sparse patch, respectively. Two different spatial configurations were considered with two vegetation patches. The first one was the aligned configuration, representing riverbank vegetation with the two patches of vegetation positioned at the sides of the flume. The second configuration was the staggered configuration, representing the interaction of riverbank vegetation with instream vegetation patches. The findings of this flume study emphasize the importance of considering the interaction of different vegetation patches when studying the flow-vegetation dynamics in natural aquatic habitats, as the spatial configuration of two vegetation patches affects the wake development and the recovery downstream of a vegetation patch. Furthermore, the flume study underlines that two vegetation patches within 0.9 meters close to each other do not necessarily mean that they act hydrodynamically as one vegetation patch.

A field study at the vegetated riverbanks of the River Dinkel was performed to investigate the flow-vegetation interaction under natural conditions and to test the representativeness of idealised derived formulae from flume studies. The flow was measured at three different riverbank vegetation patches. Patches of two different macrophyte species were found; two patches consisted of *Carex sylvatica* with a frontal area per canopy volume of 1.69 and 1.30, and one patch consisted of the *Sparganium emersum* with a frontal area per canopy volume of 2.94. The flow-vegetation interaction measurements performed in the Dinkel show that the density of the riverbank vegetation affects the flow velocity and turbulence within the vegetation patch and across the river cross-section. A shear layer formed between the slow flow within the riverbank vegetation and the faster flow in the open channel, where Kelvin-Helmholtz vortices could manifest when the shear layer has a strong enough velocity gradient. Normalized transverse flow velocity fluctuations and frequency analysis revealed the manifestation of coherent Kelvin-Helmholtz vortices. Large horizontal Kelvin-Helmholtz vortices were visible in the power density spectra of transverse flow velocity fluctuations. These Kelvin-Helmholtz vortices made a significant contribution to the transverse turbulent shear stress. The distribution of transverse flow velocity and Reynolds shear stresses revealed an inflection point, which may not align with the riverbank vegetation edge. Furthermore, the growth of the size of the vortices outside of the vegetation patch is not influenced by the characteristics of the vegetation patch itself. Quadrant analysis of Reynolds shear stress highlighted the dominance of sweeps and ejections in momentum exchange and turbulent shear stresses.

Lastly, the applicability and representativeness of some idealised derived formulae were tested on the field data. This study evaluated the performance of the two layered vortex-based model of White and Nepf (2008) and the hybrid eddy viscosity model developed by Truong and Uijttewaal (2019) for predicting transverse momentum exchange, and the analytical exponential-based model proposed by Liu et al. (2022) for predicting the lateral streamwise flow velocity profile. This comparison showed that the vortex-based model of White and Nepf (2008) demonstrates relatively accurate results but tends to overestimate lateral momentum exchange near inflection points and within the riverbank vegetation patch. The hybrid eddy viscosity model by Truong and Uijttewaal (2019) effectively captures transverse momentum exchange. The existing analytical exponential-based model proposed by Liu et al. (2022) demonstrates good predictions when utilizing directly derived mixing layers widths from the flow velocity measurements in the field. However, the model performed inadequately when using the empirical estimates of the mixing layer widths proposed by White and Nepf (2008) and Liu et al. (2022). The limitation of the hybrid eddy viscosity model is that is relies on actual flow velocity measurements. To overcome this limitation, one potential approach is to utilize the exponential-based model by Liu et al. (2022) as input for the hybrid eddy viscosity model. This combination shows reasonable results but has a much more significant potential for a better understanding of flow-vegetation interactions without performing actual flow velocity measurements. However, the performance of the empirical relationships in both the exponential-based model and the hybrid eddy viscosity model highlights the need for further research to establish better empirical relationships for the mixing layer widths under natural circumstances and without performing actual flow measurements. Previous studies that derived the empirical formulae are, to a great extent, under the influence of many idealizations. For instance, in these studies, relatively dense rigid cylinders are used as mimics for vegetation patches on a flatbed without any bedforms and with relatively uniform transverse flow conditions.

Table of Contents

List of Symbols

a	Frontal area per canopy volume	ρ	Water density
a_d	Depth-averaged frontal area per canopy volume	Re_d	Stem Reynolds number
A_p	The frontal area of the plant surface	s_f	The standard deviation of the function
α	Fischer constant	$s_{x,y}$	The standard deviation of variables x and y
b	Vegetation patch width	S	Water surface slope
β	Proportionality constant	S_i	Contribution ratio of different quadrants
C	Chèzy coefficient	St	Strouhal number
C_d	Drag coefficient	τ_{xy}	Transverse shear stress
c_f	Bed friction	$u(t)$	Instantaneous streamwise velocity
C_t	Constant of proportionality	$u'(t)$	Instantaneous turbulent streamwise fluctuations
d	Cylindrical diameter / Vegetation stem diameter	$\overline{u}$	Time-averaged streamwise velocity
δ	Total mixing width (inner and outer layer)	$\overline{U}$	The arithmetic mean of the time-averaged velocities in the vegetated and the non-vegetated zone
δ_e	Vertical penetration depth into submerged vegetation	$\overline{u'v'}$	Time-averaged streamwise and transverse velocity temporal fluctuation
δ_I	Penetration depth into the vegetation	U	Depth-averaged velocity
δ_O	Penetration depth into the bare channel	U_m	Flow velocity at the matching point
f	The dominant vortex shedding frequency	U_s	Slip velocity
F_d	Drag force	U_0	Mean upstream streamwise flow velocity
g	Gravitational constant	U_1	Steady depth-averaged streamwise velocity in the vegetation patch

h	Water depth	U_2	Steady depth-averaged streamwise velocity in the bare channel
h_c	Water depth bare channel	$U_{1(f)}$	Steady velocity in the fully developed flow region
h_f	Water depth floodplain	$U_{1(0)}$	Flow velocity at the leading edge
h_m	Mean water level	ΔU	The velocity difference between the time-averaged in the vegetated and the non-vegetated zone.
h_r	The fraction between water depth in the bare channel and floodplain	u_*	Friction velocity
h_v	Vegetation height	u_*^2	Maximum shear velocity
κ	Von Karman constant	SD	Standard Deviation
k_s	Nikurandse Roughness	x	Longitudinal coordinate (positive in the downstream direction)
λ	Shear parameter	x_d	Interior adjustment Length
λ_f	Frontal area per unit bed area	y	Lateral coordinate (positive towards the middle of the channel)
$L_{d(bare)}$	e-folding length scale for the depth-averaged velocity in the bare channel	y_m	Matching point
$L_{d(veg)}$	e-folding length scale for the depth-averaged velocity in the vegetation patch	γ	Vogel exponent
n	Shoots per m^2	z	Vertical coordinate (positive upwards from the water surface)
ν	Kinematic viscosity of water	z_0	Roughness length
ν_I	Inner layer eddy viscosity	ϕ	Solid volume fraction
ν_O	Outer layer eddy viscosity	ΔS	Averaged spacing between vegetation elements
ν_t	Theoretical Eddy viscosity	θ	Momentum Thickness

Preface

Before you lies my Master Thesis, "*Flow-Vegetation Interactions at Vegetated Riverbanks: Experimental Analysis of Flume Data and Measurements in the River Dinkel"*. This research was carried out to fulfil the graduation requirements for the degree of Master of Science in Civil Engineering and Management. This research was carried out within the Water Engineering & Management department of the University of Twente in Enschede.

First of all, I would like to take this opportunity to express a special thanks to my supervisors, Loreta Cornacchia and Vasileios Kitsikoudis. Presenting this thesis would not have been possible without the excellent guidance and expertise of both of you. I really enjoyed our weekly meetings, in which your enthusiasm and proactively providing new insights for my research kept me motivated throughout my research. Furthermore, I want to thank Erik Horstman and Kathelijne Wijnberg for all your constructive feedback during the preparation as well as during the actual research. Additionally, I want to acknowledge the excellent work of Emre Ozturk and Anna Loboda during the field trips; without this excellent construction advice for the measurement frame, I would not have been able to carry out this research. Last but not least, I would like to thank my family and friends for always supporting me during my study time.

Finally, I hope you will find as much enjoyment in reading my thesis as I did in conducting this research.

Bram Denkers
Enschede, 21 August 2023

1 Introduction

Riverbank vegetation has a wide range of positive effects on aquatic ecosystems. The first positive effect of the interaction between vegetation and hydrodynamics is that it regulates and improves the water quality by the uptake of high nitrogen and phosphorus concentration from the water column (Clarke, 2002; Cornacchia et al., 2019). Besides that, riverbank vegetation could create different habitats with variable flow velocities and water depths, thereby promoting the living environment's heterogeneity and biodiversity (Fraaije et al., 2019). Lastly, riverbank vegetation could reduce the riverbed's erosion and enhance the riverbank stability (Liu et al., 2017).

However, there are also downsides to the presence of vegetation in many natural ecosystems. Aquatic vegetation acts as an obstruction to the natural water flow. The additional vegetation-induced drag decreases the discharge capacity of the natural water flow, resulting in higher water levels (Liu et al., 2008). For example, in combination with high rainfall intensities, this could lead to water management problems such as floods.

In order to make a trade-off between the benefits and drawbacks of vegetation in natural streams, a better understanding of the effects of natural vegetation on hydrodynamics is needed. Generally, natural aquatic vegetation contributes to the transformation of the vegetated channel into a more complex hydrodynamic structured flow due to the irregular morphology and flexibility of plants (Nepf, 2012c). However, most of the research describing the flow-vegetation interactions has been carried out under idealised circumstances in laboratory flume experiments (e.g., Huai et al., 2019; White and Nepf, 2007). In such laboratory flume experiments, the vegetation has been mainly represented as artificial rigid cylinders, and the flow is uniform and steady on a non-erodible flatbed. Of course, such simplifications do not represent vegetation in natural streams (Aberle and Järvelä, 2015).

Despite the recent advances in describing the flow-vegetation interaction in laboratory experiments, the hydrodynamic variability of the flow field within and around vegetation in natural streams is still uncertain. Using parameterisations of idealised flume experiments can lead to significant uncertainties in describing the hydrodynamics in the field. For example, Horstman et al. (2018) have shown that arrays of natural mangrove pneumatophores show differences in canopy flow dynamics compared to artificial rigid mimics. Furthermore, simplifications such as using uniform rigid elements or the spacing of individual elements within a patch have been shown to bias the outcomes when compared to field experiments. This bias may hide or exaggerate some essential physical processes observed in natural conditions (Tinoco et al., 2020). The representativeness and comparison of the hydrodynamic processes in laboratory experiments have not yet been explored for natural vegetated streams. In order to be able to compare and test the representativeness of these simplifications in laboratory experiments, a better understanding of the flow within and around natural riverbank vegetation is required.

1.1 Background

Vegetation found along channel banks, rivers, and floodplain areas is often composed of woody deciduous trees and shrubs of grass, with branches and leaves heterogeneously distributed over the height. The flow around this vegetation type is rather complex as plants have different morphologies, flexibilities and densities, influencing the water flow differently. Furthermore, natural plants often grow together into well-defined regions called patches (Forman, 1995; Rowiński and Radecki-Pawlik, 2015). The term ‘patch’ is used in aquatic ecology to distinguish a well-defined region of individual aquatic plants with a high density from the surrounding bare area (Schoelynck et al., 2018). However, in the case of riverbank vegetation, the delineation of vegetation patches is less straightforward. For example, patches of single or multiple species do not have a sharp edge of shoot density with their

surroundings, or two more patches of the same or different species could grow separately but act hydrodynamically as one vegetation patch (Kolasa, 2014). This research defines a distinct vegetation patch as one delineated vegetation patch or multiple patches that are closely acting hydrodynamically as one patch (Figure 1).

Figure 1 Example of a delineated emergent riverbank vegetation patch consisting of two patches acting hydrodynamically as one patch. Adapted from Schoelynck et al. 2018.

The characteristics of vegetation patches, such as the width, length, height and density, influence the vegetation-induced drag and alter the (turbulent) velocity field across several scales. These scales range from individual branches and blades of a single plant to a community of vegetation patches. In any case, the flow alteration effects are always relative to these vegetation characteristics and the different length scales (Nepf, 1999, 2012c).

The vegetation in riverbanks is quite diverse and morphologically variable over the river-cross section (Figure 2). Different vegetation types periodically interact with the flow when high water or floods occur. The focus of this research will be on the riverbank and near-bank vegetation patches in the lower parts of the floodplains and the main channel, which are, in general, populated by shrubby woody and grassy types of emergent and submerged vegetation (Caroppi and Järvelä, 2022).

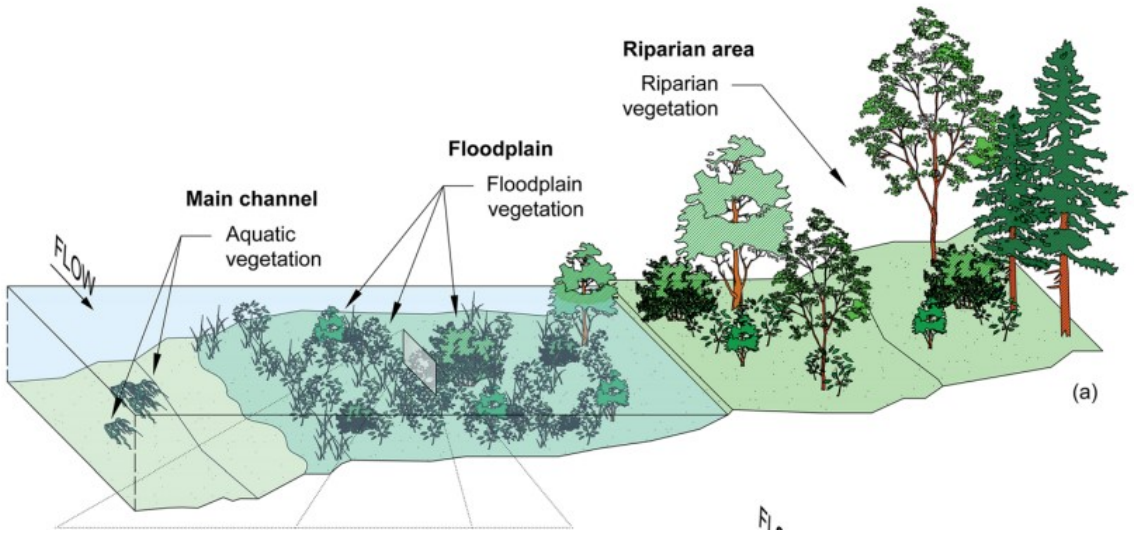

Figure 2 Conceptualisation of geomorphic and vegetation features of a river-cross section during high-flow conditions. Taken from Caroppi and Järvelä (2022).

The distribution of the frontal canopy area determines the flow drag and the mean flow alteration (Nepf, 2012a). As river-type vegetation is so complex, its spatial and seasonal variabilities make it challenging to capture a single canopy frontal area. Therefore, a general upfront species-specific parametrisation does not exist and should be determined at the site of interest (Kalloe et al., 2022).

Patches of vegetation create distinctively different large-scale flow patterns depending on the density of the patch or the total surface area that is covered by plants (Nepf, 2012c). The current metrics that are in use to characterise vegetation are coming from idealized flume experiments in which arrays of rigid cylinders are used to mimic a natural vegetation patch (Plew, 2010). The geometry of such a patch is described by the characteristic frontal area per unit of vegetation volume (a) or the solid volume fraction (ϕ). These parameters will be further elaborated in the Theoretical Framework (Section 2.1).

Natural vegetation is not entirely rigid but has a certain flexibility and non-uniformity over its height. The flexibility introduces an ability of plants to be pushed over by the flow and thus shows a reconfiguration of their original morphology in a more streamlined condition. This property has a significant effect on the characteristics frontal area of the vegetation and the associated reduction of drag (de Langre, 2008; Jalonen and Järvelä, 2014; Vogel, 2020; Yagci et al., 2016). Experimental laboratory studies show that the effects of inclination into a more streamlined position and the non-uniformity of tree-like vegetation types suppress the formation of stem-scale and wake-turbulence (Kitsikoudis et al., 2016, 2017). To conclude, ordinary vegetation parameterisations used in most flume experiments with rigid cylinders could therefore be insufficient to describe the flow-vegetation interactions in the case of flexible natural vegetation.

1.2 State of the Art

Recent studies have revealed that the use of rigid or cylindrical elements in describing hydrodynamics in the field can introduce biases by either hiding or amplifying the hydrodynamic processes when trying to reproduce the relevant natural physical processes in laboratory experiments (Horstman et al., 2018; Tinoco et al., 2020). This literature review will therefore focus on the existing idealised models and the capabilities of these models in predicting the flow-vegetation interaction in the case of natural riverbank vegetation.

Different experiments and case studies found that the uniform flow conditions of an open channel transform into a more complex turbulent structured flow in both the horizontal and the vertical directions due to vegetation patches in general (Siniscalchi et al., 2012; Sukhodolov and Sukhodolova, 2009). Nepf (2012a) shows that the mean turbulence intensity inside the vegetation patches generally increases with increasing vegetation density. In addition, the flow velocity differences between the open channel flow and the flow through the vegetation also increase. However, the turbulence levels may be damped for very dense patches and become even lower than the turbulence intensities in comparable open channel flow without vegetation (Nepf, 2012a). The flow velocity difference between the slower flow velocity in the vegetated zone and the faster flow in the main channel leads to the formation of a flow velocity gradient and the formation of shear layers (Caroppi et al., 2021). The shear layers, due to these velocity differences, are often characterised by the formation of large coherent structures (shear-induced vortices) in the horizontal plane (Figure 3) (White and Nepf, 2007) and the vertical plane in case of submerged vegetation (Figure 4), as there is a drag discontinuity in both planes resulting in an inflectional velocity profile and the formation of the shear-induced vortices (Ghisalberti and Nepf, 2002; White and Nepf, 2007).

In natural streams, riverbank vegetation often grows in spatially heterogeneous patches, creating a long region of vegetation with a certain width (Sand-Jensen and Vindbaek Madsen, 1992). An emergent vegetation patch along the sidewall provides a relatively high drag compared to a bare flat riverbed

(Figure 3), leading to the deflection of the flow approaching from upstream around the vegetation patch because of an abrupt spanwise variation in roughness (Zong and Nepf, 2010). This horizontal deflection already starts at the upfront of the patch and creates an interior adjustment region ($x < x_d$) within the vegetation patch. The streamwise flow velocity in the vegetation patch decreases exponentially in this interior adjustment region (Liu et al., 2020). The length of this adjustment region scales with the patch density and the patch width (Rominger and Nepf, 2010). The flow velocity variation between the flow velocity within the vegetation patch (U_1) and the open channel (U_2) results in the development of a shear layer between the slow flow through the vegetation and the fast-flowing deflected flow. After the adjustment region ($x > x_d$), Kelvin-Helmholtz vortices will form along the lateral edge between the vegetated and the non-vegetated areas if the flow velocity difference is significant enough (Caroppi et al., 2020). According to Caroppi et al. (2020), the occurrence of Kelvin-Helmholtz vortices is defined by the shear parameter (λ) which is based on the steady depth-averaged velocity in the open channel and the vegetated zone (Equation 1).

$$\lambda \left(= \frac{U_2 - U_1}{U_2 + U_1} \right) \geq 0.4 \tag{1}$$

These Kelvin-Helmholtz vortices dominate the mass and momentum exchange between the vegetated and the adjacent open channel flow. In the last stage ($x \gg x_d$), the mean transverse flow velocity distribution against stabilises in the longitudinal direction ($\partial \mathrm{U} / \partial \mathrm{x} = 0$). The adjustment distance is essential from a practical engineering perspective as it indicates the longitudinal effect of a particular vegetation patch.

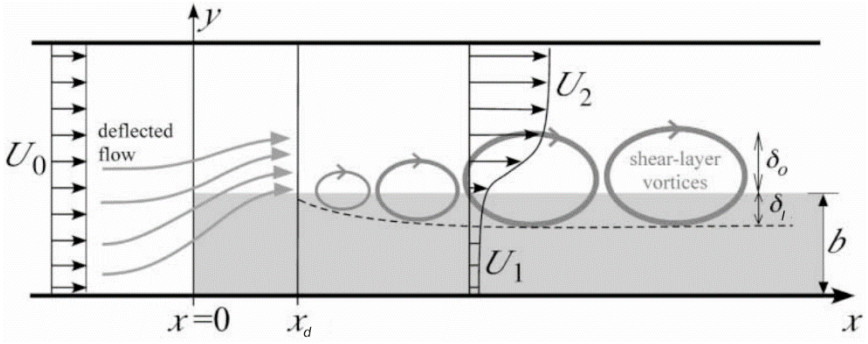

Figure 3 Top view of flow pattern along a patch of emergent vegetation at the side of a channel with a width b. The flow starts to deflect away and develops towards a fully developed turbulent flow until the adjustment length reaches x_D. After this point stable Kelvin Helmholtz vortices develop and penetrate into the vegetation with a length δ_I and into the bare channel with a length of δ_O. Adapted from Zong and Nepf (2010).

Looking at a submerged vegetation patch, when flow depth exceeds the deflected vegetation height, a vertical mixing layer develops close to the vegetation at a canopy scale (Figure 4). This mixing layer resembles a free shear layer that forms at the edge between two streams of different flow velocities. The velocity profile of this mixing layer can be described by a hyperbolic tangent (Chen et al., 2013). At the top of the vegetation, the inflection point in this velocity profile leads to the emergence of Kelvin-Helmholtz instabilities. These instabilities have the potential to evolve into eddies dominating the vertical transport of momentum into the vegetation (Nepf, 2012a). Raupach et al. (1996) first observed this mixing layer pattern for terrestrial canopies. The penetration depth of these mixing layers governs the turbulence pattern throughout the vegetation and depends on the density, drag coefficients and vegetation geometry ($C_d ah$) (Nepf, 2012b). Nepf and Ghisalberti (2008) show that if the product of these coefficients is between approximately 0.1 and 0.2, the eddies penetrate until the bed. However, the penetration depth of the eddies reduces significantly for larger canopy densities

($C_d ah > 0.2$). Lastly, the individual stems, leaves and branches in a vegetation patch can generate stem-scale turbulence, as the flow is affected by the form drag of the individual canopies in the patch.

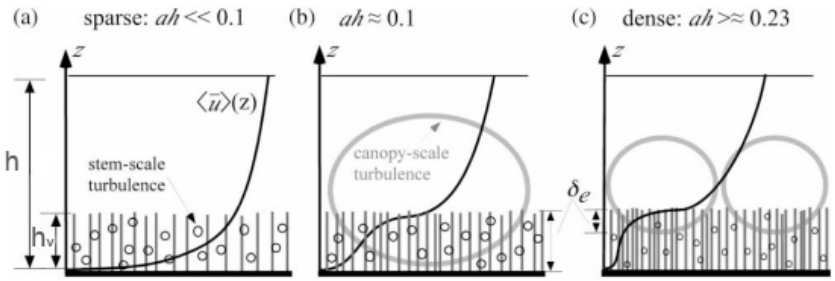

Figure 4. Flow velocity distribution within a submerged vegetation canopy for different vegetation densities. The vegetation patch height is h_v, and the water depth is h. (a) For $C_d ah \ll 0.1$, the velocity profile follows a hyperbolic rough boundary layer profile. (b) For $C_d ah \approx 0.1$ the velocity profile follows a hyperbolic tangent with an inflection point and the development of canopy-scale turbulence. The canopy-scale turbulence penetrates a distance of δ_e into the vegetation. (c) For $C_d ah >\approx 0.23$, the vegetation patch is dense enough such that the bed is protected from the canopy-scale turbulence. Stem-scale turbulence is generated throughout the vegetation patch. Adapted from Nepf (2012a).

The studies mentioned above have only studied the shear layer in either the horizontal (e.g., Rominger and Nepf (2011)) or the vertical plane (e.g., Nepf (2012a)). In these studies, the flow is characterized by two regions of constant velocity, separated by a confined shear layer with the associated Kelvin-Helmholtz vortices in either the horizontal or the vertical plane. The study of Villota et al. (2023) focuses on how the shear layer will behave in both the horizontal and vertical plane for a rigid submerged vegetation patch (Figure 5). In the vertical plane, the study shows that the shear layer follows a hyperbolic tangent profile, analogous to Nepf and Ghisalberti (2008). In the horizontal plane, the inner shear layer thickness is set by the vegetation density corresponding to the observation of Rominger and Nepf (2010). However, the outer shear layer forms a near-sinusoidal velocity distribution that bulges upward or downward with the vertical velocity of the secondary circulation.

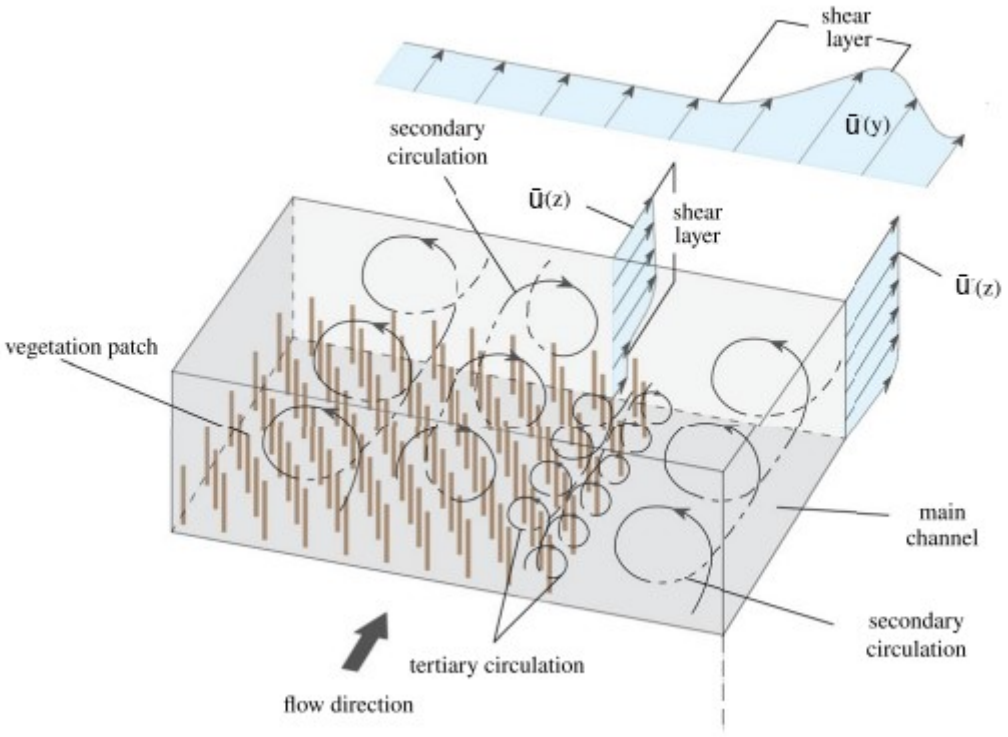

Figure 5 The three-dimensional mean flow and turbulent structure in a vegetated channel with a submerged rigid vegetation patch. Three different shear layers are formed, one in the horizontal direction and a vertical shear layer inside and outside the vegetation. Taken from Villota et al. (2023).

White and Nepf (2007) show in their experimental study with an array of rigid cylinders that this transverse mean streamwise velocity profile is asymmetric in the equilibrium region ($x > x_d$), and thus the shear layer cannot be characterised by a single length scale. White and Nepf (2007, 2008) proposed a two layered vortex-based model in which the asymmetrical mixing layer has been divided into an inner (δ_I) and an outer layer (δ_O), each with its length scale and connected with a matching point (y_m) as can be seen in Figure 6. In the inner zone ($y < y_m$), high Reynolds stresses occur at the interface between the vegetated and the non-vegetated zone and can be described by a hyperbolic tangent. The inflection point coincides with the array edge, except for the most sparse vegetation patch in their study, where the inflection point is just outside the vegetation patch. The penetration depth of the vortices into the vegetation is set by the resistance of the vegetation, which depends on the vegetation density. The wider outer zone ($y > y_m$), adjacent to the interface in the non-vegetation zone, resembles a boundary layer profile which can be described by a second-order polynomial.

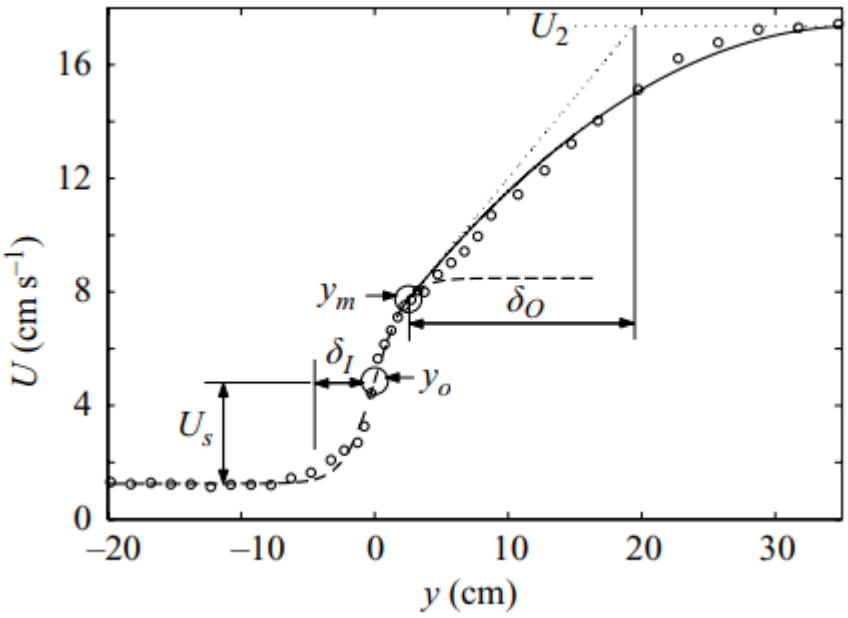

Figure 6 Two layered vortex-based model showing the inner and outer layers of the velocity regions. The dotted line shows the hyperbolic tangent approximation of the inner layer ($y < y_m$), and the solid line shows the quadratic approximation of the outer layer $y > y_m$. The matching point is indicated by the point y_m, at this point the slopes of both approximations match, and the inflection point of the inner layer is indicated by y_o. Taken from White and Nepf (2007).

In flume studies, it is shown that the penetration depth of the vegetation is independent of the characteristics of the main channel. Instead, it is set by the lateral drag and shear stress balance across the vegetation patch. As a result, it exhibits a significant correlation with the canopy drag length scale ($(C_d a)^{-1}$) (Rominger and Nepf, 2011; White and Nepf, 2008). However, if the canopy drag length scale becomes less than the diameter of an individual cylinder, the penetration length scale becomes independent of the canopy drag length scale. By curve fitting of the measurements of White and Nepf (2007, 2008) and Tsujimoto et al. (1991), the following equation to estimate the penetration depth into the vegetation patch (δ_I) has been proposed (White and Nepf, 2008):

$$\delta_I = \max(0.5(C_d a)^{-1}, 1.8d) \tag{2}$$

The outer layer is balanced by the pressure gradient from the free surface slope and the lateral shear stress, and therefore the penetration depth into the channel (δ_O) scales with the water depth (h), the bed friction (c_f), the time-averaged flow velocity in the bare channel (U_2) and the maximum shear velocity (u_*^2) (White and Nepf, 2007):

$$\delta_O \sim \frac{u_*^2}{U_2^2}\frac{2h}{c_f} \tag{3}$$

It should be noted that the empirical two-layer vortex model and the formulae for the different length scales are solely based on studies with arrays of rigid cylinders on a flatbed in the flume. Therefore, results from a wide range of (natural) vegetation patches and different riverbeds are required before these generalisations can be confirmed.

Hopkinson and Wynn (2009) and Liu et al. (2017) are some of the first flume experiments that examined the influence of different types of artificial vegetation on a sloping riverbank, such as grass simulated by a woven grass mat or trees with wooden dowels. Their studies show that with increasing riverbank vegetation density, the streamwise velocity in the open channel increases, and a sharp

velocity gradient between the vegetated and the non-vegetated zone occurs. However, in their studies, only qualitative evidence for the turbulence structure is observed (i.e., progressive waving of vegetation and downstream vibrations of the dowels). The maximum turbulence intensity for the vegetation types occurs in the mixing zone between the vegetated and the non-vegetated zone, suggesting momentum exchange in the lateral direction. However, in their flume studies, the proposed fundamental equations of White and Nepf (2007, 2008) have not been applied. Therefore, the applicability and representativeness of these fundamental equations in the case of a channel with a riverbank slope is still unknown.

In a non-vegetated compound channel with a transverse slope, the transverse depth difference preserves the formation of the shear layer, and the bed friction limits the growth of the shear layer (Fernandes et al., 2014; Truong and Uijttewaal, 2019). The presence of vegetation in a compound channel adds another source of drag and thus significantly increases the velocity difference between the vegetated and the non-vegetated part of the channel, stimulating the formation of Kelvin-Helmholtz vortices (White and Nepf, 2007). The research of Truong and Uijttewaal (2019) looks into the effect of vegetation on a floodplain on the formation of the Kelvin-Helmholtz vortices. A vegetated compound channel is not exactly the same as riverbank vegetation, although it is currently the only existing model to describe the transverse momentum exchange in a vegetated channel. It turns out that the current momentum exchange models based on compound channels without vegetation by van Prooijen et al. (2005) and the partial vegetated channel of White and Nepf (2007, 2008) are not applicable in describing the transverse momentum of a compound vegetated channel. Successfully, a new hybrid model has been proposed by Truong and Uijttewaal (2019) with an additional coefficient to incorporate the effect of the river slope on the penetration depth into the main channel.

The research of Huai et al. (2019) explored the mean flow and the turbulence structure of an open channel covered with an array of dampers at the side, representing flexible vegetation. These dampers consist of plastic floaters attached to the bottom of the flume using a thin rope. Their analysis shows that the mixing layer thickness increases and stabilizes to an equilibrium value, corresponding approximately to the interior adjustment region of a patch with rigid cylinders described in Rominger and Nepf (2011) (Figure 3). Furthermore, in the fully developed flow region after the adjustment length, large coherent vortex structures have been observed due to the inflection point in the transverse mean flow velocity profile. However, the asymmetrical feature of the velocity profile proposed by White and Nepf (2007) is not clearly visible. Following the observations of White and Nepf (2007), the shear-scale vortices appear near the interface between the vegetated and the non-vegetated zone.

All the studies mentioned above have used emergent arrays of cylindrical vegetation or floaters with a uniform diameter. However, natural vegetation flexibility and non-uniformity have an essential influence on the hydrodynamics due to the reconfiguration ability into a more streamlined position (Caroppi et al., 2019; Yagci et al., 2016). This flexibility and heterogeneity of vegetation patches have not been taken into account in the studies above as the patch flow blockage factor ($C_d aD$) is assumed to be constant. The recent research by Caroppi et al. (2022) investigates the effect of these characteristic features of natural riparian vegetation on the mean and turbulent flow structure. The drag of the riparian vegetation patch was increased by 3.0 - 4.4 times by the presence of foliage, and the observed reconfiguration-induced drag for this type of flexible riparian vegetation results in a 60% decrease in the blockage factor with increasing flow velocities (Caroppi et al., 2022). Thus, the blockage factor is essential to describe different types of flexible vegetation. It impacts the distribution of the transverse (turbulent) flow field, which contradicts White and Nepf (2007, 2008), who stated that the vegetation density does not affect the outer layer. Although the riparian vegetation in the study of

Caroppi et al. (2022) is not riverbank vegetation, it shows the importance of considering the flexibility and non-uniformity of vegetation.

Lastly, the research of Liu et al. (2022) develops a model to predict the lateral profile of velocities inside and outside an emergent vegetation patch on one side of the channel. Their model uses only the incoming flow and the vegetation characteristics to describe the lateral profile of the flow velocities at different longitudinal positions across the vegetation patch. This analytical model has been validated using data from their flume experiments with rigid cylindrical emergent vegetation and three other experimental studies with rigid cylinders from literature (Caroppi et al., 2020; White and Nepf, 2007; Zong and Nepf, 2010). However, the validity of this study is limited to a straight channel with a flatbed with a relatively dense vegetation patch consisting of an array of rigid cylinders.

To conclude, it can be seen that the presence of emergent vegetation on a riverbank has a significant role in the mean velocity, turbulence and characteristics of the accompanying mass and momentum flux at the boundary between the vegetated and the non-vegetated zone. However, the fundamental empirical equations that describe the flow development are based on experiments with rigid cylinders. Additionally, recent studies have shown the importance of considering the irregularity, morphology and flexibility of vegetation patches (Caroppi et al., 2021, 2022; Liu et al., 2017).

1.3 Problem Description and Knowledge Gap

Vegetation induces a significant drag force on the surrounding water, altering the natural stream's flow field and turbulence distribution. Over the last decades, new state-of-the-art measurement techniques have allowed researchers to measure water motions through vegetation canopies with high spatial and temporal resolutions under idealised circumstances, resulting in an abundance of data on the hydrodynamic variability of the flow field within and around rigid vegetation (e.g., Liu et al., 2017; Rominger and Nepf, 2011; White and Nepf, 2007).

This abundance of data has given the opportunity to conceptualize and calibrate analytical and empirical formulae to describe the flow through vegetation patches consisting of morphologically simple elements such as rigid cylinders. However, recent studies have shown that some simplifications on the experimental setup (i.e., use of rigid elements, homogeneous density) can bias the research's outcome by hiding or amplifying some relevant processes found under natural conditions (Tinoco et al., 2020). Furthermore, studies that incorporate natural vegetation patches demonstrate that they have a significant impact on the flow field and turbulence distribution due to their distinctive morphological features, such as shape and flexibility, when compared to rigid cylindrical mimics (Caroppi et al., 2021, 2022). However, due to the lack of field measurements without idealised circumstances, the actual flow-vegetation interaction is currently relatively unknown.

To conclude, idealised experiments have derived practical relations and insights into the hydrodynamic processes. However, the representativeness of the results of these idealised experiments is limited in their applicability, as their parametrisations could lead to significant bias in the outcomes when describing the complex hydrodynamic behaviour governed by the complex morphology and flexibility of a natural vegetation patch. Therefore, further research is needed to explore the applicability of these idealised parametrisations in the case of natural vegetation under realistic conditions (i.e., variable cross-section, riverbank slope).

1.4 Research Objective and Questions

Despite the recent advances in laboratory experiments and hydraulic modelling and the abundance of data from flume experiments, the hydrodynamic variability in natural streams with riverbank vegetation is still not well understood. Furthermore, it is unknown whether the idealised derived

formulae could efficiently address various management and modelling challenges, including flow resistance and the associated water level increase caused by the vegetation and the enhancement of current flow-vegetation models. The objective of this study is threefold. The first objective is to investigate the effect of the spatial configuration of different vegetation patches on the flow and wake development. Furthermore, the aim is to see if different types of natural riverbank vegetation affect the distribution of the mean flow velocities and turbulence characteristics across the river cross-section differently compared to flow through vegetation patches consisting of morphologically simple elements such as rigid cylinders. The last objective of this study is to assess the representativeness of the idealised derived formulae for natural vegetation with complex morphology. To achieve this objective, the research questions are formulated as follows:

1. What is the effect of the spatial configuration of flexible vegetation patches at the sides of a flume on the longitudinal and cross-sectional development of the mean flow velocities?
2. How do distinctively different patches of riverbank vegetation in the field affect the distribution of the mean flow velocities and the turbulence characteristics across the river cross-section?
3. How applicable are the existing semi-empirical relations describing the longitudinal and cross-sectional flow velocity distributions from flume experiments to measurements in a natural stream, and how could these relations be adjusted to be more accurate for the field?

1.5 Thesis Outline

This thesis has the following structure. Chapter 2 starts with a theoretical framework describing the relevant empirical relations of this research. Subsequently, the experimental setup of this research can be found in Chapter 3. In Chapter 4, the results of the flume and field studies are given per research sub-question. Afterwards, the discussion will be provided in Chapter 5. Chapter 6 includes the conclusions, where answers to the various research questions are presented. Lastly, recommendations for further research will be provided in Chapter 7.

2 Theoretical Framework

This chapter provides the definition of the parameters and a more in-depth explanation of the analytical models used in this study. First, the theory about vegetation drag of vegetation patches is explained. After this, an overview of the existing analytical models describing the transverse momentum exchange and the lateral distribution of the streamwise flow velocity profile is provided.

2.1 Vegetation Drag and Vegetation Characteristics

Most laboratory experiments studying the flow-vegetation interaction use rigid cylinders to model individual vegetation elements. According to the classical quadratic law formula (Tanino and Nepf, 2008), the drag force (F_d) acting on a cylinder can be described using the following equation:

$$F_d = \frac{1}{2}\rho C_d A_p \overline{u}^2 \tag{4}$$

In which ρ is the water density and $\overline{u}$ the time-averaged flow velocity of the water. The frontal area (A_p) of a cylinder is defined by the height and the diameter. For an isolated rigid cylinder, the standard drag coefficient is approximately 1 ($C_d \approx 1$), for a broad range of stem Reynolds numbers (Equation 5) (Stone and Shen, 2002). This Reynolds number is based on the cylindrical diameter (d) and the kinematic viscosity of water (ν).

$$Re_d = \frac{\overline{u}d}{\nu} \tag{5}$$

For natural vegetation, the drag coefficient depends on the morphology and flexibility of the individual plants. Flexible vegetation is pushed over as the flow velocity increases, decreasing the frontal area and the drag coefficient. The classical quadratic law does not hold anymore, as there is a slower drag force increase than predicted by the quadratic law. To incorporate the flexibility of vegetation, the quadratic relationship between the drag force and the velocity should be adjusted by an exponent (γ) observed for aquatic vegetation that varies between rigid (0) and very flexible (-2) (Equation 6) (Nikora, 2010b; Vogel, 2020).

$$F_x \propto \overline{u}^{2+\gamma} \tag{6}$$

In river streams, emergent vegetation often grows along the riverbank, creating long vegetation patches with a certain width (Nepf, 2012c). The geometry of a patch is described in literature most often by the frontal area per unit of canopy volume (a) (Equation 7) or the frontal area per unit bed area (λ_f) (Equation 8) (Rowiński and Radecki-Pawlik, 2015). The frontal area per canopy volume is the number of stems per square meter (n) multiplied by the stem diameter (d). The frontal area per unit bed area can be calculated by taking the integral of the projected plant area per unit of volume over the water depth (h). Of course, the stem diameter and the frontal area per canopy volume can spatially vary within the patch and over the height of the canopy due to flexibility. Therefore, the vegetation characteristics described below are only valid for flow through rigid cylindrical vegetation elements (Plew, 2010).

$$a = \frac{d}{\Delta S^2} = nd \tag{7}$$

$$\lambda_f = \int_{z=0}^{h} a dz = ah \tag{8}$$

Each cylindrical element is described by a particular characteristic diameter and an averaged spacing between the elements (ΔS). The average spacing between the individual elements can be calculated using geometrical laws using Equation (9).

$$\Delta S = \frac{1}{\sqrt{n}} \tag{9}$$

Another way of parametrising the density of the vegetation patch is using the solid volume fraction. In the case of a vegetation patch consisting of cylindrical vegetation elements, the solid volume fraction can be approximated by Equation (10).

$$\phi = \frac{\pi}{4} ad \tag{10}$$

These parameterisations are insufficient for foliated plants to describe the characteristic area for these vegetation types fully. For example, it is hard to determine the exact value of the frontal area per canopy volume for natural vegetation due to their complex morphology. An approximation of the (depth-averaged) frontal area per canopy volume could be calculated by multiplying the average total one-sided frontal area of the patch multiplied by the number of stems per bed area divided by the average canopy height of the vegetation patch (h_v) (Equation 11) (Liu et al., 2022)

$$a_d = \frac{nA}{h_v} \tag{11}$$

2.2 Analytical Transverse Velocity Profiles Models

This section gives an overview of the existing analytical models describing the riverbank vegetation-flow interactions.

In a vegetated channel with a riverbank slope, the flow can be divided into four different regions, which have different flow characteristics and are governed by different physical parameters and length scales (Truong and Uijttewaal, 2019; White and Nepf, 2008). The first region (I) is the region inside the vegetation patch. In this region, the flow velocities are controlled by the drag and the density of the vegetation patch ($C_d a$) (Nepf, 2012c). The second region (II) and the third region (III) are the inner and outer mixing layers, which are governed by the Kelvin-Helmholtz vortices. The total mixing layer width consists of a mixing region width in the vegetated zone (region II) and the non-vegetated zone (region III) ($\delta = \delta_o + \delta_I$). The fourth region (IV) is the region with uniform mean flow velocities in the open channel.

In a partially vegetated channel and a floodplain vegetated channel, the fully developed stationary flow equation can be derived from the 2-D shallow water equations (White and Nepf, 2007). After taking the time average of the velocity components, the simplified momentum equation can be written as:

$$0 = -\rho g \frac{\mathrm{d}(1-\phi)h_m}{\mathrm{d}x} + \frac{\partial(1-\phi)\tau_{xy}}{\partial y} - D_x \tag{12}$$

In which, D_x is the drag force exerted on the fluid in the x-direction, which consists of the bed friction (c_f) and the vegetation drag (Equation 4) within the vegetation ($y < 0$), and only the bed friction outside of the vegetation ($y > 0$).

$$D_x = \begin{cases} \frac{1}{2}\rho\left(C_D a + \frac{c_f}{h}\right)\overline{u}^2, & y < 0 \\ \frac{1}{2}\rho\left(\frac{c_f}{h}\right)\overline{u}^2, & y > 0 \end{cases} \tag{13}$$

The $\rho g \frac{\mathrm{d}nh_m}{\mathrm{d}x}$ term is the pressure gradient term, in which g is the gravitational constant, h_m the mean surface water slope and ϕ the solid volume fraction of the vegetation. The next term ($\frac{\partial \phi \tau_{xy}}{\partial y}$) accounts for the transverse exchange of streamwise momentum between the vegetated floodplain and the bare channel in which τ_{xy} is the depth- and time-averaged transverse shear stress.

For flow through vegetation patches, the transverse shear stress consists of three components; the dispersive stresses, the Reynolds stress and the shear stress derived from secondary circulation (van Prooijen et al., 2005). As for turbulent flow through compound vegetated channels, the secondary circulations are negligible for most conditions (van Prooijen et al., 2005). In dense vegetation patches, the dispersive stresses are also small (Poggi et al., 2004). Thus, the Reynolds stress is the most significant contributor to the transverse shear stress and Equation (14) holds:

$$\tau_{xy} \approx -\rho \overline{u'v'} \tag{14}$$

Boussinesq proposed a fundamental model in which the turbulent stresses can be related by the eddy viscosity to the mean flow (Schmitt, 2007). Therefore, the depth-averaged turbulent shear stress can be modelled (Equation 15) by finding a proper eddy viscosity (ν_t) parameterization.

$$\tau_{xy} \approx \rho \overline{u'v'} = \nu_t \frac{d\overline{u}}{dy} \tag{15}$$

Two applicable models for partially vegetated channels and vegetated compound channels are the two layered vortex-based model of White and Nepf (2008) and the effective eddy viscosity concept of van Prooijen et al. (2005). Furthermore, another applicable model is the hybrid eddy viscosity model of Truong and Uijttewaal (2019), which extends the effective eddy viscosity concept. All three models will be further discussed in the following sub-sections.

2.2.1 Two Layered Vortex-Based Model

White and Nepf (2007, 2008) proposed a vortex-based model in which the asymmetrical mixing layer has been divided into an inner and an outer layer, each with its own length scale. The matching point is where the inner and outer layer slopes match. As the velocity profile is asymmetric at this point, the inner hyperbolic tangent and the outer second-order polynomial slopes match (Figure 6). The characteristic length scale of the inner layer can be approximated by performing a non-linear regression to a hyperbolic tangent:

$$U_I = U_1 + U_s \left(1 + \tanh\left(\frac{y - y_0}{\delta_I}\right)\right) \tag{16}$$

In which, y_0 is the shear-layer inflection point, U_s is the slip velocity ($U_s = U(y_0) - U_1$). The outer layer resembles a classical boundary-layer profile and can be approximated by the following quadratic boundary profile:

$$U_O = U_m + (U_2 - U_m)\left[\frac{y - y_m}{\delta_O} - \frac{1}{4}\left(\frac{y - y_m}{\delta_O}\right)^2\right] \tag{17}$$

In which U_m is the velocity at the matching point between the inner and outer mixing layers. Furthermore, the model allows calculating the maximum penetration depth through the side edge into the patch of the Kelvin-Helmholtz vortices depending on the vegetation density (Equation 2). The penetration depth into the open channel is related to the bed friction coefficient (C_f) and the water depth $\delta_O \sim \frac{h}{C_f}$. However, until recently, no relationships have been determined. Based on the comparison of different flume studies by Liu et al. (2022), Equation (18) has been proposed to estimate

the penetration depth into the channel based on the fact that the penetration depth into the channel over the vegetation patch width (b) is considered constant in case $\phi \leq 0.045$ (Liu et al., 2022).

$$\frac{\delta_O}{b} = 0.63 \pm 0.14 \tag{18}$$

However, it should be noted that this relationship is based on three different flume studies with rigid cylinders.

The two layered vortex-based eddy viscosity model proposed by White and Nepf (2008) consists of two separate layers. The inner layer eddy viscosity parametrization (ν_I) depends on the maximum shear velocity (u_*^2), the characteristic length of the inner layer (Equation 2) and the slip velocity:

$$\nu_I = \frac{u_*^2 \delta_I}{U_s} \tag{19}$$

The maximum shear velocity was estimated using the maximum shear Reynold stress ($u_*^2 = \max(\overline{u'v'})$) (White and Nepf, 2007). The outer layer eddy viscosity (ν_O) depends on the characteristic length scale of the outer layer (Equation 3) and the maximum shear velocity and the streamwise flow velocity in the bare channel and at the matching point:

$$\nu_O = \frac{0.7 u_*^2 \delta_O}{U_2 - U_m} \tag{20}$$

2.2.2 Effective Eddy Viscosity Model & Hybrid Eddy Viscosity Model

The transverse momentum and velocity profile model proposed by van Prooijen et al. (2005) is one of the most elaborated models for a compound channel without vegetation. In this model, the effect of the bottom friction and the riverbank slope on the mixing layer width is considered.

The eddy viscosity model that takes into account the bottom friction and the riverbank slope is given by:

$$\nu_t = \alpha \sqrt{c_f} U_d D + \frac{h_m}{h(y)} \beta^2 \delta^2 \left| \frac{\mathrm{d}\overline{u}}{\mathrm{dy}} \right| \tag{21}$$

In which α is a calibration constant of approximately which is set a prior to 0.1 for a wide range of compound channels (Fischer et al., 1979). h_m is the mean water depth of the floodplain h_f and the channel h_c. $h(y)$ is the local water depth of the transect. $\beta \approx 0.07$ is the proportionality constant (van Prooijen et al., 2005), depending on the transverse slope (Truong and Uijttewaal, 2019). δ is the total mixing length, consisting of the penetration depth into the channel and the floodplain. $\frac{d\overline{u}}{dy}$ is the slope of the depth and time-averaged velocity profile.

From Equation (21), it can be seen that the eddy viscosity consists of two components related to the bottom friction and the eddy viscosity related to the Kelvin-Helmholtz vortices. The water depth leads to compression of the lateral momentum flux. By continuity, the compression of the lateral momentum flux leads to an increase in the transverse velocity component of the Kelvin-Helmholtz vortices at the floodplain and a decrease in the transverse velocity component of the Kelvin-Helmholtz vortices in the main channel (van Prooijen et al., 2005). This is represented by the $\frac{h_m}{h(y)}\beta^2$ term in Equation (21).

The role of the slope between the main channel and the floodplain is more important than thought for an increased shear rate (van Prooijen et al., 2005). Therefore, Truong and Uijttewaal (2019) proposed

adding an additional term ($h_r = h_f/h_c$) related to the slope of the compound channel in their new hybrid eddy viscosity model. Furthermore, an additional eddy viscosity based on the production of turbulent kinetic energy by the flow through the vegetation is introduced (Equation 22) (Kean and Smith, 2004).

$$v_{\mathrm{tv}} = \frac{1}{8} C_t^{-2} C_d d\overline{u} \tag{22}$$

In which C_t is a constant of proportionality that depends on the shape of the streamwise velocity profile and is usually $C_t = 1$ (Truong and Uijttewaal, 2019).

To summarize, the hybrid model proposed by Truong and Uijttewaal (2019) consists of an additional term related to the slope of the compound channel and an additional term related to the production of turbulent kinetic energy by the flow through the vegetation. Resulting in the following hybrid eddy viscosity model (Equation 23)

$$v_t = \begin{cases} \alpha\sqrt{c_f}\overline{u}D + \dfrac{h_m}{h(y)} h_r^2 \beta^2 \delta^2 \left|\dfrac{\mathrm{d}\overline{u}}{\mathrm{d}y}\right| \text{ (outside vegetation)} \\ \underbrace{\alpha\sqrt{c_f}U\overline{u}}_{\text{Bottom turbulence}} + \underbrace{\frac{1}{8} C_t^{-2} C_d d\overline{u}}_{\text{Vegetation drag}} + \underbrace{\dfrac{h_m}{h(y)} h_r^2 \beta^2 \delta^2 \left|\dfrac{\mathrm{d}\overline{u}}{\mathrm{d}y}\right|}_{\text{KH-vortices}} \text{ (inside vegetation)} \end{cases} \tag{23}$$

2.2.3 Analytical Model of Longitudinal and Transverse Velocity Profiles

In this section, the exponential-based model of Liu et al. (2022) for predicting the velocity fields in partially vegetated channels will be explained. The deflection of the flow starts upfront of the vegetation patch and extends a certain distance into the vegetation. The length of this adjustment distance is related to the patch density and the width and can be estimated by the following equation proposed by Rominger and Nepf (2011).

$$x_d = (5.5 \pm 0.4)\left[\left(\frac{2}{C_d a}\right)^2 + b^2\right]^{\frac{1}{2}} \tag{24}$$

In the vegetated region, which is not influenced by the Kelvin-Helmholtz vortices, the steady longitudinal velocity can be predicted with the model of Liu et al. (2020), shown below:

$$U_1 = U_{1\,(f)} + \left(U_{1\,(0)} - U_{1\,(f)}\right) \cdot \exp\left(-\frac{3x}{x_d}\right) \tag{25}$$

Where $U_{1(f)}$ is the steady velocity in the fully developed flow region ($x > x_d$), $U_{1(0)}$ is the velocity at the leading edge of the patch. Within the patch, Liu and Shan (2019) proposed the following steady velocity in the fully developed flow region, in which S is the water surface slope.

$$U_{1(f)} = \left[\frac{ghS}{C_f + \dfrac{C_d a h}{2(1-\phi)}}\right]^{\frac{1}{2}} \tag{26}$$

According to Liu and Shan (2019), the velocity at the leading edge of a patch ($U_{1(0)}$) normalised by the mean upstream streamwise channel flow velocity (U_0) can be predicted by:

$$\frac{U_{1(0)}}{U_0} = 1 - (0.15 \pm 0.02)(C_d a b)^{\frac{1}{2}} \tag{27}$$

Secondly, at each lateral position, the depth-averaged velocity profile across the vegetated region and the bare channel U can be predicted using Equation (28) and Equation (29). The first equation is valid within the vegetation patch. The second equation is valid in the bare channel. The total width of the channel is B.

$$U = U_1 + \left(U_{y=b} - U_1\right) \cdot \exp\left[\frac{y-b}{L_{d(veg)}}\right] \text{ for } (0 \le y \le b) \tag{28}$$

$$U = U_2 + \left(U_{y=b} - U_2\right) \cdot \exp\left[\frac{b-y}{L_{d(\,bare\,)}}\right] \text{ for } (b \le y \le B) \tag{29}$$

Where $U_{y=b}$ is the velocity at the patch edge ($y = b$) and $L_{d(bare)}$ and $L_{d(veg)}$ are the mean e-folding length scales for vegetation and the bare channel region. These parameters are associated with the velocity change in the vegetated and the bare channel region. The mean e-folding lengths are defined as the mean of the local e-folding scale as calculated by Equation (30) and Equation (31):

$$L_{d(veg)}(y) = (y-b)\left(\ln\frac{U_{(y)} - U_1}{U_{y=b} - U_1}\right)^{-1} \tag{30}$$

$$L_{d(\,\mathrm{bare}\,)}(y) = (b-y)\left(\ln\frac{U_{(\mathrm{y})} - U_2}{U_{y=b} - U_2}\right)^{-1} \tag{31}$$

The velocity at the edge of the vegetation patch and the velocity in the bare channel are the only two unknown parameters when calculating the depth-averaged velocity profile fields (Equations 28 and 29). Two boundary conditions are applied to solve this system of equations without actual measurements for the flow velocity at the edge of the vegetation patch and the velocity in the bare channel. The first boundary condition is that the flow velocities predicted by Equations (28) and Equation (29) should have continuity at the side edge of the vegetation patch ($y = b$) (Equation 32). The second boundary condition is that flow volume coming (BU_0) in from upstream must meet the flow continuity in the vegetated and non-vegetated parts of the channel (Equation 33).

$$\frac{\partial U_{(Eq\ 28)}}{\partial y} = \frac{\partial U_{(Eq\ 29)}}{\partial y} \text{ at } y = b \tag{32}$$

$$\int_0^b U_{(Eq\ 28)}dy + \int_b^B U_{d(Eq\ 29)}dy = BU_0 \tag{33}$$

To conclude, the incoming flow velocity and the width of the channel must be determined to predict the lateral profiles of the flow velocities at different longitudinal positions across the partially vegetated channel. Furthermore, the flow velocity inside the vegetation patch must be calculated using Equations (25) and Equation (26).

Based on the results of the flume data from Caroppi et al. (2020), Huai et al. (2015) and White and Nepf (2007) Liu et al. (2022) proposed that the e-folding length scales are constant with the mixing widths.

$$\frac{L_{d(bare)}}{\delta_O} = 0.64 \pm 0.14 \tag{34}$$

$$\frac{L_{d(veg)}}{\delta_I} = 0.32 \pm 0.04 \tag{35}$$

3 Materials and Methods

This section describes all the methods used to answer the different research questions. In order to analyse the data of both the flume and the field study, the characteristics of the two different study sites will be presented in the following subsection. After which, the experimental measurement plan is presented. In the end, the data pre-processing and the analysis of the hydrodynamic measurements are explained.

In this research, two different types of experiments were used to give answers to the different research questions. The first experiment was a re-analysis of existing flume data from measurements conducted by Cornacchia et al. (2019) at NOIZ, which was used to gain insight into the flow development using natural vegetation patches and used to answer the first research question: *'What is the effect of the spatial configuration of flexible vegetation patches in a flume on the longitudinal and cross-sectional development of the mean flow velocities?'*. Additionally, field measurements were carried out at the vegetated river banks of the River Dinkel. This river originates in North Rhine-Westphalia around Coesfield (Germany), flows through the Netherlands and ends up in the River Vechte near Neuenhaus (Germany). The goal of this field study is to answer the second and the third research question *'How do distinctively different patches of riverbank vegetation in the field affect the distribution of the mean flow velocities and the turbulence characteristics across the river cross-section?'* and *'How applicable are the existing semi-empirical relations describing the longitudinal and cross-sectional flow velocity distributions from flume experiments to measurements in a natural stream, and how could these relations be adjusted to be more accurate for the field?'*

3.1 Flume Study

The first part of this study involved the analysis of the flow-vegetation interaction measurements conducted by Cornacchia et al. (2019). While some of the data had already been presented in their study, our study will use additional flow measurements not used in their paper. The flume experiments were carried out in the unidirectional racetrack flume in the laboratory in NIOZ Yerseke (The Netherlands) in 2015. The total length of the measurable part of the flume was 6 meters and had a width of 0.6 meters. For a more detailed description of the flume set-up, see Bouma et al. (2005).

The effect of macrophytes on the hydrodynamics was tested using two submerged macrophytes species, *Callitriche platycarpa* and *Groenlandia densa* (Figure 7). *Callitriche platycarpa* formed a very dense patch under field conditions that exhibited increasing canopy height with increasing patch length and is referred to as the 'dense' vegetation patch. *Groenlandia densa* had a more open structure with a constant height and is referred to as the 'sparse' vegetation patch. These macrophytes were collected in a field campaign in February 2015 from a wetland on the Ain River in France. During the experiments, the average water depth was 0.35 meters, with a cross-sectionally averaged velocity of 0.24 ± 0.03 m/s at the upstream end of the measurable part of the flume. These flow conditions corresponded to a representative summer flow in natural streams that were typically colonized by *Callitriche* and *Groenlandia* (Cornacchia et al., 2023).

The mean and standard deviation (SD) of the geometric characteristics of both macrophytes can be found in Table 1. The biomass of the patches was measured by collecting all plant material within three random quadrants (0.1 m x 0.1 m). Furthermore, individual plants were sampled and dried in the oven for 48 hours at 60 °C. The bending height of the canopy was measured during the different runs in which the specific patch is situated upfront and thus not affected by the spatial configuration. The average biomass of an individual plant was used to calculate the number of shoots per m^2. The number of shoots per m^2 was calculated by dividing the total patch biomass by the biomass of an individual plant. The shoots per m^2 for the *Groenlandia* patch represented a low density in natural *Groenlandia*

patches, and the *Callitriche* patch represented an average natural patch density (Cornacchia et al., 2023). The frontal area of the plant surface was determined by photographing the individual vegetation canopies and analysing these images using the measuring area function in ImageJ (Schneider et al., 2012). The flexibility and the morphology of the natural plants made it hard to determine the patch parameters, such as the shoots per m^2, the average spacing and the porosity. The frontal area per canopy volume was calculated using the diameter of an individual plant, assuming the vegetation can be approximated as a rigid cylinder (Equation 7).

The height of the two vegetation patches can be found in Figure 7. The relative depth of submergence (h/h_v), i.e., the ratio of water depth to maximum canopy height was relatively constant along the *Groenlandia* patch due to its uniform height. Values of the relative depth of submergence ranged between 3.5 and 7.0 for the *Groenlandia* patch, which corresponded to a shallow submerged vegetation patch ($h_v/h < 5$) (Nepf, 2012c). For the *Callitriche* patch, the relative height of submergence varied from 17.5 at the leading edge of the patch to 2.0 in the middle of the patch, which corresponded to a deeply submerged vegetation patch at the leading edge and shallow submerged vegetation patch at the trailing edge of the vegetation patch (Nepf, 2012c).

Table 1 Summary of the patch characteristics (Mean ± SD) of the two macrophytes at a flow of 0.24 ± 0.03 m/s: Biomass, averaged canopy height and the frontal area of plant surface were measured. The frontal area per canopy volume and porosity were calculated respectively with Equation (7) and Equation (10).

	Biomass (g [DW] m^{-2})	**Bending Canopy Height (m)**	**Shoots per m^2**	**Stem diameter (m)**	**Frontal Area of Plant surface (m^2)**	**Frontal area per canopy volume (m^{-1})**	**Porosity (-)**
Callitriche platycarpa	318 ± 67	0.109 ± 0.027	11003	0.0007	0.006	7.70	0.0042
Groenlandia densa	97 ± 28	0.077 ± 0.014	577	0.0017	0.017	1.03	0.0015

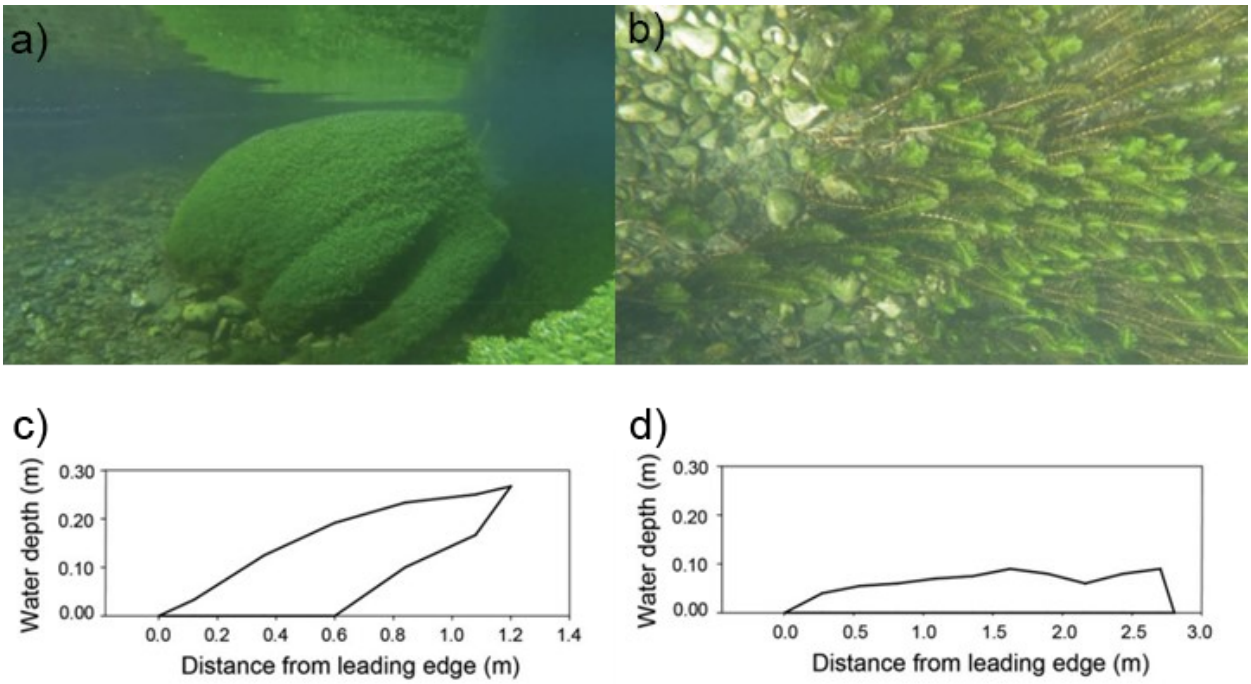

Figure 7 a) The dense vegetation patch, Callitriche platycarpa. b) Sparse vegetation patch, Groenlandia densa. c) Lateral view of the callitriche platycarpa patch. The black outline indicates the patch height. d) Lateral view of the Groenlandia densa patch. The black outline indicates the patch height. All four figures were taken from Cornacchia et al. (2019).

To test for the effects of patch spatial configurations on the hydrodynamics in and around vegetation patches, the two patches were arranged one downstream of the other, either on the same side of the flume (aligned) or on the opposite side (staggered). Furthermore, the two macrophytes upstream were switched resulting in a 'Sparse-Dense' and a 'Dense-Sparse' configuration and the length between the two different patches was varied. In Figure 8, all these different spatial configurations are shown. All spatial configurations could be observed in natural streams within a relatively short distance of 0.5 meters after each other (Cornacchia et al., 2018).

The macrophytes were transplanted into stainless steel trays (30 x 29.5 x 5 cm). The trays were filled with a bottom layer (4.5 cm height) of river sand and a top layer (0.5 cm height) of fine gravel with a mean grain size of 0.2 cm. A total of nine trays were used for the *Groenlandia*, for a total patch coverage of 2.7 x 0.3 m. For *Callitriche*, plants were rooted into two trays of 0.6 x 0.3 m. At the downstream edge of the *Callitriche* patch, two extra trays were added to account for the presence of the typical overhanging canopy due to shoot bending. Furthermore, between the two vegetation patches, trays filled with only the soil substrate were used as spacing between the vegetation patches.

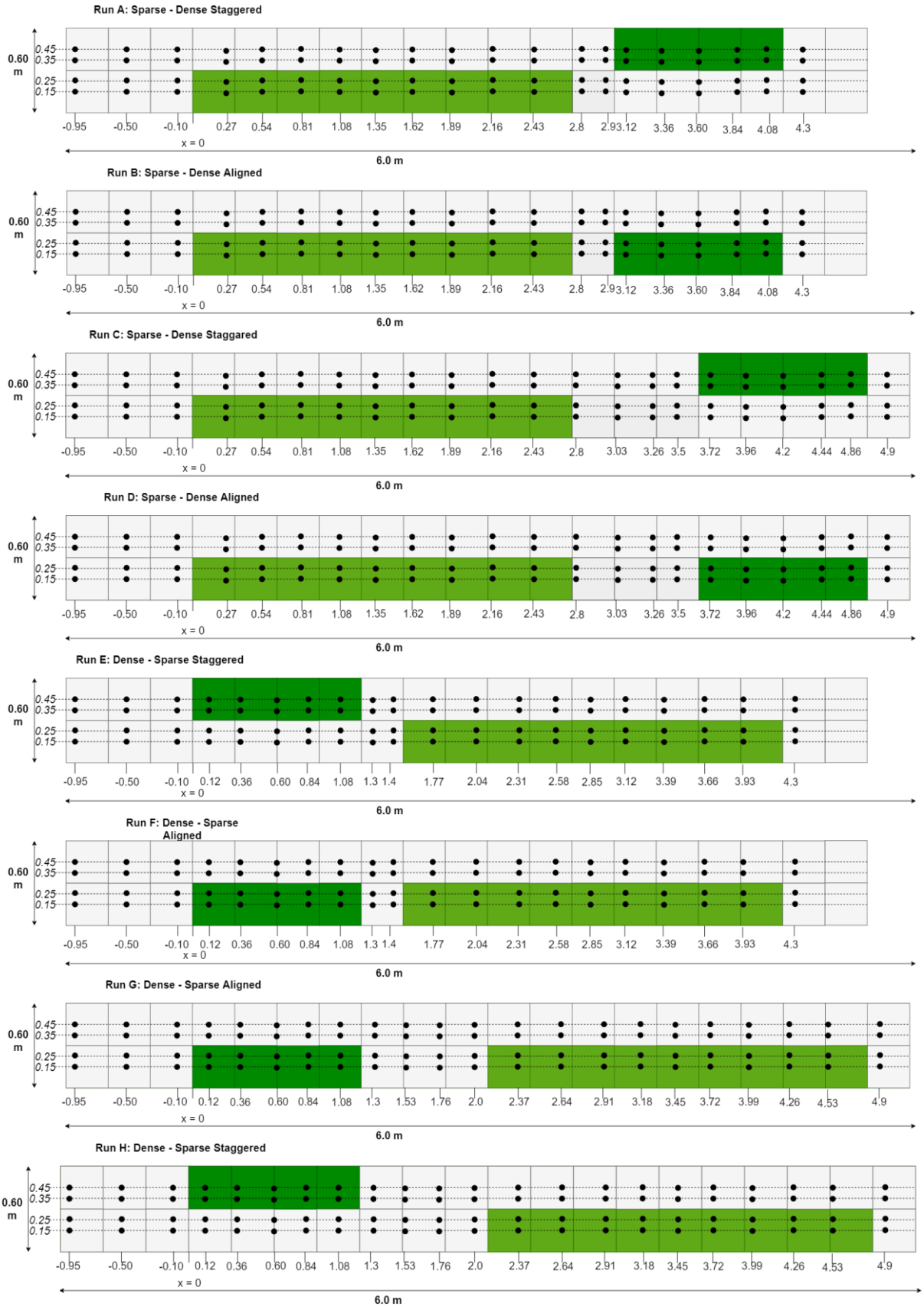

Figure 8 Schematic top-view of all the spatial configurations of the Sparse and Dense vegetation patches with the measurement points (black dots). The green boxes indicate the vegetation patches. Light green is the sparse vegetation (Groenlandia), and dark green is the dense vegetation (Callitriche).

The flow field around the vegetation patches was measured using a Nortek Vectrino acoustic Doppler velocimeter (ADV). The point flow velocities are measured at 10 Hz, and the recording time was 30 seconds, resulting in a total of 300 sample points per measurement point. In the different spatial configurations (Figure 8), the different measurement points are indicated with dots. At each measurement point, point velocities were taken at 2, 5, 10, 12, 15, 17 and 27 centimetres above the flume bed.

The local coordinate system was defined with the origin at the upstream edge of the upstream vegetation patch with the longitudinal coordinate (x) positive in the downstream direction (which is constant for each day in our case). The lateral coordinate (y) was positive towards the middle of the channel with $y = 0$ at the left edge of the flume. Lastly, the vertical coordinate (z) was positive upwards with $z = 0$ at the water surface. The corresponding velocities were then denoted as u, v and w, respectively.

3.2 Field Study

The field experiments were carried out in the River Dinkel at the village Glane in April 2023. The Dinkel is a small meandering river. As can be seen in Figure 9, the measurement location was just downstream of a meander in the river. Upstream of the measurement location, the right channel at the junction is almost completely closed off, so the downstream flow velocities from the side channel were negligible.

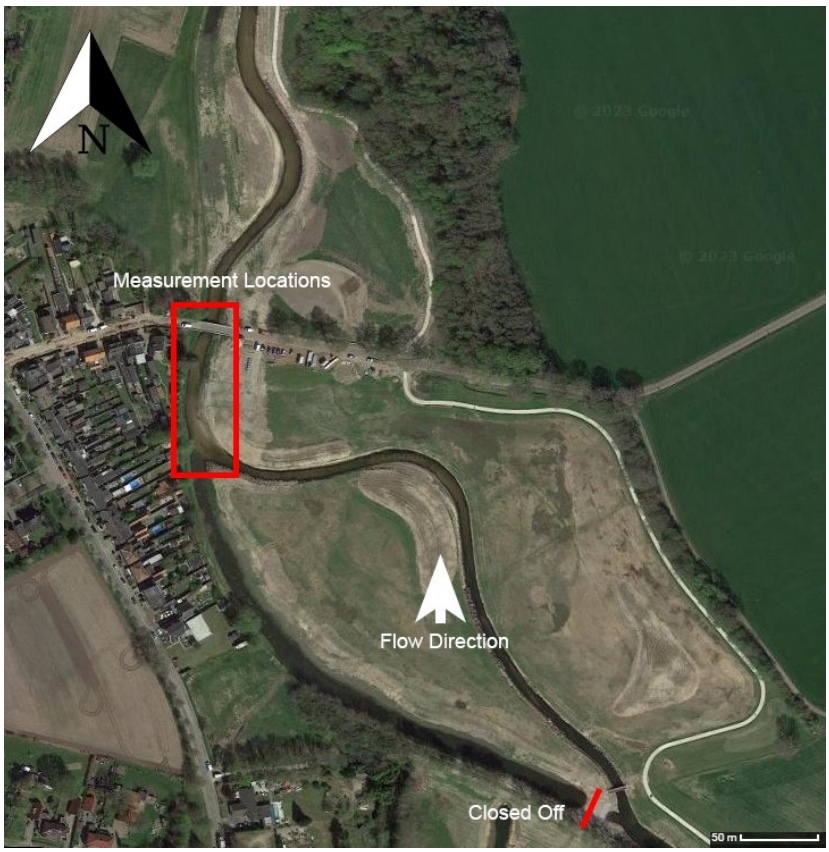

Figure 9 Aerial picture of the river section up and downstream of the measurement locations (red square). The flow direction is towards the north. The thick red line indicates the almost completely closed-off river branch. Source Google Maps

At this location, three different river transects, relatively close to each other, with vegetated riverbanks, were measured on three different days with different water levels (Figure 10). The width of the river was approximately 10 meters with a bank slope of, respectively, 1:2 for locations 1 and 2 and 1:3 for location 3. The vegetation patches were also situated on a higher platform relative to the

channel bed, representing a small floodplain. The riverbed consisted of sandy material with bed forms with a height of approximately 5-10 cm.

Figure 10 Three different measurement locations. Note picture is taken during low water levels. The bed forms of approximately 5-10 cm in height are shown in the top right of the figure. The flow direction is from top to bottom of this picture.

During the field experiments, the depth-averaged flow at mid-depth in the bare channel varied between 0.4 m/s and 0.8 m/s. Upon examining the variation of water levels in the Dinkel (Figure 11), it can be concluded that the measured flow velocities indicated moderate to high water level conditions (Landsemant für Natur Umwel und Verbraucherschutz Nordrhein-Westfalen, 2023).

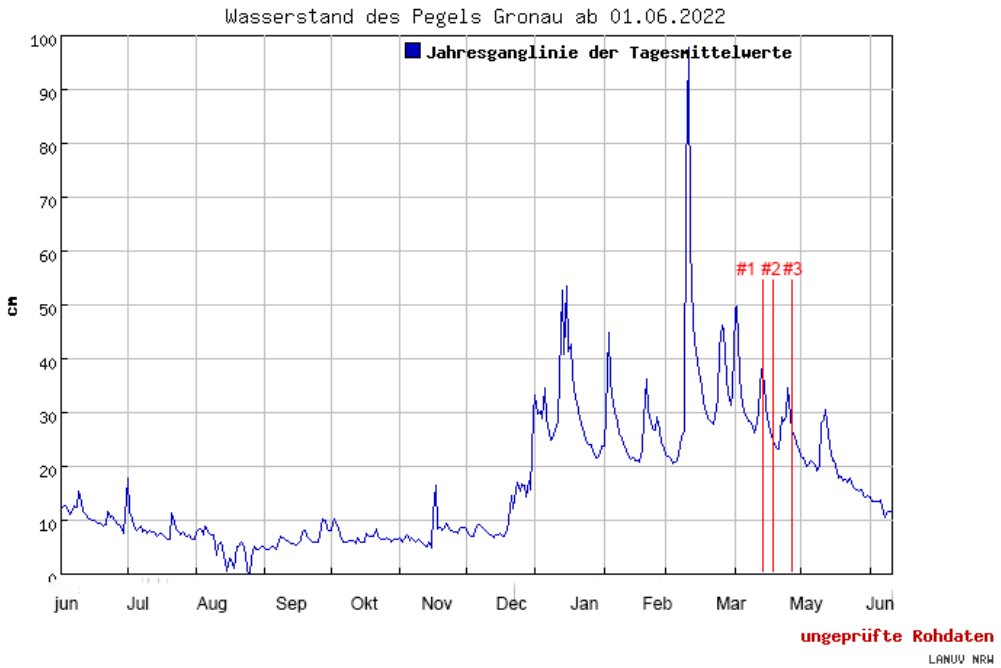

Figure 11 Variations of water levels of the River Dinkel. The red lines indicate the three measurement days (14-04, 17-04 and 19-04). Adapted from (Landsemant für Natur Umwel und Verbraucherschutz Nordrhein-Westfalen, 2023)

At the three different measurement locations (Figure 10), patches of two different macrophyte species were found; two times the *Carex sylvatica* (Location 1 and 3) and one time the *Sparganium emersum*

(Location 2) (Figure 12). Both macrophytes were typical colonizers in this river catchment (Feenstra and Vertegaal, 1976).

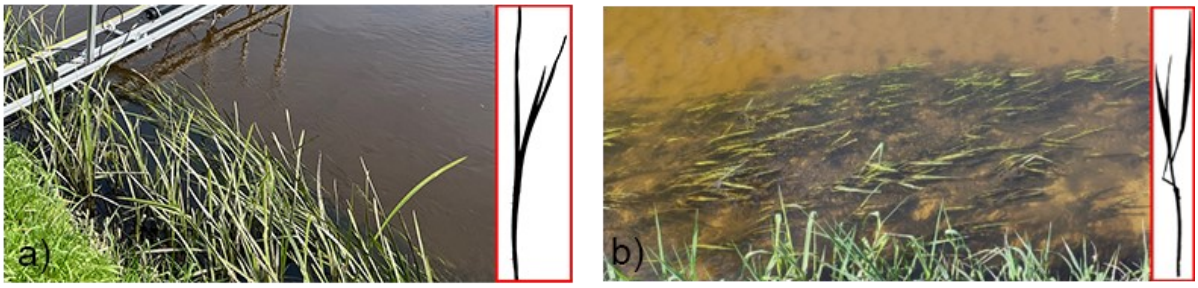

Figure 12 a) Carex sylvatica patch at locations 1 and 3. On the right, the vertical profile of the Carex sylvatica is given. b) Sparganium emersum vegetation patch location 2. On the right, the vertical profile of the Sparganium emersum is given.

The geometric characteristics of the different vegetation patches can be found in Table 2. The biomass of the patches was measured by collecting all plant material within three random quadrants (0.2 m x 0.2 m). Furthermore, 5-10 individual plants were sampled and dried in the oven for 48 hours at 60 °C. To get an approximate of shoots per m^2, the average dry biomass of the individual plants was divided by the total patch biomass, which was determined using the three random quadrants. The average vegetation height corresponded to the average of the deflected height over the cross-section of the vegetation patch. This deflected vegetation height is directly measured in the field. The total one-sided frontal area was measured by photographing the individual sampled plants against a white background with a reference height. The total one-sided frontal area was estimated by converting the image to a black-white binary file based on the colour thresholds. The number of black pixels is counted and scaled according to the reference height. The total one-sided frontal area of natural plants was not uniform and much different than rigid cylinders because of their irregularities and the relatively large leaf areas compared to their stem diameter. The depth-averaged frontal area per canopy volume was calculated using Equation (11). The frontal area per canopy volume was at the lower edge of the values for common aquatic plants (1 – 13 m^{-1}), and the stem diameter was also at the lower edge of the values for common aquatic plants (0.2 – 1.2 cm) (Lightbody and Nepf, 2006; Widdows et al., 2008).

Table 2 Summary of the different patch characteristics (Mean ± SD) at the different measurement locations in the River Dinkel. Patch width, distance from the leading edge of the patch, biomass and the frontal area of the plant surface are measured. The frontal area per canopy volume and porosity are calculated respectively with Equation (11) and Equation (10).

Species (Location)	***Carex sylvatica* (Location 1)**	***Sparganium emersum* (Location 2)**	***Carex sylvatica* (Location 3)**
Patch Width (m)	1.20	1.69	1.50
Distance from the leading edge of the patch (m)	9.0	10.0	7.0
Dry Biomass (g m^{-2})	21.72 ± 5,47	125.56 ± 44.86	20.36 ± 3.17
Shoots per m^2 (n m^{-2})	37.45 ± 9,42	35,13 ± 12.55	32.94 ± 5.13
Average Spacing between canopies (m)	0.16 ± 0.02	0.17 ± 0.03	0.17 ± 0.01
Stem diameter (cm)	0.16 ± 0.09	1.16 ± 0.16	0.43 ± 0.11
Average Patch Height (m)	0.32 ± 0,07	0.58 ± 0.14	0.28 ± 0.18
Total One-sided Plant surface (cm^2)	143.16 ± 35.04	485.75 ± 133.98	110.63 ± 56.79

Frontal Area per Canopy Volume (m^{-1})	1.69 ± 0.72	2.94 ± 1.51	1.30 ± 1.07
Porosity / Solid Volume Fraction (-)	0.002 ± 0.002	0.027 ± 0.014	0.004 ± 0.004

In the case of (emergent) vegetation patches, the flow deflects laterally from the vegetated zone into the bare channel (Figure 3) (Zong and Nepf, 2010). The interior adjustment length of deflection was calculated using Equation (24). As can be seen in Table 3, the field measurements were conducted at the upper edge of the derived interior adjustment length for locations 1 and 2. Thus the flow was fully developed, and the Kelvin-Helmholtz vortices could have been formed at the lateral edge of the vegetation patch. The measurements at the third location were taken within the adjustment region. Thus, it could be that the flow is not fully developed in the location, and the Kelvin-Helmholtz vortices will not be fully developed at the lateral edge of the vegetation patch. However, it should be noted that calculating the interior adjustment region is based on a highly empirical equation, as it is based on one set of measurements with uniform rigid artificial vegetation patches, and the validity is only limited to patch widths between the 4 and 40 centimetres.

Table 3 Overview of interior adjustment length and the distance from the leading edge of the three vegetation patches. The distance from the leading edge of the vegetation patch was measured in the field. The interior adjustment length was calculated using Equation (24).

Species (Location)	***Carex sylvatica* (Location 1)**	***Sparganium emersum* (Location 2)**	***Carex sylvatica* (Location 3)**
Distance from the leading edge of the patch (m)	9.0	10.0	7.0
Interior Adjustment Length (m)	8.90 ± 0.39	10.34 ± 0.16	10.71 ± 0.18

Based on the different water depth measurements and the vegetation height over the cross-section of the vegetation patch, the relative cross-sectional depth of submergence was calculated. At the first measurement location, the relative depth of submergence in the transverse direction was relatively constant, ranging from 1.2 at the riverbank to 1.3 at the edge of the vegetation patch, corresponding to a shallow submerged vegetation patch (Nepf, 2012c). For the second location, the relative depth of submergence ranges from 1.1 at the riverbank, 0.5 in the middle of the vegetation patch and 1.3 at the edge of the vegetation patch, indicating that it was a mix of shallow submerged as well as emergent vegetation (Nepf, 2012c). In the third measurement location, the relative depth of submergence is around 1.1 for the whole vegetation patch indicating that the patch is shallow submerged and close to emergent (Nepf, 2012c).

The flow within and around the vegetation patches was measured at three measurement locations to test the effects on the distribution of the mean flow velocities and the turbulence characteristics across the river cross-section for different vegetation types. For each measurement location, the cross-sectional (transverse) velocity field inside and outside of the vegetation patch is measured simultaneously using two Nortek Vector ADVs. The point flow velocities are measured at 64 Hz, and the recording time was 3 minutes, resulting in a total of 11520 sampling points per measurement point. The ADVs are mounted to a movable rigid frame (Figure 13), where the height and the horizontal alignment of two ADVs can be adjusted independently.

Figure 13 Overview of the experimental setup with the movable frame with two ADVs mounted. The length of the frame is 6 meters.

The point flow velocities for each case were measured at a single transect several meters downstream of the leading edge of the vegetation patch. The exact distance from the leading edge depends on the measurement day and the accessibility of the measurement location. In Figure 14, an overview of the measurement points for each vegetated river cross-section is provided. As can be seen, the horizontal direction consists between the 13 and the 54 measurement points, depending on the width and the density of the vegetation patch. The point measurements were taken at two different depths relative to the water depth, at approximately 40% and 90% of the water depth. However, for the first measurement location also points close to the bed at approximately 10% of the water depth were measured. The flow velocities measured at $0.4h$ above the bed were used as a proxy for the depth-averaged velocities, as it is shown for hydraulic rough flows with different roughness that the depth-averaged flow velocities are obtained at approximately 40% of the water depth above the bed (Van Rijn, 1990). Only for measurements inside the vegetation at location 3, a linear interpolation was performed between the measurement close to the surface and the measurement close to the bed to get a representative value for the depth-averaged flow velocity at that lateral distance.

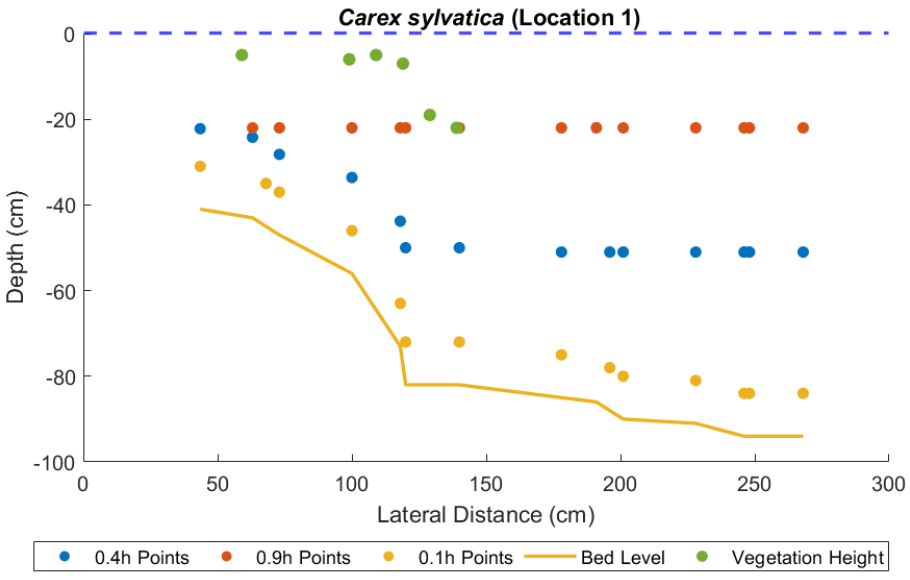

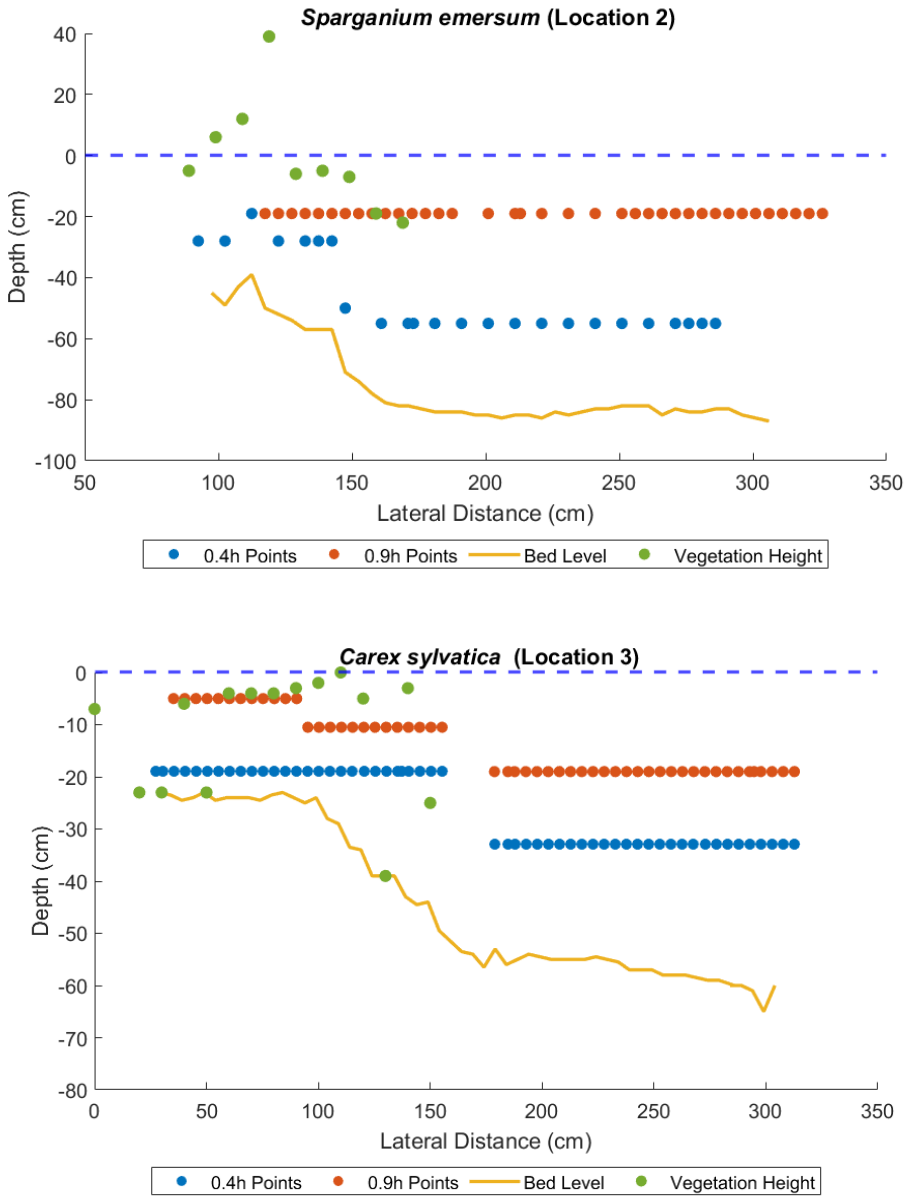

Figure 14 Overview of the measurement points at the three different measurement locations. The red, blue, and yellow dots represent the point velocity measurements at approximately 0.9h, 0.4h and 0.1h from the bed. The green dots indicate the deflected vegetation height measurements. The solid yellow line is the bed level.

For each cross-sectional vegetation patch, the local coordinate system was defined with the origin at the riverbank with the longitudinal coordinate (x) positive in the downstream direction (which is constant for each day in our case), the lateral coordinate (y) positive towards the middle of the channel and the vertical coordinate (z) positive upwards with $z = 0$ at the water surface. The corresponding velocities are then denoted as u, v and w, respectively.

3.3 Flow Analysis and Data Processing

This section describes how the data (pre-)processing and the flow measurement data analysis are performed for the field and the flume study.

3.3.1 Flow Analysis

In order to describe the spatially heterogeneous flow around the vegetation patches, the Reynolds decomposition in time was used (Figure 15). At each measurement location, the ADV gives three

instantaneous velocities $u(t), v(t), w(t)$, in the streamwise, lateral and vertical direction. These velocities were decomposed into time-averages $\overline{u}$, $\overline{v}$, $\overline{w}$ and instantaneous turbulent fluctuations $u'(t), v'(t), w'(t)$, such that $u'(t) = u(t) - \overline{u}$ and similarly for v and w. The vertical average of the time-averaged velocity in the streamwise direction was used to calculate the depth-averaged velocity U at each profile position. However, this depended on the number of measurement points along the vertical.

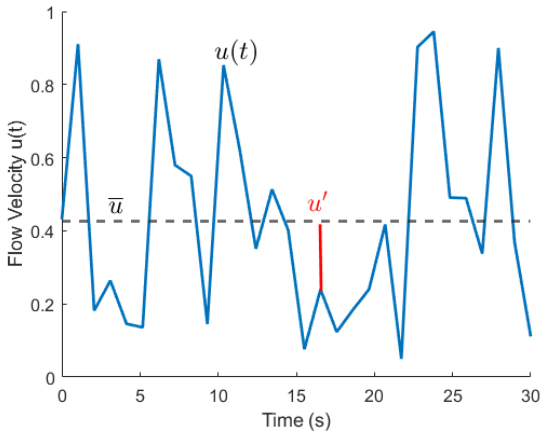

Figure 15 Reynolds decomposition for velocity component u(t)

The turbulent kinetic energy per unit mass (k) is given in Equation 36 (Kundu et al., 2015).

$$k = \frac{1}{2}\left(\overline{u'^2} + \overline{v'^2} + \overline{w'^2}\right) \tag{36}$$

3.3.2 Data Pre-processing

Even though acoustic Doppler velocimeters are widely used in laboratory and field studies to get insight into three-directional flow velocities, these measurements can occasionally record erroneous data, which may show up as spikes in time series. For example, due to plants that could interfere with the acoustic signal or when measuring close to the bed. Another errors that could occur are the so-called weak spots and show noisy velocity traces in the ADV data (Nortek, 2022). This happens when the first pulse gets reflected by the bottom and reaches the sampling volume simultaneously with the second pulse going through the sampling volume, and both pulses cancel each other out.

The raw ADV data of both the Vectrino from the flume study and the Vector from the field study were prefiltered by discarding values with a signal-to-noise ratio and correlation lower than 15 dB and 70%, respectively, as suggested by the ADV manufacturer (Nortek, 2022).

Different post-processing techniques have been developed to remove erroneous data from the recorded data series, such as the Phase-Space Threshold Method (PST) (Goring and Nikora, 2002) and the Modified Phase-Space Threshold Method (M-PST) (Parsheh et al., 2010). In this research, the M-PST method was used to remove spikes from the recorded data as the PST method tends to incorrectly identify valid measurements adjacent to the spikes, as spikes have greater magnitude compared to the valid data (Jesson et al., 2013). The M-PST method tries to overcome this problem by setting an upper limit for valid values, which is used to identify large-magnitude spikes before applying the PST method.

Once a spike has been detected and removed from the time series, the gap should be replaced by an approximated value. Goring and Nikora (2002) have proposed several replacement methods, such as the last good value (LGV), linear interpolation (LI) and the 12-point polynomial (12PP). The LGV method replaces any spike with the last good value. The LI method calculates the replacement value by simple

linear interpolation between the valid values surrounding the spike. A downside of this method is that in the iterative despiking method, if the surrounding value is a spike that will be removed in the following iterations, the replacement value may constitute a spike. Lastly, the 12PP method is the best-fit cubic polynomial for the 12 valid points on either side of the spike (so 24 points in total), which are used to calculate the replacement value. According to Goring and Nikora (2002), the benefit of this model is that it overcomes the downside of the LI method, that the surrounding values could also be a spike. The spike duration is typically relatively short and, therefore, would have little effect on the 12PP method.

In order to choose the most suitable combination of despiking and replacement method, the results of a comparison study between the different methods by Jesson et al. (2015) was used. It turned out that the M-PST is recommended because of its computation efficiency and accuracy in detecting the spikes. The recommended replacement method is depending on the detection method as the combination could lead to a not accurate reconstruction of the spectral density distribution. The suggested replacement method for the M-PST method is the last good value method. Therefore, in combination with the M-PST method the LGV replacement method was used. The Velocity Signal Analyser software (v.1.5.67) was used to perform the despiking and replacement of the raw data.

Lastly, after the despiking methods had been performed, a manual visual inspection of the different time series was performed. The whole time series of a point measurement was discarded, whether there is a negative velocity or a strange turbulence recurring pattern, e.g., due to plant obstruction, or when the replacement methods have replaced the ~60% of the time series.

4 Results

4.1 Flow and Wake Developments Flume Study

In this section, the analysis of the hydrodynamic measurement of the eight different spatial configurations of natural vegetation patches in the flume experiment will be discussed. This chapter has been split into aligned configurations, which represent riverbank vegetation, and staggered patch configurations, representing the interaction of riverbank vegetation with instream vegetation. The flow velocities are measured along four longitudinal transects in the flume, as can be seen in Figure 8. For the aligned configurations, two longitudinal transects are along the sparse and dense vegetation patch, and the other two are along the unvegetated part of the flume. All four longitudinal transects are along either the sparse or the dense vegetation patch for the staggered configurations.

4.1.1 Aligned Configurations

Figure 16 shows the four longitudinal profiles of the depth-averaged flow velocities for the four different aligned configurations. In the aligned spatial configurations, the flow exhibits the typical features of a wake flows downstream of a porous medium (Nepf, 2012c). For example, the depth-averaged flow velocities start already to decelerate upfront of the upstream vegetation patch and keep decelerating inside the vegetation patch. Meanwhile, the flow velocities accelerate in the adjacent unvegetated zone.

The flow rapidly decreases within the upstream vegetation patch until up to a particular exit velocity. The percentage of flow velocity decrease inside the upstream patch is defined by subtracting the upstream patch's exit velocity from the upstream patch's entrance velocity and dividing it by the entrance velocity of the upstream patch. It turns out that the velocity decrease inside the upstream vegetation patch is 15% larger for a dense patch compared to a sparse vegetation patch (Table 4). In the wake of the upstream patch, the flow velocity recovers due to the mixing of the faster flow from the adjacent unvegetated zones. The recovery percentage of the flow velocity has been defined as the difference between the flow velocity at the leading edge of the downstream vegetation patch and the flow velocity at the leading edge of the upstream vegetation patch and dividing it by the flow velocity at the leading edge of the upstream vegetation patch. The spatial configurations with more spacing between the two vegetation patches show an equal or more significant recovery of the flow velocities compared to the spatial configurations with less spacing between the vegetation patches (Table 4).

Remarkable is that the recovery for the dense-sparse configuration is a positive percentage (5%), meaning that the flow velocity at the leading edge of the sparse (downstream) patch is higher than the flow velocity at the leading edge of the dense (upstream) vegetation patch. This positive recovery percentage could be because the turbulence induced by the dense vegetation patch promotes the mixing between the slow and the fast-moving flow velocity layers.

The percentage of flow velocity decrease in the downstream patch has been defined similarly to the upstream patch flow velocity decrease. The flow velocity decrease in the downstream patch is lower when compared to a configuration with the same patch type upfront. For example, the velocity decrease in a dense vegetation patch in a sparse-dense configuration is 11% lower than in a dense-sparse configuration. The same holds for comparing the sparse vegetation patch in a dense-sparse configuration with a sparse vegetation patch in a sparse-dense configuration.

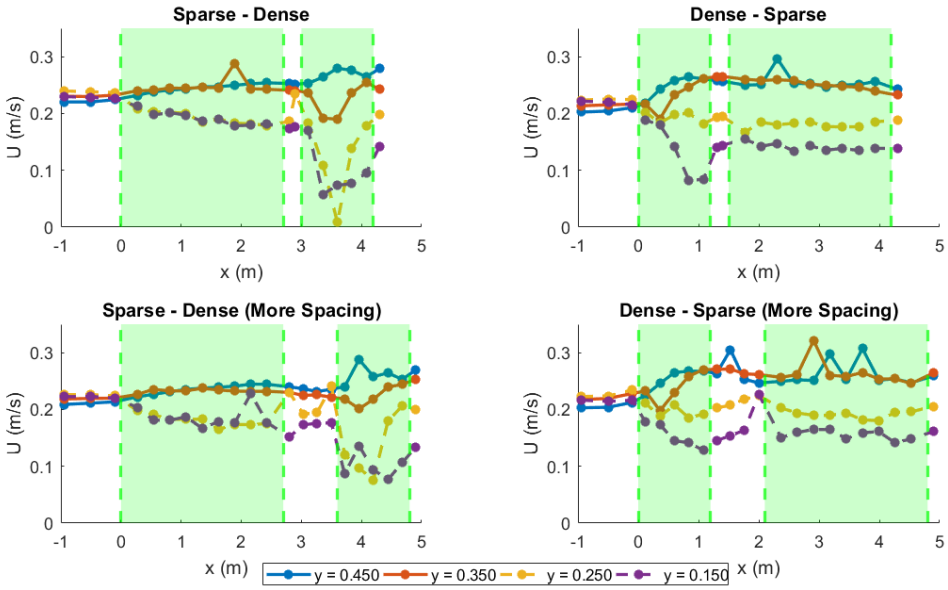

Figure 16 Longitudinal development of the streamwise depth-averaged flow velocities of the aligned configurations (Run B, Run D, Run F, Run G). The flow direction is from left to right. The solid lines represent the two longitudinal profiles along the adjacent unvegetated area. The dashed lines are the longitudinal profiles within the sparse and dense vegetation patch. The locations of the vegetation patches are indicated with green shaded rectangles.

Table 4 Overview of the flow and wake development of the longitudinal profile along the vegetation patches in the aligned configuration based on the measured depth-averaged flow velocities.

Aligned Configurations	**Flow Velocity Decrease Upstream Patch**	**Flow Velocity Recovery**	**Flow Velocity Decrease Downstream Patch**
Sparse – Dense	-23%	-23%	-29%
Sparse – Dense (more spacing)	-27%	-23%	-29%
Dense – Sparse	-40%	-30%	0%
Dense – Sparse (more spacing)	-35%	5%	-24%

4.1.2 Staggered Configurations

Figure 17 shows the contour plot of streamwise flow velocity for all the staggered configurations. For all configurations, the flow velocities decelerate in the upstream vegetation patch and at the same time increase in the adjacent unvegetated area. The spacing between the patches does have an impact on the wake development of the upstream patch. A smaller spacing between the vegetation patches shows higher flow velocity in the unvegetated area adjacent to the upstream vegetation patch compared to the same spatial configurations with larger spacings.

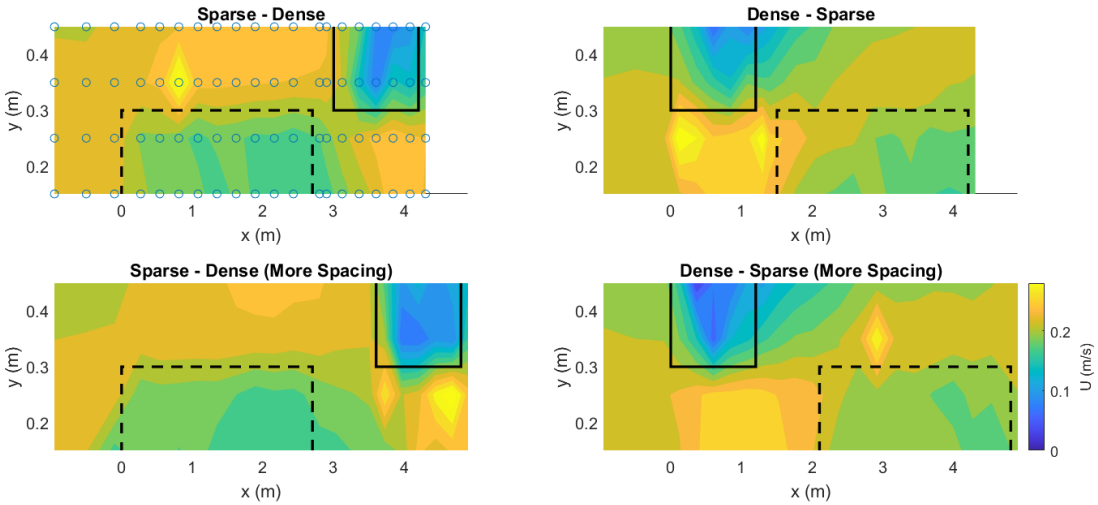

Figure 17 Top view of the flow showing the longitudinal streamwise velocity of the staggered configurations. The flow direction is from left to right. The dashed black rectangles indicate the sparse vegetation patches and the solid rectangles indicate the dense vegetation patches. The rounds in the first contour plots indicate the measurement grid.

In a staggered configuration, the flow velocity decrease in the dense vegetation patch in the dense-sparse configuration is roughly 24% larger compared to a sparse patch in a sparse-dense configuration (Table 5). This flow velocity decrease in the upstream vegetation patches in the staggered spatial configurations is larger compared to the upstream vegetation patches in the aligned configurations.

Next, for all staggered spatial configurations, the development of the wake of the upstream vegetation patch is affected by the spacing between the vegetation patches, as the flow is squeezed through the relatively small spacing between the vegetation patches. The spatial configurations with a smaller spacing result in a higher flow velocity at the leading edge of the downstream patch compared to the spatial configurations with more spacing between the vegetation patches.

Table 5 Overview of the flow and wake development of the longitudinal profile along the vegetation patch in staggered configurations based on the measured depth-averaged flow velocities.

Staggered Configurations	**Flow Velocity Decrease Upstream Patch**	**Flow Velocity Recovery**	**Flow Velocity Decrease Downstream Patch**
Sparse – Dense	-23%	35%	-43%
Sparse – Dense (more spacing)	-18%	11%	-35%
Dense – Sparse	-47%	140%	-25%
Dense – Sparse (more spacing)	-42%	100%	-14%

Finally, for comparison of the staggered configuration with aligned configurations, the longitudinal profiles of the depth-averaged streamwise flow velocities of the staggered configurations can be found in Appendix A.

4.2 Cross-Section Mean and Turbulent Flow Field Study

Three different vegetation patches were investigated in a field study, ranging from two relatively sparse vegetation patches with *Carex Sylvatica* (Locations 1 and 3) to one more dense vegetation patch with *Sparganium emersum* (Location 2).

Figure 18 shows the normalized transverse distribution of the streamwise mean velocity of the different vegetation patches. In order to be able to compare between the different measurement locations, the flow velocities have been normalized by the maximum streamwise velocity (U_{max}) measured at each transect and the width of the vegetation patches (Table 6). There is a velocity difference between the time-averaged flow velocity outside the vegetated zone ($y/b > 1$) and time-averaged flow velocity inside the vegetated zone ($y/b < 1$) (Table 6). Comparing the flow velocities in the non-vegetated zone and the vegetated zone, it can be seen that the degree of velocity reduction depends on the vegetation patch density. A denser vegetation patch leads to an absolute larger flow velocity difference.

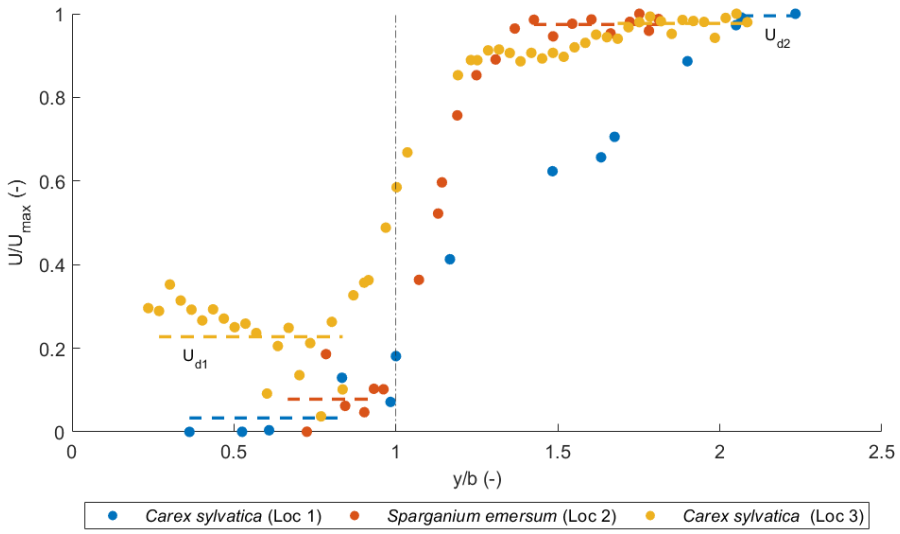

Figure 18 The transverse (y-direction) distributions of the streamwise flow velocity at the different locations normalized with the maximum streamwise flow velocity (U_{max}) and the patch width (b). U_{d1} and U_{d2} are the time-averaged flow velocities in the vegetated and non-vegetated zones indicated with the dash lines for the different locations. The vertical dashed line indicates the edge of the vegetation patch.

The flow velocity differences between the vegetated and the non-vegetated zone of the channel produce a shear layer, which follows a classical mixing layer of a hyperbolic tangent at the second and third locations (Raupach et al., 1996). There exists an inflection point near the lateral edge of the vegetation patch. Such an inflection point indicates that Kelvin-Helmholtz instabilities could develop (Ghisalberti and Nepf, 2002). In the first location with the sparse *Carex sylvatica*, a clear inflection point is not visible in the transverse mean flow velocity distribution. Furthermore, the shear parameters are 0.9, 0.8 and 0.6 for the first, second and third measurement locations. This indicates that the flow velocity difference between the vegetated and the non-vegetated zone is large enough to develop Kelvin-Helmholtz vortices at all measurement locations.

Figure 19 provides the normalised turbulent kinetic energy and the three individual normal Reynolds stress components in the transverse distribution. The Reynolds stresses and the TKE is normalised by the maximum streamwise velocity squared. It can be seen that the streamwise normal Reynolds stress has the largest contribution to the turbulent kinetic energy for all three measurement locations. The more dense *Sparganium emersum* vegetation patch (location 2) shows the largest normal stresses compared to the other vegetation patches. The absolute values of the turbulent kinetic energy and the three normal Reynolds stress components can be found in Table 6. Furthermore, the peak of the normalised kinetic energy is approximately at the interface between the vegetated and the non-vegetated zone for the second and third locations. However, for the sparse *Carex sylvatica* patch

(location 1), the normal Reynolds stresses show a sharp increase at the inner edge of the vegetation patch. Nevertheless, the Reynolds stresses at this location do not reduce gradually towards the inner side of the bare channel. This behaviour of the Reynolds stresses could be due to the fact that the patch density is not dense enough or the effect of the inner band of the channel gives this increase of Reynolds stresses. The last possibility is that the Reynolds stress peak is not measured due to the relatively large spacing at the interface between the vegetated and the non-vegetated zone. Based on this observation and the lack of a clear inflection point visible in the transverse mean flow velocity distribution, the first measurement location is neglected in further analysis.

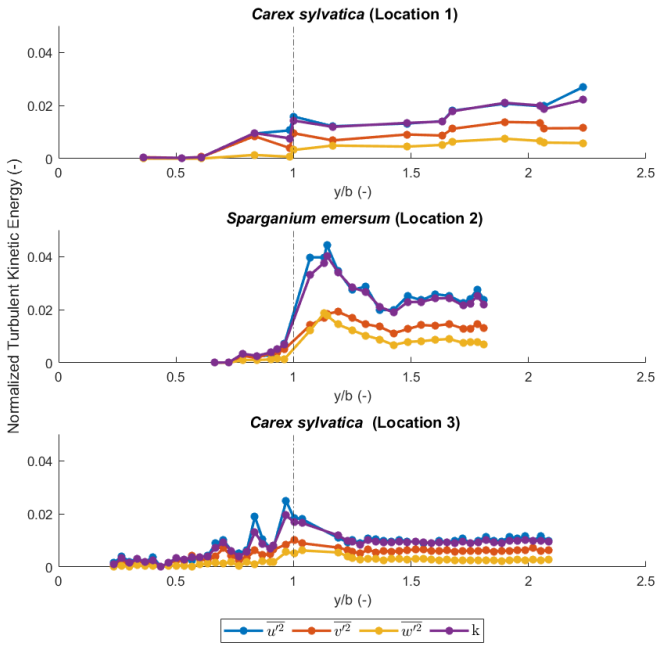

Figure 19 The transverse distribution of the Reynolds stresses and the turbulent kinetic energy per unit mass (k) at the different locations normalized with the maximum flow velocity squared (U_{max}) and the patch width (b). The vertical dashed line indicates the edge of the vegetation patch.

Table 6 Overview of the hydrodynamic parameters of the vegetated and the non-vegetated zones. The flow velocity difference between the vegetated zone (U_{d1}) and the non-vegetated zone (U_{d2}). The flow velocity at the interface between the vegetated and the non-vegetated zone ($U_{y=b}$) and the maximum values of the turbulent kinetic energy and the maximum normal Reynold stresses.

Species (Location)	$\boldsymbol{b}$ **(m)**	$\boldsymbol{U_{d1}}$ **(m/s)**	$\boldsymbol{U_{d2}}$ **(m/s)**	$\boldsymbol{U_{y=b}}$ **(m/s)**	$\boldsymbol{TKE_{max}}$ **(m/s)²**	$\boldsymbol{\overline{u'^2}_{max}}$ **(m/s)²**	$\boldsymbol{\overline{v'^2}_{max}}$ **(m/s)²**	$\boldsymbol{\overline{w'^2}_{max}}$ **(m/s)²**
***Carex sylvatica* (Location 1)**	1.20	0.014 ± 0.06	0.419 ± 0.02	0.08 ± 0.05	0.0039	0.0048	0.0024	0.0013
***Sparganium emersum* (Location 2)**	1.69	0.044 ± 0.09	0.548 ± 0.03	0.11 ± 0.07	0.0127	0.0140	0.0061	0.0059
***Carex sylvatica* (Location 3)**	1.50	0.119 ± 0.08	0.511 ± 0.05	0.30 ± 0.07	0.0053	0.0068	0.0028	0.0017

The shear layer could lead to the formation of coherent Kelvin-Helmholtz vortices, which make a large contribution to the mean transverse turbulent Reynolds shear stress ($\overline{u'v'}$) (Nepf, 2012c; Raupach et al., 1996). The transverse distribution of the mean transverse Reynolds stress is given in Figure 20. For

the *Carex sylvatica* patch, this peak is approximately at the interface between the vegetated and the non-vegetated zone. For the *Sparganium emersum* patch, the peak is just outside of the vegetation patch. The maximum transverse Reynolds stresses are 0.0033 m^2/s^2 and 0.015 m^2/s^2, respectively, for the *Sparganium emersum* patch and the *Carex sylvatica* patch.

Two distinct regions can be identified: a region of high shear stress across the interface, which determines the length scale over which momentum can penetrate the vegetation and the region of shear outside the vegetation patch indicating the penetration depth into the bare channel. Furthermore, comparing Figure 18 and Figure 20, it can be seen that the maximum Reynolds stress coincides with approximately the inflection point of the transverse velocity profile.

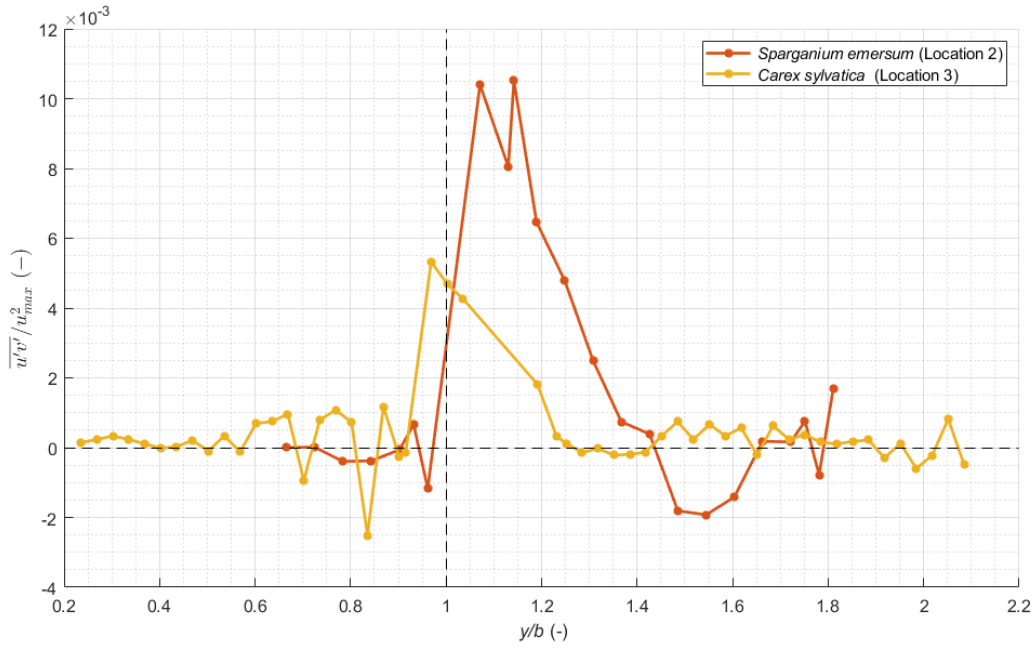

Figure 20 Transverse distribution (y-direction) of the shear Reynolds Stresses ($\overline{u'v'}$) for the different vegetation patches normalized with the maximum flow velocity squared (U^2_{max}) and the patch width (b). The horizontal line indicates the points with no turbulent momentum transport. The vertical line indicates the interface between the vegetated and the non-vegetated zone.

The outer layer of the flow velocity profile in this study does not scale with this classical boundary that can be approximated by a quadratic boundary profile (Equation 17), because the velocity profile is relatively symmetrical, meaning that the matching and inflection points are close to each other in the case of the two layered model ($y_0 \approx y_m$) (White and Nepf, 2008). Therefore, the velocity profile resembles a more symmetrical mixing profile, and it can be better approximated by a hyperbolic tangent (i.e., Equation 16). A non-linear regression to the hyperbolic tangent has been performed on which the inner and outer mixing widths are defined. The penetration distance into the vegetated zone is defined as the 90% velocity change between the time-averaged flow velocity at the vegetation edge and the time-averaged flow velocity in the vegetated zone. For the penetration distance into the main channel is defined as the 90% of velocity change between the time-averaged flow velocity at the inflection point and the time-averaged flow velocity in the vegetated and the non-vegetated zone (Huai et al., 2019; Liu et al., 2022). The inflection is determined at the point where the velocity gradient dU/dy reaches the maximum value. Furthermore, the Reynold shear stresses are calculated according to $T_{xy} = -\rho\overline{u'v'}$.

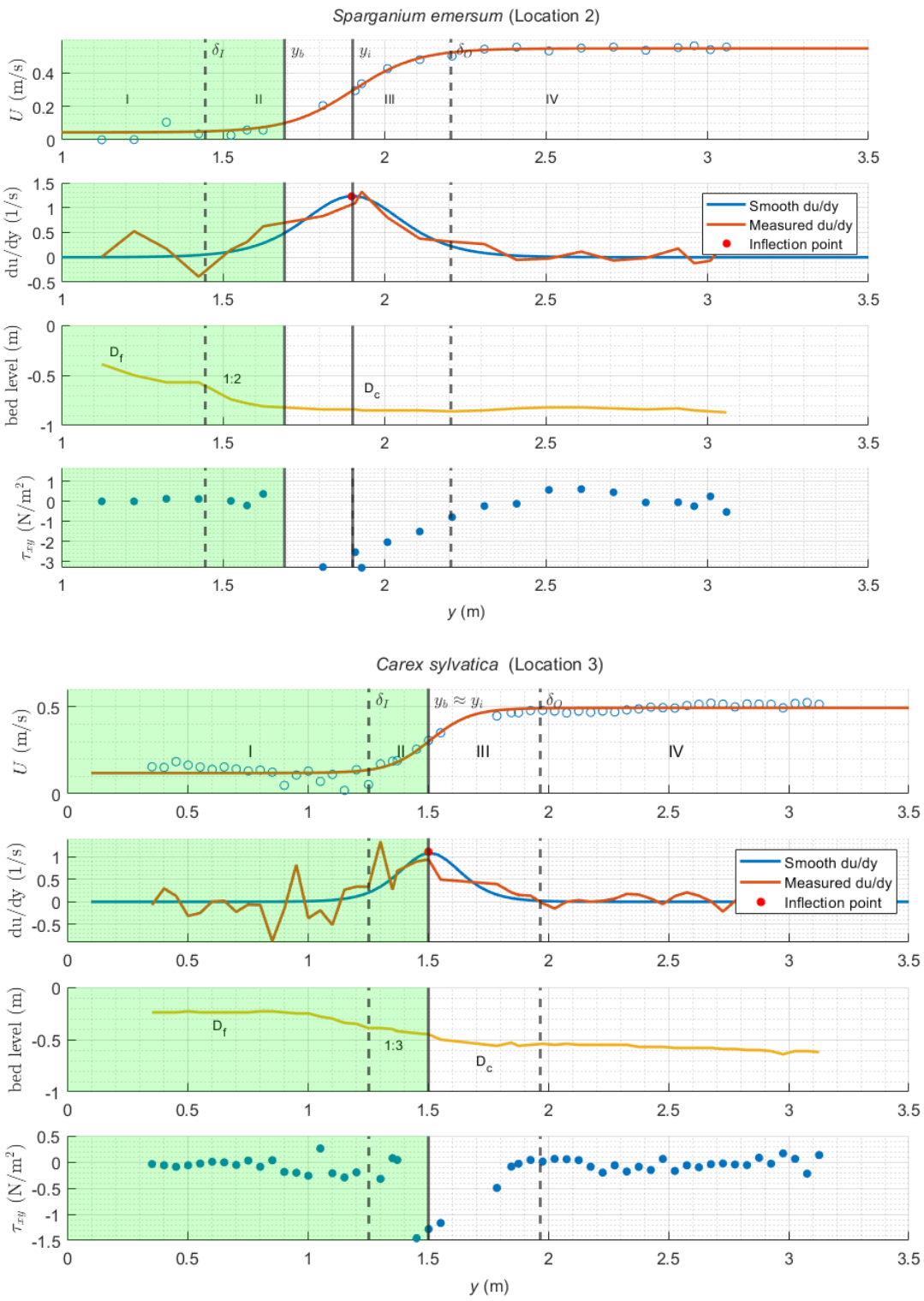

Figure 21 The mean streamwise flow velocity profiles for locations 2 and 3 with the hyperbolic tangent fit. The four different regions are defined: I) inside the vegetation, II) and III) mixing regions and IV) outside of the vegetation. δ_I is the penetration depth into the vegetation and δ_O is the penetration depth into the channel. y_b represents the edge of the vegetation patch. Furthermore, the graph containing the bed level also provides the depth of the vegetated riverbank and channel with the slope between them. Lastly, in the bottom graph, the shear Reynold stresses are presented. The vegetation is indicated with green shaded rectangles.

Figure 21 shows that the typical streamwise velocity profile is divided into four regions, as explained in the Theoretical Framework. For the *Sparganium emersum* patch, the inflection point is 20 centimetres outside the vegetation patch. The inflection point coincides with the vegetation edge for

the *Carex sylvatica* patch. In Table 7, the values for the mixing widths can be found, and the location of the inflection points and the vegetation edge is provided. A comprehensive comparison between these measured mixing widths and the empirical formulae given in the literature will be performed in the following sub-section.

Table 7 Overview of the characteristic mixing width lengths at the different measurement locations. The inner (δ_I) and outer (δ_O) mixing layer width is calculated by the 90% velocity change (as explained in the previous subsection). The horizontal location of the edge between the vegetated and the non-vegetated zone (y_b) and the inflection point (y_i) is relative to the riverbank ($y = 0$). The water depth in the channel (D_c) and the vegetation patch (D_f) is the spatially averaged of both areas.

Species (Location)	$\boldsymbol{\delta_o}$ **(m)**	$\boldsymbol{\delta_I}$ **(m)**	$\boldsymbol{y_i}$ **(m)**	$\boldsymbol{y_b}$ **(m)**	$\boldsymbol{D_c}$ **(m)**	$\boldsymbol{D_f}$ **(m)**	**Slope (-)**
Sparganium emersum **(Location 2)**	0.30	0.24	1.90	1.69	0.83	0.45	1:2
Carex sylvatica **(Location 3)**	0.46	0.24	1.50	1.50	0.59	0.25	1:3

In Figure 22, the power spectral density of the transverse velocity fluctuation (v') at the four different regions is illustrated. The spectral analysis is based on the Welch method (Welch, 1967) with a Hamming window type. It can be seen that the energy is transferred from large-scale eddies into smaller-scale eddies, which follows Kolmogorov's decay rate (-5/3) (Nikora, 2010a), which is typical for vegetation patches in open channel flow (Kitsikoudis et al., 2020; Nezu and Sanjou, 2008). The inertial subrange starts at the point where the energy spectra follow Kolmogorov's decay rate, and the turbulence is isotropic, starting at approximately 0.4 Hz for the *Sparganium emersum* patch (location 2) and 0.8 Hz for *Carex sylvatica* patch (location 3). Furthermore, the power density spectra of the transverse fluctuations in the outer mixing layer (region III) show notable peaks with a -3 slope in both locations corresponding to the quasi 2-D large horizontal Kelvin-Helmholtz vortices ($f < f_{filter} = 0.2\ \mathrm{Hz}$) (Uijttewaal and Booij, 2000). The aforementioned dominant frequencies and their power become lower when going into the vegetation (regions I and II), indicating that the vegetation blocks the formation of large-scale Kelvin-Helmholtz vortices. The decrease of power of the dominant frequencies in regions I and II is more significant for the more dense *Sparganium emersum* patch than for the sparser *Carex sylvatica* patch, indicating that the patch density influences the penetration depth of the vortices into the vegetation patch.

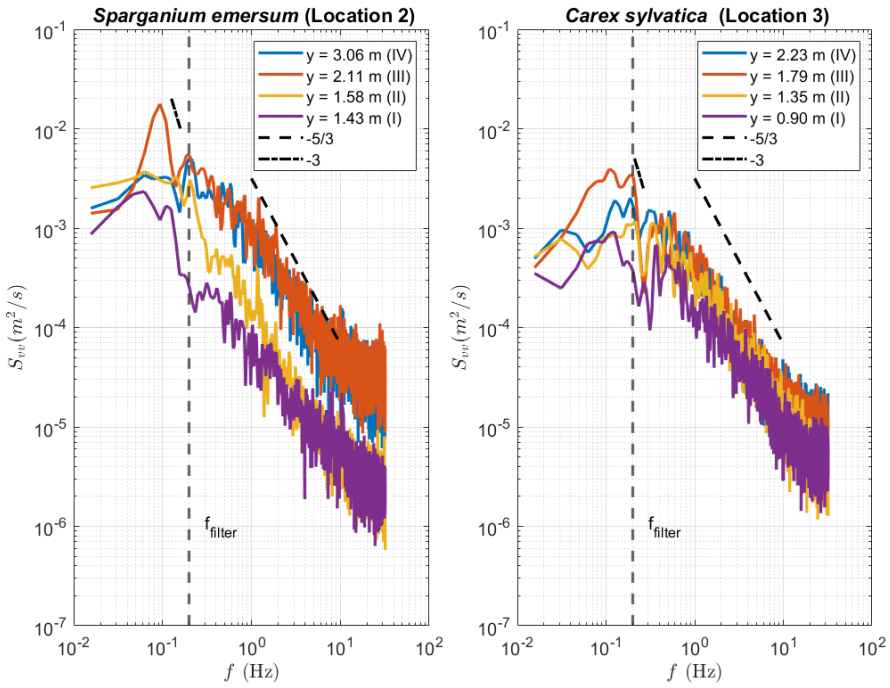

Figure 22 The power spectral density graph of the transverse fluctuating flow velocity (v') at four locations along the cross-section for the two measurement locations. f_{filter} indicate the difference between large and small-scale turbulence (Truong and Uijttewaal, 2019).

Furthermore, the frequency of the transverse flow velocity fluctuations is normalized by the momentum thickness (θ) using Equation (37) and arithmetic mean of the time-averaged velocities in the vegetated and the non-vegetated zones ($\overline{U}$) similar as done in Huai et al. (2019) and White and Nepf (2007).

$$\theta = \theta_1 + \theta_2 = \int_{-\infty}^{\infty} \left[\frac{1}{4} - \left(\frac{U_d - \overline{U}}{\Delta U} \right)^2 \right] dy \tag{37}$$

The velocity difference (ΔU) is the difference between time-averaged velocities in the vegetated and the non-vegetated zone. The momentum thickness is 0.115 and 0.247 meters for the *Sparganium emersum* patch and the *Carex sylvatica* patch, respectively. In Figure 23, the normalized transverse flow velocity fluctuations are provided, and the vertical dashed line indicates the natural frequency of the Kelvin-Helmholtz vortices at the interface ($f_n \approx 0.032$). According to free shear layer theory, the coherent structures passing by have a natural dimensionless frequency of 0.032 (Ghisalberti and Nepf, 2002; Ho and Huerre, 1984; White and Nepf, 2007). For the *Sparganium emersum* patch, the dominant normalized frequency is close to the natural frequency of the Kelvin-Helmholtz vortices at the interface of the vegetation patch. This is indicative of the possibility of the formation of coherent Kelvin-Helmholtz vortices. For the *Carex sylvatica* patch, the dominant frequency does not match the natural frequency of the Kelvin-Helmholtz instabilities. This could be due to the fact that the measurements at the third location have been taken within the adjustment region. In this region, the flow is not fully developed, which means that the Kelvin-Helmholtz vortices will not be fully developed at the lateral edge of the vegetation patch (White and Nepf, 2007). The observations of the *Sparganium emersum* patch align with those of rigid cylinders (White and Nepf, 2007) and artificial flexible vegetation patches (Huai et al., 2019).

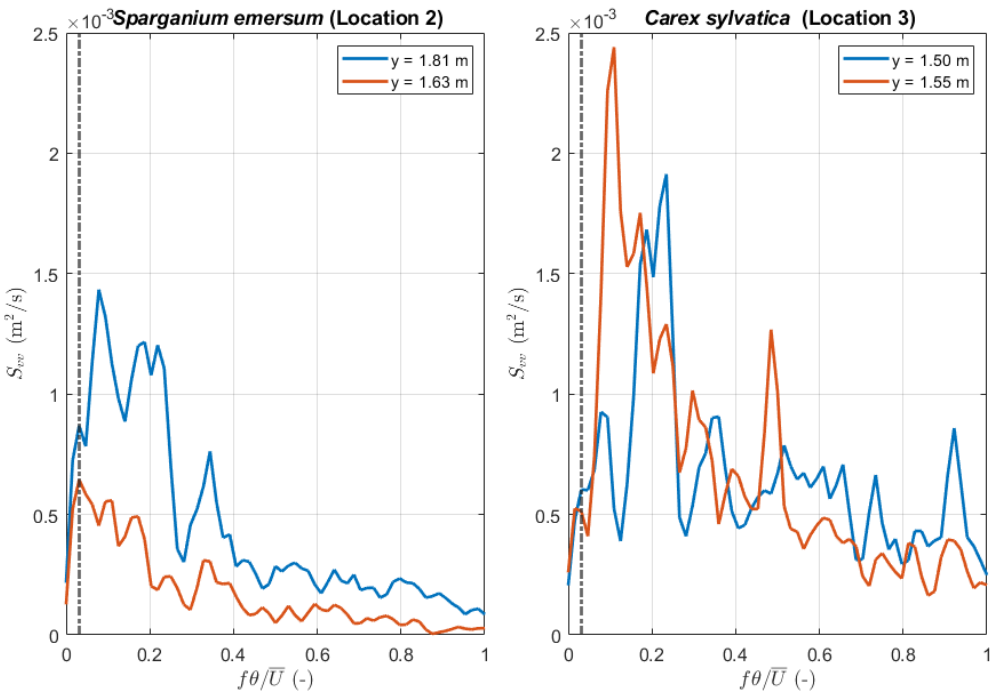

Figure 23 The Power Density graph with normalised frequencies of $v'(t)$ for the y-positions around the vegetation edge for measurement locations 2 and 3. The natural frequency for a free shear layer $\frac{f_n\theta}{\overline{U}} = 0.032$ is given with the dashed line. The vegetation edge are $y_b = 1.69$ m and $y_b = 1.50$ m respectively for locations 2 and 3.

The dimensionless Strouhal number is used to get insight into the characteristic length of the vortex frequency (Huai et al., 2019). The Strouhal number describes this relation between the vortex shredding frequency and the length size of the vortices (Equation 37).

$$St = \frac{fL}{U} \tag{38}$$

In which f is the dominant vortex shedding frequency, L is the characteristic length of the vortex shedding, and U is the approach velocity towards the obstacle (Huai et al., 2019). However, in this field measurement no approach velocity upstream of the vegetation has been measured. Therefore, the local measured flow velocity at the corresponding transverse position of the dominant vortex shedding frequency has been used as the approach velocity towards the obstacle. Across a wide range of Reynolds numbers and for different vegetation densities, the Strouhal number is constant at approximately 0.21 (Poggi et al., 2004; Zong and Nepf, 2012). Furthermore, the field-scale analysis of flexible vegetation by Caroppi et al. (2022) has shown that in the case of foliated flexible vegetation, the dominant frequency corresponds to a Strouhal number of approximately 0.2. As this Strouhal number is constant, it can be used to calculate the characteristic length of the vortex size.

In Table 8, the dominant vortex frequencies of the four different regions for the two measurement locations are given. The characteristic vortex length at the outer mixing layer (region III) is the largest for both measurement locations, which shows the formation of Kelvin-Helmholtz vortices in the horizontal plane. Furthermore, the characteristic vortex length size is roughly of the same order in the outer mixing layer for both vegetation patches, suggesting that the vortex length depends on the characteristics of the bare channel instead of the characteristics of the vegetation patch. The points well within the vegetation patch (region I) have a characteristic vortex length of approximately 0.15 meters. This vortex size is approximately the size of the average spacing between the individual stems

of the vegetation patch. This shows that the vortices that develop within the vegetation patch are mainly due to the wake production of the stems, and the growth of the vortices is bounded by the spacing between the individual stems, which is in accordance with observations in literature with artificial rigid and flexible vegetation patches (e.g., Huai et al. (2019) and White and Nepf (2008).

Table 8 Overview of dominant vortex frequencies and the associated characteristic vortex size at mid-depth.

	***Sparganium emersum* (Location 2)**				***Carex sylvatica* (Location 3)**			
Region	I	II	III	IV	I	II	III	IV
Dominant Frequency (Hz)	0.06	0.06	0.09	0.20	0.125	0.21	0.10	0.19
Vortex Length size (m)	0.12	0.20	1.12	0.58	0.11	0.19	0.98	0.52

The definite peaks associated with low-frequency signals ($f < f_{filter}$ = 0.2 Hz) are associated with the formation of Kelvin-Helmholtz in the horizontal plane (Uijttewaal and Booij, 2000). In order to be able to compare the contribution of these Kelvin-Helmholtz vortices to the total transverse shear stress, the peak regions have been separated from the other higher-frequency signal using a low-pass filter. Figure 24 shows the dominant contribution of the Kelvin-Helmholtz vortices to the total turbulent shear stress. The Reynolds shear stress induced by the Kelvin-Helmholtz vortices is more than 90% of the total Reynolds shear stress, which complies with the observations of vegetated compound channels with rigid cylinders of Truong and Uijttewaal (2019). However, it should be noted that the absolute values of the Kelvin-Helmholtz induced transverse shear stress can be larger than the absolute values of the total transverse shear stress, as the small-scale motions in the flow may be correlated differently. Furthermore, it can be seen that for the *Carex sylvatica* patch, there is a sharp decrease in the Reynolds stress at the edge of the inner layer (x = 1.25), which presumably can be interpreted as the limited distance of the penetration of the Kelvin-Helmholtz vortices into the vegetation (Truong and Uijttewaal, 2019). For the *Sparganium emersum* patch, this sharp decrease in the Reynolds stress at the edge of the inner layer is not observed.

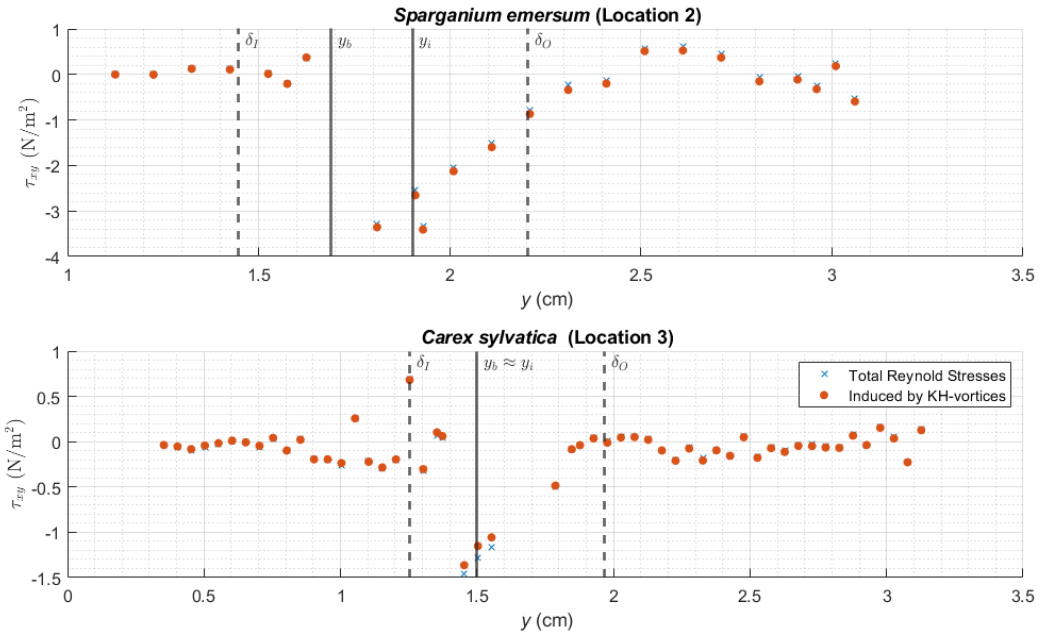

Figure 24 The transverse distribution of the total Reynolds Shear stresses and the contribution of the Kelvin-Helmholtz (KH) vortices to the total Reynolds shear stress for measurement locations 2 and 3.

Quadrant analysis of the Reynolds shear stress is performed in order to provide insightful information on the contribution of momentum exchange to the turbulent shear stress from various events in the flows (Wallace, 2016). There are four quadrants that are associated with the four different events. These four different Reynolds stress contributions depend on the instantaneous velocity fluctuations in the horizontal (u') and vertical direction (v'):

1) Outward Interaction ($u' > 0 \ \wedge v' > 0$)
2) Ejection ($u' < 0 \ \wedge v' > 0$)
3) Inward Interaction ($u' < 0 \ \wedge v' < 0$)
4) Sweeps ($u' > 0 \ \wedge v' < 0$)

In order to get some insight into the momentum exchange of the generated coherent Kelvin-Helmholtz vortices, a joint frequency distribution (JFD) of the turbulent flow velocity fluctuations in the streamwise and lateral directions has been conducted. In this joint frequency distribution, both fluctuating components are random variables. In Figure 25, the joint probabilities of these random events for the different regions of the cross-section can be found. In order to get the mean at zero and a standard deviation of one, the streamwise and the lateral direction have been normalised by their corresponding turbulence intensities ($\sqrt{\overline{u'^2}}$, $\sqrt{\overline{v'^2}}$).

The joint frequency distribution analysis of the quadrants (Figure 25) shows more frequent major events in the second and the four quadrants (ejections and sweeps) in the outer mixing layer (region III). The mode of the joint frequency distribution is for both locations in the second quadrant, specifying that the ejections are the most dominant event type. The patterns inside the vegetated zones (region I and region II) clearly denote that there is not a dominant type of one of the specific events. In the bare channel (region IV), the inward interactions and the ejects dominate. However, the spread between the different events is much larger in the bare channel than in the vegetated zones. This could be because the turbulence that arises in region II penetrates into the bare channel.

Sparganium emersum **(Location 2)**

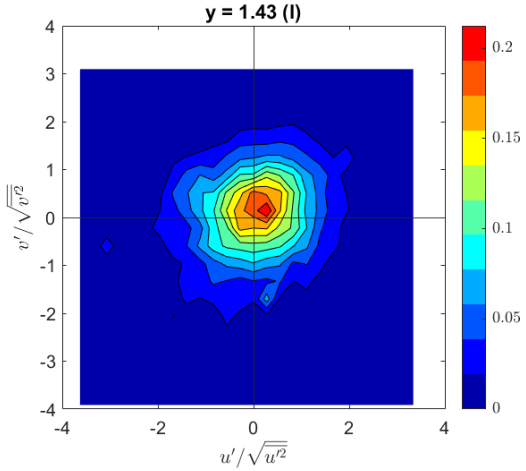

Carex sylvatica **(Location 3)**

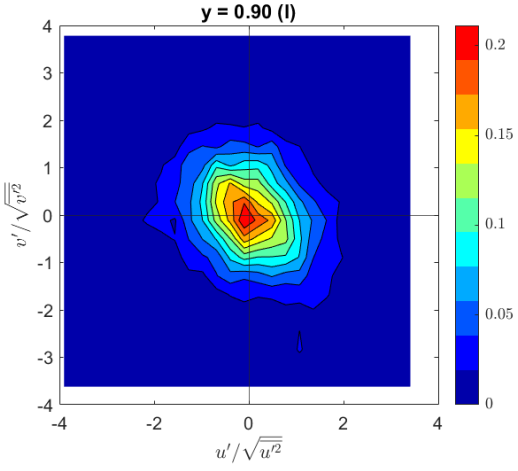

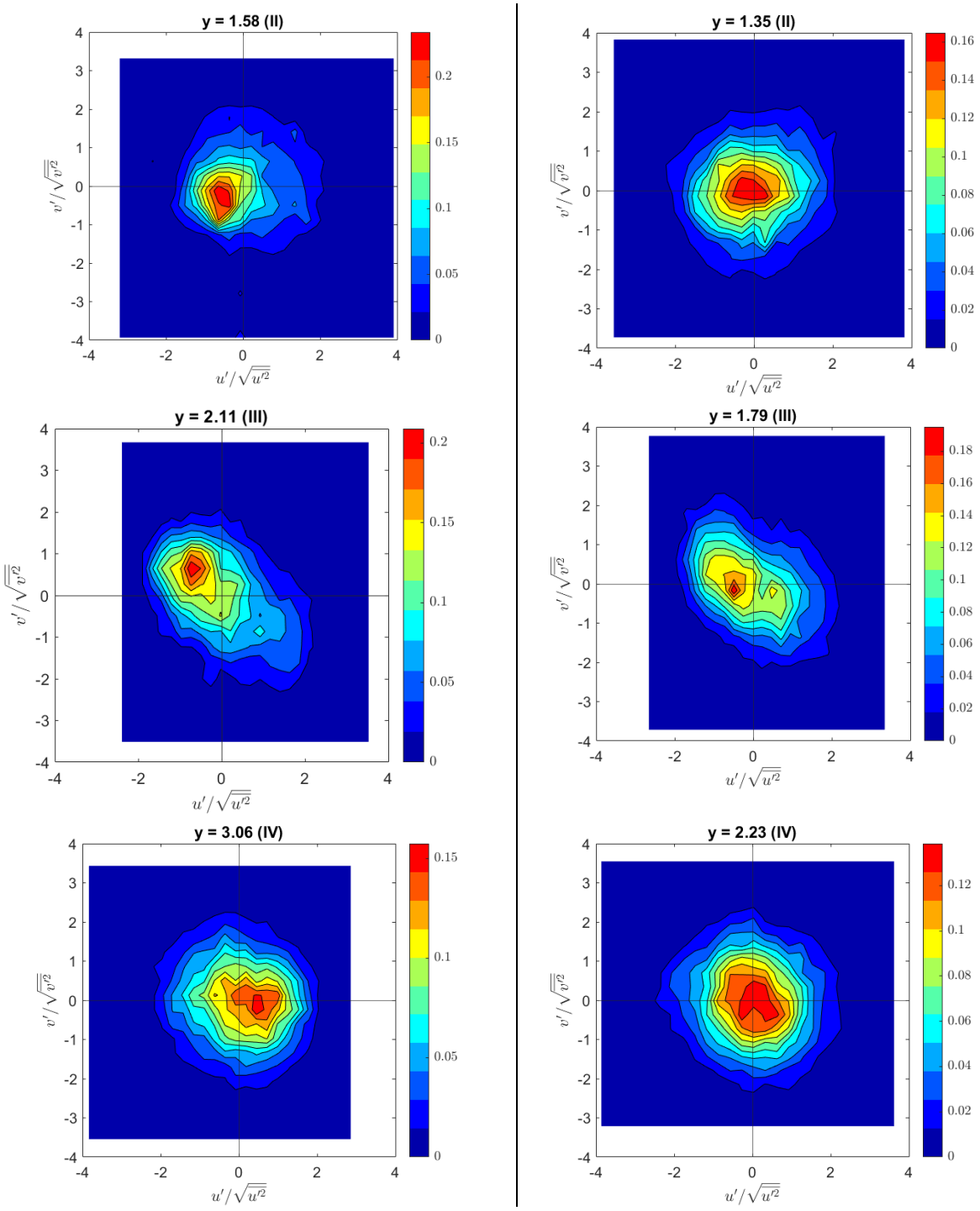

Figure 25 Joint frequency distribution of normalised longitudinal flow velocity fluctuations and the transverse flow velocity fluctuations at the four different regions.

Another analysis has been performed to get insight into the ratio of different quadrants over the cross-section using the bursting cycling detection method (Franca et al., 2014). Therefore, the contribution ratio of the different quadrants (S_i) have been expressed as the contribution of the Reynolds Stress in a certain quadrant divided by the sum of the total contribution of the Reynolds Stresses in all four quadrants.

$$S_i = \frac{\sum|u'v'|_{Qi}}{\sum|u'v'|_{Q1,2,3,4}} \tag{39}$$

The transverse distribution of the contribution of the different quadrants is presented in Figure 26. As can be seen, the ejections (Q2) and sweeps (Q4) are the main contributors to the total Reynolds Stress in the outer mixing layer (region III) at both measurement locations. The ejections and sweeps show a gradually decreasing trend from the interface to the vegetated and the non-vegetated zone, which could give insight into the penetration depth of the vortices into the channel and the vegetation patch. For the *Carex sylvatica* patch, the edge of the outer mixing layer (δ_O) coincides with the point at which the four quadrants show again equal contributions. For the *Sparganium emersum* patch, this point of equal contribution of the four quadrants is not clearly visible.

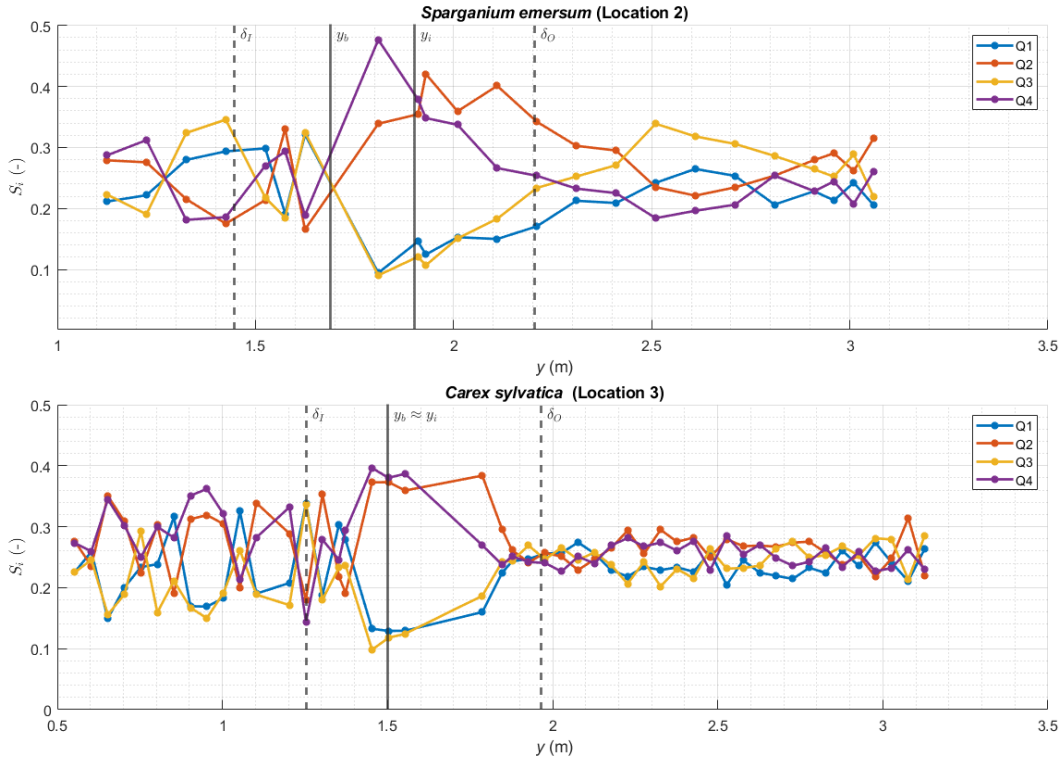

Figure 26 Contribution of the different Reynolds stress types from each quadrant. S_i indicates the ratio of the i-th quadrant to the total Reynolds stress.

4.3 Application of Existing Formulae to the Field Data

In this section, the measured parameterisations will be compared with the different semi-empirical formulae existing in the literature. In addition, whether needed, the relations will be adjusted to be more representative in describing the flow-vegetation interaction in the field. First, the different characteristic widths of the mixing layers of the different regions (such as δ_O and δ_I) will be compared to formulae proposed in the literature. Next, the determination of the drag coefficient will be discussed shortly. After this, the exponential-based model of Liu et al. (2022) will be evaluated and compared to the measured transverse streamwise velocity profile. Lastly, the representativeness of the two layered vortex-based model and the hybrid eddy viscosity model will be discussed.

4.3.1 Mixing Layer Characteristics

The standard deviation of the vegetation patch characteristics was considered when evaluating the theoretical semi-empirical formulae using the error theory propagation. This theory states that the uncertainty in the output of an equation can be determined by propagating the standard deviations in the input variables through the variance formula (Equation 40) (Ku, 1966):

$$s_f = \sqrt{\left(\frac{\partial f}{\partial x}\right)^2 s_x^2 + \left(\frac{\partial f}{\partial y}\right)^2 s_y^2 + \left(\frac{\partial f}{\partial z}\right)^2 s_z^2 + \cdots} \quad (40)$$

In which s_f represents the standard deviation of the function f, s_x represents the standard deviation of x, s_y represents the standard deviation of y and so further.

White and Nepf (2008) propose that the penetration depth into the vegetation depends on a combination of the drag coefficient and frontal area per canopy volume or the stem diameter (Equation 2). Another empirical formula to determine the penetration depth into the vegetation patch has been proposed by Liu et al. (2022) (Equation 35) based on their flume study analysis and the data of White and Nepf (2007). This empirical formula relates the velocity change in the vegetated zone using the mean of the e-folding length scales to the penetration depth into the vegetation patch. The e-folding length scale is the length over which the streamwise flow velocity decrease with a factor of e.

In order to use the empirical formulae of White and Nepf (2008), the drag coefficient of the vegetation patch is calculated. The drag coefficient of the vegetation patch is assumed to be 1. This assumption is valid for rigid cylinders and artificial flexible emergent vegetation (Huai et al., 2019; White and Nepf, 2008). Lastly, different analytical models are not very sensitive to variations in the drag coefficient (Huai et al., 2019; Liu et al., 2022).

Table 9 compares the measured and the two theoretical penetration depths derived by the above-mentioned empirical formulae. As explained in the previous research question, the actual penetration depth is defined as the 90% velocity change between the time-averaged flow velocity at the vegetation edge and the time-averaged flow velocity in the vegetated zone. The empirical formula of White and Nepf (2008) performs quite well (Equation 2), as for both measurement locations, the measured penetration depth falls within the standard deviation of the estimated penetration depths calculated using the error propagation formula. However, the estimated standard deviation of the penetration depth into the vegetation patch of the third measurement location is quite significant compared to its mean value. This large standard deviation is due to the significant standard deviation in the average vegetation patch height, which propagates into the estimated penetration depth. However, the observed discrepancy, where the measured penetration depth is smaller than the penetration depth predicted by White and Nepf (2008), contradicts the findings of a flume study conducted by Caroppi et al. (2021). The study by Caroppi et al. (2021) observed higher shear penetration into the vegetation of natural form compared to rigid cylindrical structures. It is important to note, however, that the shear penetration in the flume study by Caroppi et al. (2021) is defined based on the decay of Reynolds stress to 10% of its maximum value within the vegetation, and the penetration depth is not depending on the transverse flow velocity change such as in White and Nepf (2008) and this study.

The method of Liu et al. (2022) (Equation 35) overestimates the penetration depth into the vegetation at both locations. At the second location, the penetration depth is even larger than the width of the vegetation. Furthermore, the penetration depth into the denser *Sparganium emersum* patch (location 2) is even larger than the sparse *Carex sylvatica* patch (location 3), which does not correspond with the actual measurements and estimates of White and Nepf (2008). The cause of this is since the method of Liu et al. (2022) to determine the mean of the local e-folding length scale cannot handle flow velocity measurements lower than the time-averaged flow velocity inside the vegetation patch. In the *Sparganium emersum* patch, many measurement points are lower than the steady time-averaged flow velocity (Figure 22). Therefore, the local e-folding length scale could be determined only for three measurements inside the vegetation patch. Thus, the mean e-folding length scale is only depending on

three measurements. This reason shows that the method of Liu et al. (2022) is unsuitable for vegetation patches and does not approach a uniform time-averaged flow velocity inside the vegetation patch. Another downside of this method is that it still depends on flow velocity measurements to determine the e-folding length scales, and a prior determination of the penetration depth is impossible.

Table 9 Comparison of the measured penetration depth into the vegetation patch with the two theoretical penetration depths based on the empirical formula of White and Nepf (2008) and Liu et al. (2022). The mean values and the standard deviations are provided for the theoretical penetration depths.

Penetration depth into vegetation (δ_I) (m)	**Measured (90% velocity change)**	**White and Nepf (2008)**	**Liu et al. (2022)**
***Sparganium emersum* (Location 2)**	0.24 m	0.17 ± 0.09 m	2.41 ± 0.30 m
***Carex sylvatica* (Location 3)**	0.24 m	0.39 ± 0.32 m	0.71 ± 0.09 m

In region (III), the outer mixing layer depends on the water depth and the bed friction according to the scaling relation (Equation 3) (White and Nepf, 2007). The scaling relationship is tested on the different measurements to see if a simple empirical relationship depending on a newly introduced constant (α) can be set up:

$$\delta_O = \alpha \frac{u_*^2}{U_2^2} \frac{2h}{c_f} \tag{41}$$

The bed friction in the Dinkel is approximated based on the flow velocity measurements at the points most far into the main channel (y = 2.68 m) by using the Law of Wall theory, which states that flow velocity distribution of turbulent flow follows a logarithmic profile which can be described by the following formula (Umeyama and Gerritsen, 1992):

$$u = \frac{u_*}{\kappa} \ln\left(\frac{z}{z_0}\right) \tag{42}$$

In which u_* is the friction velocity, κ is the von Karman constant which is equal to 0.4 and z_0 is the roughness length. The friction velocity and the roughness length were determined by linear interpolation of the flow velocity measurements in depth on a logarithmic plot. The roughness length can be converted to a Nikurandse Roughness (k_s) which is $k_s = 33z_0$ for hydraulic rough flows. The Chèzy coefficient and the bed friction coefficient were calculated using the following equations:

$$C = 18log10\left(\frac{12h}{k_s}\right) \tag{43}$$

$$c_f = \frac{g}{C^2} \tag{44}$$

The bed friction is 0.0053, corresponding to a Chèzy coefficient of 43 $m^{1/2}/s$. This range of values represents a rough channel, as the value of the Chèzy coefficient ranges typically from 30 $m^{1/2}/s$ (small rough channels) up to 90 $m^{1/2}/s$ for large smooth channels (Chanson, 2004).

The water depth of the main channel and the previously calculated bed friction is used to test the scaling relation of the water depth and the measured penetration depth into the bare channel. In Table 10, it can be seen that this simple scaling relation depending on α does not hold as there is already a large spread for the two measurement locations, meaning that there are unknown phenomena or

processes that impact the length of the outer mixing width. For example, the slope of the compound channel or the relation between the floodplain water depth and the channel depth could affect the length of the outer mixing layer. Furthermore, the limited number of experiments in this study restricts the level of insight into the scaling relationship, necessitating further analysis to elucidate the precise underlying mechanisms governing this scaling relationship.

Table 10 Overview of the parameters in the scaling relation as provided in Equation (41). The penetration depth into the bare channel (δ_O) is measured using the 90% velocity change between the time-averaged flow velocity at the vegetation edge and the time-averaged flow velocity in the vegetated zone. The patch width (b) and water depth (h) is measured at the field side. And the bed friction (c_f) is determined using Equation (44).

Species (Location)	δ_o (m)	b (m)	h_c (m)	$2h/c_f$ (m)	α (-)
***Sparganium emersum* (Location 2)**	0.30	1.69	0.83	313.21	11.47
***Carex sylvatica* (Location 3)**	0.46	1.50	0.59	222.64	27.80

Liu et al. (2022) proposed an empirical formula (Equation 18) that assumes a constant mixing width of the outer layer with respect to the vegetation patch width. This field study examines the applicability of this constant to the patch width, and the width of the outer layer is examined. However, it is evident that this constant does not hold in this particular study, as it can be seen that the patch width over the penetration depth into the bare channel does not is constant (Figure 10). Nonetheless, since this empirical formula is the only available method for estimating the width of the outer mixing layer without field flow velocity measurements, it will be utilized in the exponential-based model for direct comparison with the field measurements.

Table 11 shows the differences between the measured outer layer mixing width into the bare channel and the theoretically derived outer layer mixing width. The results demonstrate considerable deviations between the measured and derived penetration depths into the outer channel. Notably, even in cases where the vegetation patch had a smaller width, the measured penetration depth was found to be larger, contradicting the findings of Liu et al. (2022).

Table 11 Comparison between the measured penetration depth into the bare channel based on the 90% flow velocity change and the theoretical penetration depth derived using the empirical formula of Liu et al. (2022) (Equation 18).

Penetration depth into the bare channel (δ_O) (m)	Measured (90% velocity change)	Liu et al. (2022)
***Sparganium emersum* (Location 2)**	0.30 m	1.06 ± 0.24 m
***Carex sylvatica* (Location 3)**	0.46 m	0.94 ± 0.21 m

4.3.2 Exponential-Based Model

Liu et al. (2022) have proposed an analytical exponential model to predict the transverse velocity field in partially vegetated channels. Its effectiveness has been validated using various flume studies, including those conducted by Caroppi et al. (2020), Huai et al. (2015) and White and Nepf (2007, 2008). This section will discuss the representativeness of this exponential-based model on field measurements.

In order to use the exponential-based model, it is necessary to determine the two key parameters: the e-folding length scales for the bare channel and the vegetated zone. The e-folding length scales can be determined using the empirical equations presented by Liu et al. (2022) (Equations 34 and 35). These empirical equations rely on the inner and outer mixing layer widths. These mixing widths could be determined by the 90% flow velocity change or estimated based on the semi-empirical formulae of White and Nepf (2008) (Equation 2) for the inner mixing layer width and the empirical formula of Liu et al. (2022) (Equation 18) for the outer mixing layer width. Lastly, flow velocity measurements can directly derive the e-folding length scales (Equations 30 and 31). This analysis considers and compares all three approaches against the actual measured flow velocities. Table 12 provides an overview of the different e-folding lengths through these different methods.

Table 12 Comparison of the three different methods to derive the e-folding length scales ($L_{d(bare)}$ and $L_{d(veg)}$). The first method of White and Nepf (2008) and Liu et al. (2022) uses the characteristics of the vegetation patch, and the 90% velocity change and the mean local e-folding length scales depend on the flow velocity measurements.

	White and Nepf (2008) and Liu et al. (2022)		**90% Flow velocity change**		**Mean local e-folding length scales**	
E-folding length scales	$L_{d(bare)}$ **(m)**	$L_{d(veg)}$ **(m)**	$L_{d(bare)}$ **(m)**	$L_{d(veg)}$ **(m)**	$L_{d(bare)}$ **(m)**	$L_{d(veg)}$ **(m)**
***Sparganium emersum* (Location 2)**	0.68	0.05	0.15	0.06	0.30	0.77
***Carex sylvatica* (Location 3)**	0.60	0.12	0.15	0.11	0.34	0.23

To utilize the exponential-based model, it is also essential to specify the incoming flow velocity, the channel width and the steady flow velocity inside the vegetation patch. Since the incoming flow has not been directly measured, the maximum mean flow velocity for each measurement location has been used. Additionally, the total transverse length of the measurement locations has been utilized to determine the channel width. The flow velocity within the fully developed region inside the vegetation patch is calculated based on the vegetation characteristics, as described in Equation 26. The water depth is the average water depth inside the vegetation taken, and the water surface slope is assumed to be 10^{-4}. For clarity, Table 13 provides an overview of the input parameters of the exponential-based model. It can be seen that the estimated steady flow velocity in the fully developed region inside the vegetation patch is slightly lower compared to the actual flow velocity measurements inside the vegetation zone.

Table 13 Overview of the input parameters of the exponential-based model. For the upstream incoming flow velocity (U_0), the maximum mean streamwise flow velocity for each measurement location has been used. The channel width (B) is based on the width of the total transverse length of the measurement location. The steady flow velocity in the fully developed flow region ($U_{1(f)}$) is calculated using Equation (26).

Input parameters Exponential-Based model	U_0 **(m/s)**	B **(m)**	$U_{1(f)}$ **(m/s)**	U_{d1} **(m/s)**
***Sparganium emersum* (Location 2)**	0.54	1.935	0.025	0.044
***Carex sylvatica* (Location 3)**	0.51	2.774	0.038	0.119

Figure 26 illustrates the performance of the exponential-based model under different approaches for deriving the e-folding length scales. Overall, the exponential model demonstrates unsatisfactory predictions for both locations when using the abovementioned parameters. The flow velocities outside of the vegetation patch reach relatively high values. These unsatisfactory predictions could be because a smaller channel width has been used in the model than the actual channel width in the field. Furthermore, the upstream streamwise flow velocity could be an overestimation for this smaller channel width. Lastly, the performance of the exponential model inside the vegetated zone is inadequate for all three methods and differs significantly from the actual flow velocity measurements.

The model demonstrates unsatisfactory predictions when the e-folding length scales are directly derived from the actual flow velocity measurements (Equations 30 and 31). Especially within the *Sparganium emersum* patch, the model overestimates the predicted flow velocities compared to the actual flow velocities. Additionally, the width of the inner mixing is underestimated by the model. According to the model, the flow requires more distance to adjust to the slower uniform flow in the vegetated channel. In reality, this indicates a faster mixing between the slower flow and the fast-flowing layers. Notably, in the area just outside of the vegetation patch ($y \approx \delta_o$), the model estimates the flow velocities quite well compared to the actual flow measurements. It can be seen that the relative overestimation of the penetration depth into the vegetation in the second location reflects back into the overestimated flow velocities.

The second method, using e-folding length scales derived from the empirical formulae of White and Nepf (2008) and Liu et al. (2022), performs slightly better than using the directly derived e-folding length scales from the actual flow velocity measurements for the second measurement location. However, the model still tends to overestimate the flow velocity in the bare channel in both locations.

Lastly, the exponential model based on the mixing widths derived from the 90% flow velocity change performs the best for both measurement locations. The transverse streamwise velocity profile's shape is best captured using the mixing widths derived from the 90% flow velocity change.

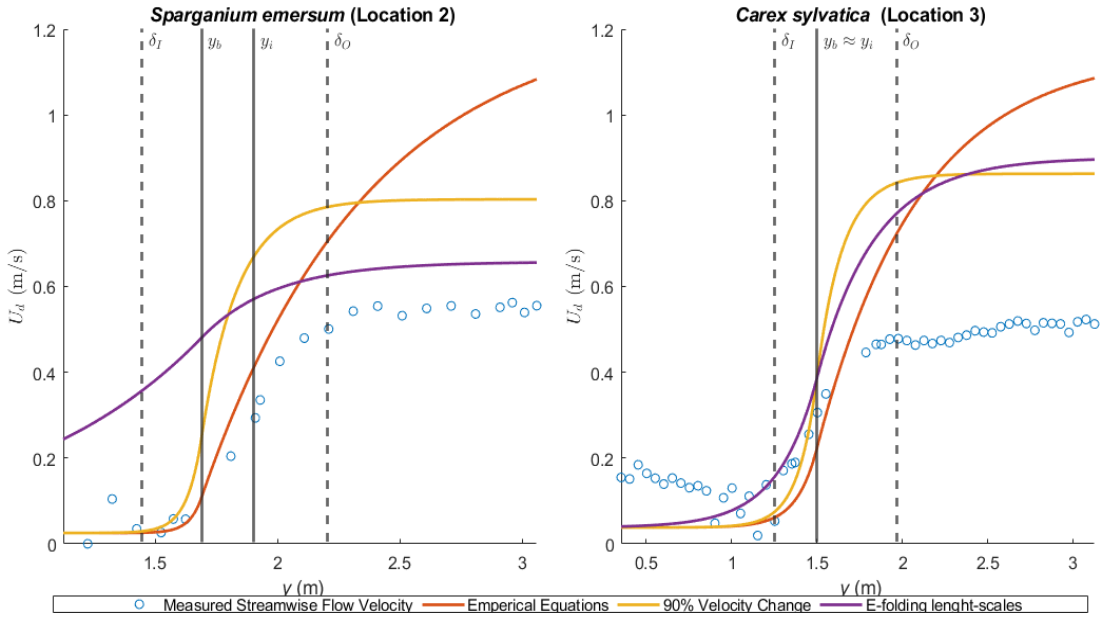

Figure 27 The predicted lateral profiles of the streamwise flow velocities based on the e-folding length scales derived from the mixing layers widths derived from the 90% flow velocity change, the semi-empirical formulae of White and Nepf (2008) and Liu et al. (2022) and directly derived from the measured flow velocities. The incoming flow velocity is 0.54 and 0.51 m/s

for measurement locations two and three, respectively. The channel width is 1.935 and 2.774 meters for locations two and three, respectively.

To gain insight into the behaviour of the model under varying input parameters, the total width is adjusted to 6 meters for both measurement locations. This adjustment closely approximates the total width of the channel as measured on Google Maps. The incoming flow velocity has remained the same and still represents the maximum mean flow velocity in the transect.

As depicted in Figure 28, the performance of the exponential-based model is notably enhanced when utilizing a more realistic vegetation channel width, in contrast to the previous results obtained with a channel width matching the transverse measurement length.

However, the model still exhibits unsatisfactory behaviour within the vegetation patch when utilizing directly derived e-folding length scales from actual flow measurements (Equations 30 and 31). The empirical estimation underestimates flow velocities for both measurement locations just outside the vegetation patch. Interestingly, the exponential model demonstrates the most accurate performance when the mixing widths are derived from the 90% flow velocity change.

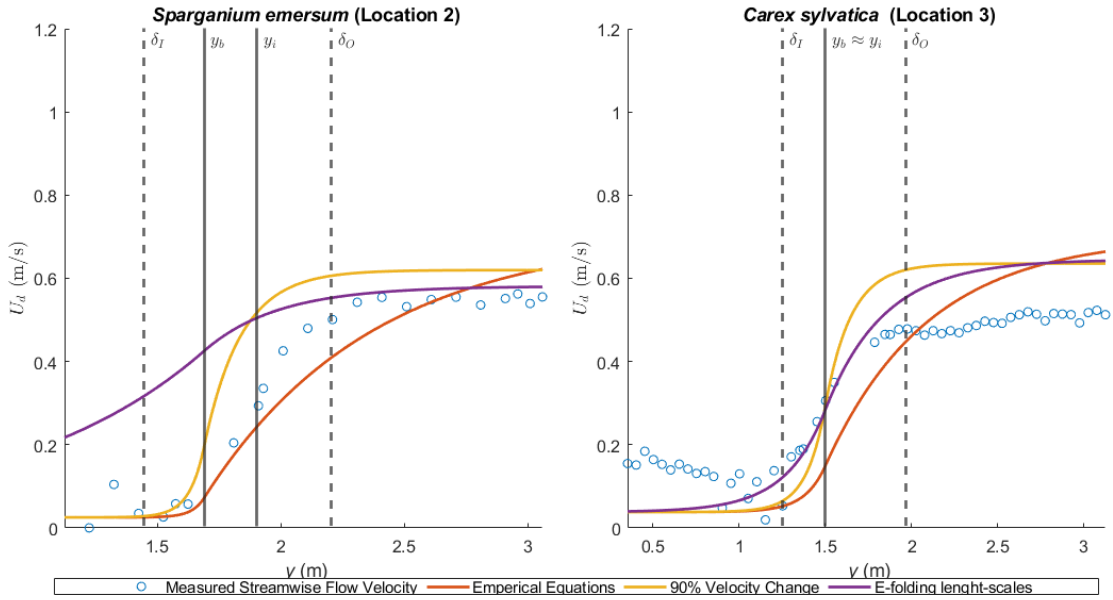

Figure 28 The predicted lateral profiles of the streamwise flow velocities based on the e-folding length scales derived from the mixing layers widths derived from the 90% flow velocity change, the semi-empirical formulae of White and Nepf (2008) and Liu et al. (2022) and directly derived from the measured flow velocities. The incoming flow velocity is 0.54 and 0.51 m/s for measurement locations two and three, respectively. The channel width is 6 meters for both measurement locations.

By adjusting the incoming flow velocity to the arithmetic mean between the maximum mean flow velocity at the transverse profile and the mean flow velocity at the side edge between the vegetated and the non-vegetated zone, the resulting flow velocities are 0.32 m/s for location two and 0.41 m/s for location 3. The channel width remains based on the width of the total transverse length of the measurement location, as outlined in Table 13.

Figure 29 shows that the exponential-based model using the lower incoming flow velocities performs slightly worse than the exponential-based model using the larger channel width. For the second measurement location, all three methods to derive the e-folding length scales underestimate the flow velocities outside the vegetation patch. For the third measurement location, there is still an overestimation of the flow velocities outside the vegetation patch.

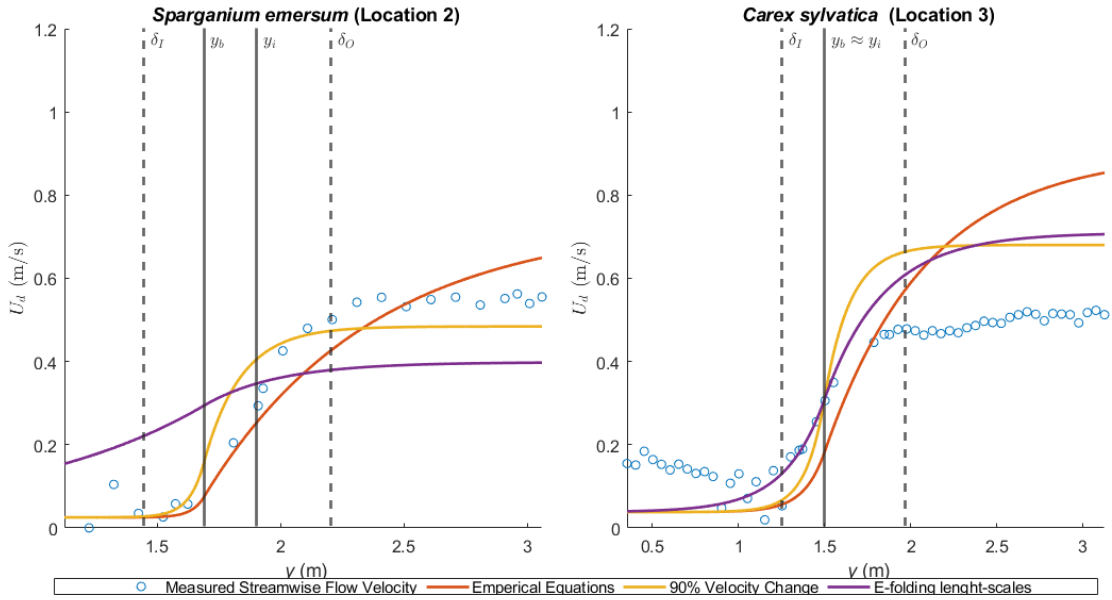

Figure 29 The predicted lateral profiles of the streamwise flow velocities based on the e-folding length scales derived from the mixing layers widths derived from the 90% flow velocity change, the semi-empirical formulae of White and Nepf (2008) and Liu et al. (2022) and directly derived from the measured flow velocities. The incoming flow velocity is 0.32 and 0.41 m/s for measurement locations two and three, respectively. The channel width is 1.935 and 2.774 meters for locations two and three, respectively.

4.3.3 Eddy Viscosity Models

In order to approximate the lateral shear stress of momentum exchange in a vegetated channel, the concept of an eddy viscosity model has been used (van Prooijen et al., 2005). This subsection aims to test the two layered vortex model proposed by White and Nepf (2008) and the hybrid eddy viscosity model developed by Truong and Uijttewaal (2019) using the actual measured transverse distribution of lateral shear stresses. The transverse shear stresses will be determined using Equation (15). In Table 14, an overview of the parameters for the two layered vortex-based model of White and Nepf (2008) is provided for reference.

Table 14 Overview of the parameters of the Vortex-based model of White and Nepf (2008). The maximum shear velocity (u_*^2) is based on the maximum shear Reynold stress. The inner (δ_I) and the outer layer (δ_O) mixing widths is calculated by the 90% velocity change. The outer and inner layer edit viscosity (ν_t) is calculated using Equation (19) and Equation (20). The flow velocity at the inflection point (U_s) is measured.

	Inner-Layer				**Outer Layer**			
	u_*^2 (m/s)²	δ_I (m)	U_s (m/s)	ν_t (m²/s)	δ_O (m)	U_2 (m/s)	U_s (m/s)	ν_t (m²/s)
***Sparganium emersum* (Location 2)**	0.0033	0.24	0.065	0.012	0.30	0.548	0.065	0.003
***Carex sylvatica* (Location 3)**	0.0015	0.24	0.181	0.0023	0.46	0.511	0.18	0.0019

Next, the hybrid eddy viscosity model of Truong and Uijttewaal (2019) is given in Equation (23). This model incorporates separate theoretical eddy viscosity inside the vegetation patch on the floodplain and outside of the vegetation. The model depends on the flow velocities and the water depths at various points along the cross-section. Additionally, the hybrid model has two empirical coefficients that must be determined beforehand.

The first coefficient (α) is a constant of order 0.1, as Fischer et al. (1979) suggested. The next coefficient, denoted as β is proportional to the slope steepness between the bare channel and the riverbank on which the vegetation patch is situated. According to Truong and Uijttewaal (2019), for slope ratios of 1:2 and 1:3, the proportional coefficients are respectively 0.15 and 0.1. It is important to note that the determination of the β coefficient is based on a limited number of flume experiments, consisting of only three cases. Therefore, the validity of this relationship will be further examined later in this section. In Table 15, an overview of the model parameters can be found.

Table 15 Overview of the model parameters of the hybrid eddy viscosity model of Truong and Uijtewaal (2019). The two coefficients (α and β) and the total mixing widths ($\delta = \delta_O + \delta_I$) based on the 90% flow velocity change.

Species (Location)	$\boldsymbol{\alpha}$ **(-)**	$\boldsymbol{\beta}$ **(-)**	$\boldsymbol{\delta}$ **(m)**
Sparganium emersum **(Location 2)**	0.1	0.15	0.54
Carex sylvatica **(Location 3)**	0.1	0.1	0.70

Figure 30 presents the theoretical eddy viscosity profile by the hybrid eddy viscosity model of Truong and Uijttewaal (2019) and the two layered vortex-based model of White and Nepf (2008). From the hybrid eddy viscosity model, the dominant contribution to theoretical eddy viscosity arises from the Kelvin-Helmholtz vortices within the vegetation patch, exhibiting a peak around the inflection point and then rapidly decreasing within the bare channel. The extent of this decrease aligns approximately with the width of the outer mixing layer. However, the inner mixing layer width in the vegetation cannot be distinctly deduced from the modelled eddy viscosity. This behaviour is in line with the observation of the quadrant analysis, which shows that the contribution of the sweeps and ejections related to the formation of Kelvin-Helmholtz vortices dominates in the area just outside the vegetation patch.

In the *Sparganium emersum* patch, it is evident that the two layered vortex-based model yields a significantly larger inner-layer eddy viscosity (not shown in the figure $v_{t,I} = 0.012$ m^2/s) compared to the hybrid model. The outer-layer eddy viscosity of the vortex-based model approximately corresponds to the total eddy viscosity modelled by the hybrid model for both measurement locations. Furthermore, going into the channel, the contribution of the bottom turbulence increases compared to the total turbulence.

Comparing the *Carex sylvatica* patch to the *Sparganium emersum* patch, the hybrid model indicates higher turbulence and lateral momentum exchange within the vegetation. The peaks inside the vegetation are due to peaks in the contribution to the eddy viscosity of the Kelvin-Helmholtz vortices. The eddy viscosity of the two layered vortex-based model corresponds to approximately the maximum viscosity of the hybrid model both inside and outside of the vegetation patch.

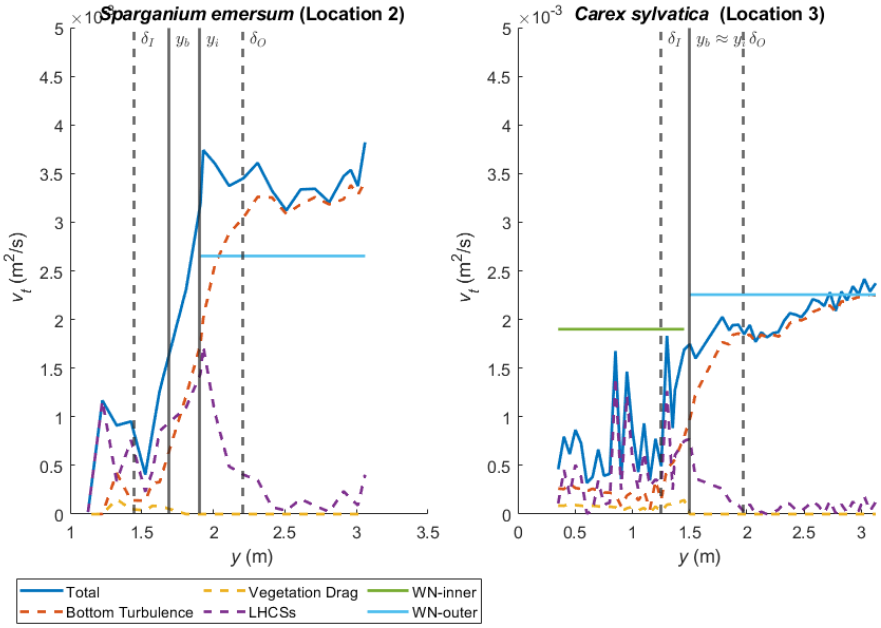

Figure 30 Eddy Viscosity profile according to the hybrid eddy viscosity model of Truong and Uijtewaal (2019) for locations 2 and 3. The total eddy viscosity is divided into bottom turbulence, vegetation drag, and large horizontal coherent structures (LHCSs). The inner layer (WN-inner) and the outer layer (WN-outer) of the two layered vortex-based model of White and Nepf are plotted as references.

Figure 31 illustrates the comparison of the transverse momentum exchange determined from the two different eddy viscosity models with the actual measured transverse shear stresses. The two layered vortex-based model produces a relatively good result deep within the bare channel. However, the model tends to overestimate the peak of the lateral momentum exchange around the inflection point and within the vegetation patch. This tendency is particularly noticeable at the second measurement location, where the inner layer theoretical eddy viscosity of the two layered vortex-based model is larger than the eddy viscosity modelled by the hybrid eddy viscosity model.

On the other hand, the hybrid eddy viscosity of Truong and Uijttewaal (2019) demonstrates better performance in modelling the transverse momentum exchange. It provides a closer match to the measured transverse shear stresses, showcasing its ability to capture the complex flow dynamics and lateral momentum transfer more accurately in the field.

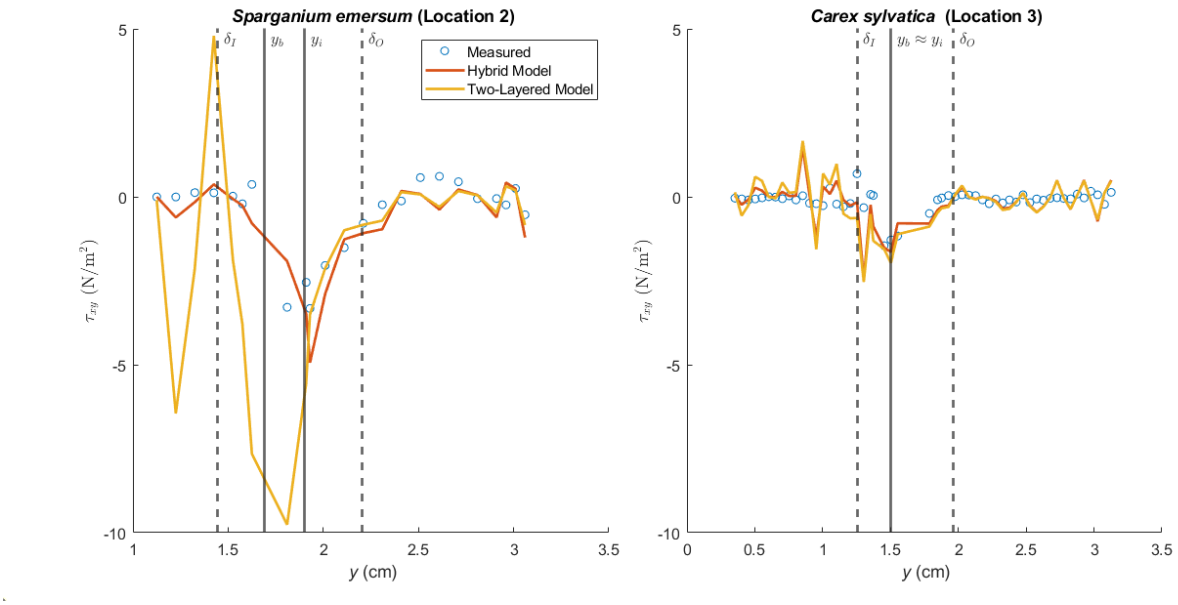

Figure 31 Comparison between the predicted transverse distribution of the $\overline{u'v'}$ Reynolds Shear stress by the hybrid model of Truong and Uijtewaal (2019) and the two layered vortex-based model of White and Nepf (2008) and the actual measurements.

Truong and Uijttewaal (2019) suggest that adjusting the proportionality coefficient allows the transverse momentum exchange determined by the hybrid eddy viscosity model to match other different experimental setups. They propose a possible relationship between the proportionality coefficient and the slope based on their flume study and three other flume experiments conducted in a compound channel with and without rigid vegetation patches (e.g., Ervine et al. (2000), Lambert and Sellin (1996) and White and Nepf (2007)).

A sensitivity analysis was conducted on this proportionality coefficient to validate the proposed relationship by slightly varying the suggested proportionality coefficient. The results of this sensitivity analysis are presented in Figure 32. For the *Sparganium emersum* patch, a slope of 0.1 best fits the

actual measured transverse momentum exchange. Similarly, for the *Carex sylvatica* patch, a slope of 0.1 best fits the measured data.

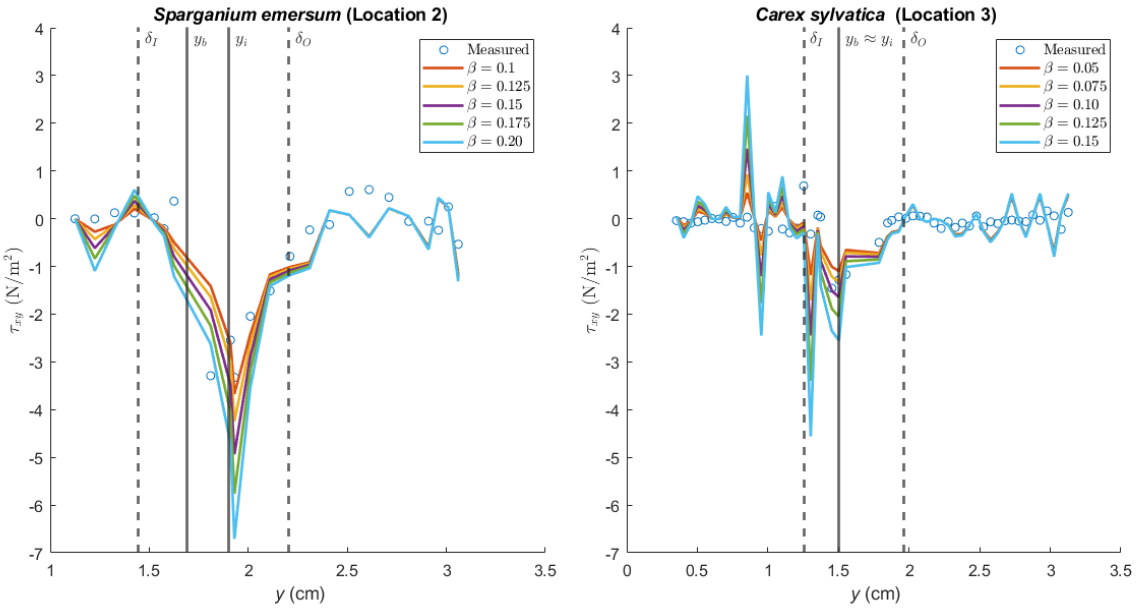

Figure 32 Sensitivity Analysis of the proportional coefficient (β) of the hybrid eddy viscosity model proposed by Truong and Uijttewaal (2019) for both measurement locations.

When comparing our slopes to the proposed relationship of Truong and Uijttewaal (2019), it can be argued that the relationship under natural conditions is less sensitive to the slope than initially suggested (Figure 33). However, it should be taken into account that in this study, there is no compound channel with a floodplain but a riverbank with a vegetation patch with a slight slope.

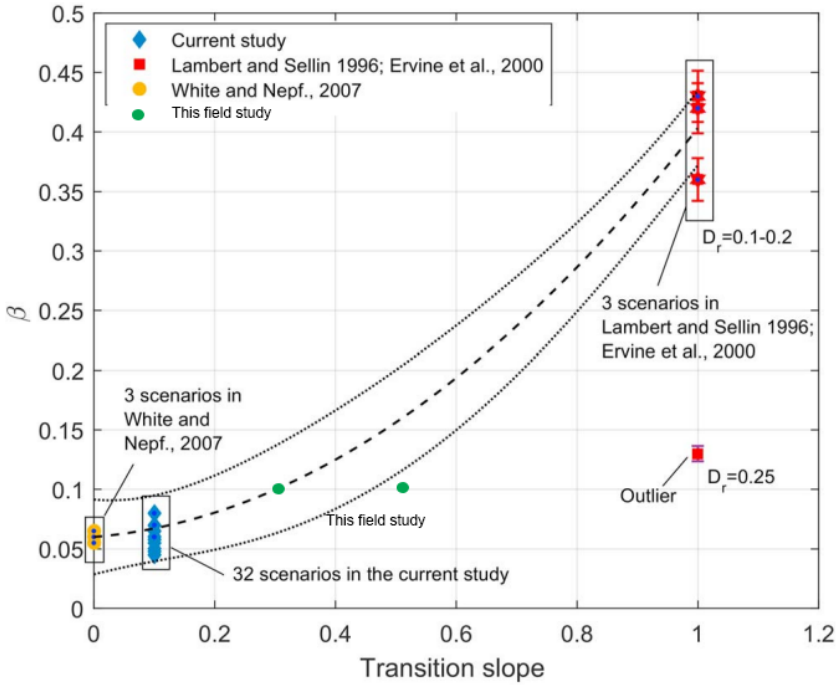

Figure 33 The suggested relationship between the proportional coefficient and the transition slope between the floodplain and the main channel based on the studies of Ervine et al. (2000), Lambert and Sellin (1996) and White and Nepf (2007) and the best fit of the proportionality coefficient in this field study. Adapted from Truong and Uijttewaal (2019).

A downside of the hybrid eddy viscosity model is that it still relies on flow velocity measurements, which must be measured in the field. However, to overcome this downside, the transverse flow velocity field of the exponential-based model of Liu et al. (2022) based on the mixing length widths estimates of White and Nepf (2008) and Liu et al. (2022) could be used as input for the hybrid eddy viscosity model. In this way, the lateral shear stress of momentum exchange in the vegetated channel can be approximated based on the vegetation and channel characteristics but without actual flow velocity measurements inside the vegetation patch. For the exponential-based model, the total width of the channel of 6 meters and an incoming flow velocity equal to the maximum mean streamwise flow velocity for each measurement location has been used.

Figure 34 compares the measured and the modelled lateral shear stress of momentum exchange in the vegetated channel. For the more dense *Sparganium emersum* patch, the predicted lateral shear stress distribution does not sufficiently capture the region of high shear stress across the interface between the vegetated and the non-vegetated zone. Furthermore, in the bare channel outside of the outer mixing layer width ($y > \delta_O$), the model over overestimates the lateral shear stress. The sparser *Carex sylvatica* vegetation patch shows better results when using the empirical estimates of the mixings widths to determine the lateral shear stress distribution. The predicted lateral shear stress distribution captures well the region of the high shear stress across the interface between the vegetated and the non-vegetated zone. However, the modelled peak of increased shear stress is larger than that of actual measured shear stress. Furthermore, the model still overestimates the lateral shear stress in the bare channel. To conclude, combining both models has much potential for a better understanding of the flow-vegetation interactions without performing actual flow velocity measurements. However, the empirical estimates of the inner and outer mixing layers should be improved to get more accurate results.

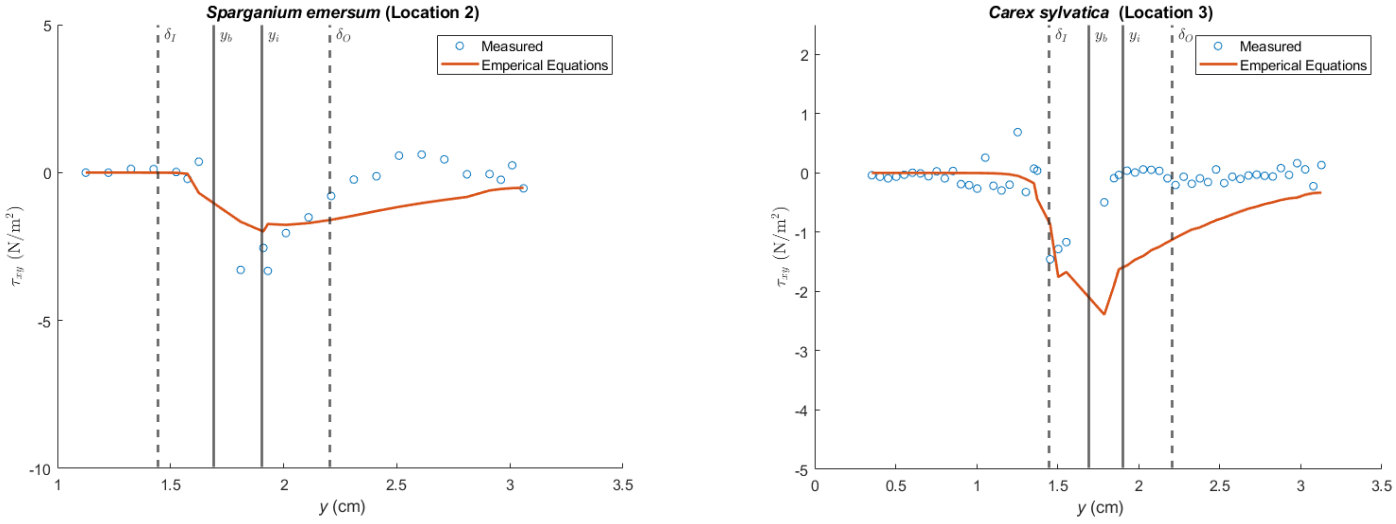

Figure 34 A comparison between the measured and the predicted lateral shear stress of the momentum exchange by the Hybrid model of Truong and Uijttewaal (2019) using the predicted flow velocities according to the exponential-based model of Liu et al. (2022) with the empirical estimates for the inner and outer mixing layer widths. The incoming flow velocities for measurement locations two and three are 0.54 m/s and 0.51 m/s, respectively, while the channel width is 6 meters.

5 Discussion

The first section of the discussion provides the significance and the novelties of this study. In the next section, the implications and assumptions are taken in this study.

5.1 Significance and Novelty

Flow-vegetation interaction has emerged as a significant concern in river management, underscoring the importance of flow-vegetation studies to understand how vegetation impacts flow patterns and vice versa. Examining this interaction is essential to gain insights into the influence of vegetation on flow and its potential implications. For instance, certain types of riverbank vegetation have demonstrated positive effects, such as mitigating erosion and bolstering bank stability (Liu et al., 2017). However, it is essential to note that vegetation can also introduce additional drag, impeding the discharge capacity of natural water flow and leading to elevated water levels (Liu et al., 2008). In order to be able to tackle these problems and provide guidelines for these management problems, analytical models are needed to be provided. The result of this study gives a first step in testing the current models of these river management problems.

Previous studies that derived the empirical formulae are, to a great extent, under the influence of many idealizations. For instance, rigid cylinders mimic natural vegetation patches (White and Nepf, 2007). Also, these artificial vegetation patches are relatively dense compared to the vegetation patches characterized in this study. For example, the sparsest vegetation patch in White and Nepf (2007) and Liu et al. (2022) have a frontal area per canopy flume of respectively 9.2 m^{-1} and 4.0 m^{-1}, which is already at the upper edge of most aquatic vegetation patches in nature (1 – 13 m^{-1}) (Lightbody and Nepf, 2006; Widdows et al., 2008) and also the vegetation patches in this study (≈2-3 m^{-1}). Furthermore, a flatbed has been used in the studies mentioned above, while the transverse depth difference does influence the formation of the shear layer (Truong and Uijttewaal, 2019; van Prooijen et al., 2005). Lastly, rigid cylinders compared to natural flexible vegetation elements significantly affect the mixing widths (Caroppi et al., 2021). Over the last decades, new state-of-the-art measurement techniques have allowed researchers to capture an abundance of flow velocity measurements within and around vegetation patches at the side (i.e., Liu et al., 2017; Rominger and Nepf, 2011; White and Nepf, 2007). These idealised flow-vegetation interactions have allowed for conceptualizing and calibrating empirical formulae.

Of course, these assumptions are quite reasonable and primarily necessary to identify and get a first understanding of the flow-vegetation interaction. The main reason and motivation for this study are that it is currently unknown what the accuracy and applicability of these derived formulae in natural streams with riverbank vegetation are. The fundamental idealised flow-vegetation interaction formulae are often not applied in field studies. As most of the field studies have a qualitative nature in which observations of different types of vegetation are directly compared to each other in a particular setting (e.g., Caroppi et al. (2022) and Przyborowski et al. (2019)). To address this knowledge gap, the analytical exponential-based model to predict the transverse mean flow velocity profile has been applied to riverbank vegetation. Additionally, the measured transverse shear stress contribution is compared with the two eddy viscosity models by White and Nepf (2008) and Truong and Uijttewaal (2019). The following sub-section will provide the implications and a comparison of the results with other studies.

5.2 Implications, Limitations and Applicability

Different assumptions have been made for some of the results obtained in this research. Furthermore, some results can be linked and compared to other studies. In this section, the assumptions, limitations and applicability of the flume study and after which the field study will be discussed.

5.2.1 Flume Study

First, flow upstream of the upstream vegetation patch in the flow begins to decelerate, continuing within the patch. This adjustment region depends on vegetation density and is analogous to the findings of Zong and Nepf (2010). By continuity, it can be stated that decreasing flow velocity inside the vegetation patch leads to increased vertical velocity outside the vegetation patch and, thereby, an increase of the streamwise flow velocity in the adjacent unvegetated area (Yan et al., 2020). With increasing downstream distance of the patch, the wake spread, and the flow recovers to its upstream equilibrium velocity (Chen et al., 2013).

One of the most considerable limitations of the flume analysis is that the flow velocities are measured at 10 Hz with a recording time of 30 seconds, resulting in only 300 sample points per measurement point. With this amount of sampling points, only the mean flow velocities stabilize, and the standard deviation of the time series does not stabilize. Therefore, only the mean flow characteristics can be used, and the turbulence characteristics of the flow cannot be described, such as the turbulent kinetic energy or a spectral or quadrant analysis of the turbulent flow events.

5.2.2 Field Study

The first implication of the results is that the vegetation density indeed plays an essential role in the vegetation drag and affects the development of the (turbulent) flow field around the patch corresponding to other flume studies (e.g., Nepf and Ghisalberti (2008) and Rominger and Nepf (2011)). As the vegetation patch in this field study is not fully emergent, a shear layer could be formed in both the horizontal and the vertical plane (Villota et al., 2023). The transverse distribution of the streamwise flow velocity represents a symmetrical horizontal shear layer corresponding with the observations in the vegetated compound channel of Trong and Uijtewaal (2019). The outer horizontal shear layer does not form a near-sinusoidal velocity distribution that bulges upward and downward, as observed in Villota et al. (2023). Therefore, it can be concluded that the vertical flow velocity of the secondary circulation is too small to adjust the outer shear layer.

Next, comparing the transverse distribution of the maximum shear Reynold stress ($\overline{u'v'}$) (Figure 20) and the transverse distribution of the streamwise flow velocity (Figure 18), it can be seen that the maximum shear Reynold stress coincides with approximately the inflection point of the transverse velocity profile, which is in line with the experiments of White and Nepf (2007, 2008). For the second measurement location, the inflection point in the transverse distribution of the streamwise flow velocity is just outside the vegetation patch. However, based on the analysis of White and Nepf (2007), the inflection point is only outside of the vegetation patch in the case of a relatively sparse vegetation patch. In this research, the third location has a lower density than the second location, which contradicts with the analysis of White and Nepf (2007). The fact that the inflection point is outside of the vegetation patch could be caused by the bed slope in the second location being much steeper, or the side edge of the vegetation patch is not dense enough to form a sharp gradient between the vegetated and the non-vegetated zone.

Subsequently, the power density spectra of the transverse fluctuations in the outer mixing layer (region III) show notable peaks with a -3 slope in both locations corresponding to the quasi 2-D large horizontal Kelvin-Helmholtz vortices (Uijttewaal and Booij, 2000) analogous to the findings of other flume studies with rigid and flexible artificial vegetation such as Trong and Uijtewaal (2019) and Huai et al. (2019).

The joint frequency distribution of the field experiments corresponds qualitatively quite well to other flume and field studies using rigid cylinders or artificial vegetation. For example, the flume studies of Trong and Uijtewaal (2019) and Huai et al. (2019) also indicate that at the interface between the

vegetated and the non-vegetated zone ejections and sweeps dominate, and inside the vegetation, all of the quadrants have an equal contribution. These observations agree with the theory that the vortex size in the bare channel is solely dependent on the channel characteristics, such as the bed friction and that the vortex size inside the vegetation solely depends on the vegetation density (Nepf, 2012c).

Overall, the observations in this field study qualitatively agree reasonably well with the observations of other flume studies which use rigid cylinders or flexible artificial vegetation (e.g., Huai et al. (2019) and Truong and Uijttewaal (2019) and White and Nepf (2007)). However, more vegetation patches in the field need to be investigated to compare the difference between natural and artificial vegetation patches quantitatively. However, by conducting the flow velocity measurements under realistic conditions, this study offers a first valuable insight into the representativeness and applicability of idealized formulae, expanding our understanding of flow-vegetation interactions in natural environments.

For example, the drag coefficient of the vegetation has been assumed to be equal to one in this study. This choice was because the different analytical models, such as the exponential-based velocity profile model, were not very sensitive to a change in the drag coefficient. However, this sensitivity has been tested by applying the models on rigid cylinders. Under natural circumstances, flexible vegetation is pushed over as the flow velocity increases, decreasing the frontal area and the drag coefficient (Caroppi et al., 2022; Nikora, 2010b; Vogel, 2020). Also, the (depth-averaged) frontal area per canopy volume has been determined at the measurement transect based on the non-deflected vegetation height and the average water depth inside the patch. Thus, the total patch flow blockage factor ($C_d a$) has been assumed constant, while it turns out that this parameter is essential for the flow-vegetation interaction.

Another limitation of this study is that the measurements are done at a subjective longitudinal distance from the leading edge of the vegetation patch. The interior adjustment length is calculated according to the equation proposed by Rominger and Nepf (2011). However, this value is inconsequent, and whether or not the location of the vegetation patch is outside its interior adjustment region is unknown. Because it is hard to determine the exact starting location of a patch, as patches do not have a sharp edge of distinct shoot density with their surroundings, or two or more patches act hydrodynamically as one vegetation patch (Kolasa, 2014). Furthermore, the interior adjustment region is based on a flume study using rigid cylinders and has not been validated in the field (Rominger and Nepf, 2011). Furthermore, it is assumed that the vegetation density was uniform throughout the patch. Therefore, it is uncertain whether or not the vegetation patch is outside of the interior adjustment region ($x > x_d$), and it is uncertain if the Kelvin-Helmholtz vortices even could develop at the measured transect.

Furthermore, the vegetation characteristics can be defined in different ways. So, the frontal area per canopy volume is initially described for using rigid cylinders. In order to be able to describe the frontal area per canopy volume of natural vegetation patches, different methods have been used. For example, for straplike vegetation types, the leaf width is used, while for vegetation with a circular stem cross-section, the stem diameter is used. In this study, the individual vegetation elements in the vegetation do not have a uniform height. Therefore, a depth-averaged value for the frontal area per canopy volume has been calculated, which already shows a significant standard deviation. A comparison of these different methods exhibits a broad range of different values.

In this study, only one transect has been measured for each vegetation patch. Ideally, the plan was to measure at more transects in the longitudinal plane and add more measurements in depth. This is to get a complete insight into the flow-vegetation interaction, such as the longitudinal growth of the

shear-layer and the shear-layer induced vortices (Rominger and Nepf, 2011) and to see if the secondary circulation contribution to the transverse Reynolds stresses is neglected as proposed by Hopkinson and Wynn (2009) and White and Nepf (2008). However, due to time constraints, the choice has been made to measure only one transect and to do more detailed measurements around the interface between the vegetated and the non-vegetated zone.

Furthermore, the flow velocity measured at $0.4h$ above the bed has been used as a proxy for the depth-averaged velocities, which is considered valid for fully developed hydraulic rough flows characterized by a logarithmic flow velocity profile (Van Rijn, 1990). This equation holds for large rivers. However, its applicability in the context of small streams with vegetated sloping riverbanks remains uncertain, as it is unclear whether the logarithmic profile still holds. To overcome this limitation in further studies, more flow velocity measurements in depth could have been used to approximate the depth-averaged flow velocities better.

Another limitation in applying the exponential-based model is that not all input parameters are directly measured. For example, to apply the exponential-based model, the width has been assumed to be equal to the total transverse measurement length for the different measurement locations. This smaller width assumes that the modelled channel is smaller than the actual channel and that there is no vertical in and outflow at the lateral boundaries of the channel. Also, the exponential-based model has been applied with an estimated channel width of 6 meters for both locations. However, this assumption is also not fully valid as the exponential-based model has been validated only at a channel with only a vegetation patch at one of the sides of the channel and not at both sides. Another assumption that has been made is that the incoming uniform flow velocity has been assumed to be equal to the maximum measured mean streamwise flow velocity in the measured transect. Another limitation of the exponential-based model is that the uniform flow velocity in the developed region inside the vegetation patch has been derived using Equation (26). The surface water slope has been assumed to be 10^{-4}. Furthermore, this equation has only been validated under idealized circumstances in a flume study with a flat bed and has not been tested in real-world field conditions.

The last point is the applicability of the existing (empirical) models to describe the flow-vegetation interaction in the field. The empirical relations for the inner and outer layer mixing widths exhibit significant deviation from the actually measured mixing widths. For example, the exponential model, heavily reliant on these estimated values, shows limited accuracy. To address this, conducting field flow velocity measurements to determine actual parameters is currently the best approach. The same holds for both eddy viscosity models, which also heavily rely on estimated values of the mixing layer widths. This study shows that both models show promising results when using the actual measured parameters. The need for actual measurements shows the limited applicability of the model in cases without actual flow velocity measurements. Improving the empirical relations would improve the applicability of the exponential-based model and the eddy viscosity models and provide deeper insights into the dynamics of flow-vegetation interactions. However, there is much potential in combining the downside of hybrid eddy viscosity, which is the actual streamwise flow velocity measurements and the advantage of the exponential-based model, which can predict the lateral profile of the streamwise flow velocities within and outside of the vegetation patch.

6 Conclusion

This chapter outlines the main findings and insights from the experiments carried out in the flume and the Dinkel with patches of natural vegetation, and this is done by answering the research questions presented in the introduction. In the end, recommendations for future research will be suggested.

1. **What is the effect of the spatial configuration of flexible vegetation patches in a flume on the longitudinal and cross-sectional development of the mean flow velocities?**

To answer this research question, the flow in and around two submerged macrophytes species, *Callitriche platycarpa* (dense patch) and *Groenlandia densa* (sparse patch), were analysed to investigate the flow-vegetation interaction in aquatic habitats. The frontal area per canopy volume was 7.70 and 1.30 for the dense and sparse patches, respectively. Two different spatial configurations were considered, the aligned configuration, representing riverbank vegetation and staggered patch configurations, representing the interaction of riverbank vegetation with instream vegetation.

The velocity decrease inside the upstream vegetation patch was 15% larger for a dense patch compared to a sparse vegetation patch in aligned configurations. In the wake of the upstream patch, the flow velocity recovered due to mixing with the faster flow from the adjacent unvegetated zones. The aligned configurations with more spacing between the two vegetation patches showed an equal or more significant recovery of flow velocities compared to configurations with less spacing.

In the staggered configurations, the flow velocity decrease in the upstream vegetation patch is larger compared to the upstream vegetation patches in aligned configurations. Furthermore, the spacing between the patches had a more significant impact on the wake development and the recovery of the flow velocities of the upstream patch, with a smaller spacing of 0.3 meters resulting in higher flow velocities in the adjacent unvegetated area and a faster recovery.

The findings mentioned above emphasize the importance of considering the interaction of different vegetation patches when studying the flow-vegetation dynamics in natural aquatic habitats and that vegetation patches close to each other do not necessarily mean that they act hydrodynamically as one vegetation patch. This can be seen as the flow recovery length in the wake of the upstream patch is larger than the spacing between the individual patches. Furthermore, the spatial configuration (sparse–dense or dense-sparse) and the spacing between the two individual vegetation patches affect the wake development and the recovery downstream of a vegetation patch. Thus, the heterogeneity and patchiness of spatial configurations in natural conditions significantly affect the mean flow distribution.

2. **How do distinctively different patches of riverbank vegetation in the field affect the distribution of the mean flow velocities and the turbulence characteristics across the river cross-section?**

This research investigated the impact of three distinctively different patches of riverbank vegetation in the Dinkel on the distribution of the mean flow velocities and turbulence characteristics. At the three different measurement locations, two different macrophytes species were found; two times the *Carex sylvatica* with a frontal area per canopy volume of 1.69 and 1.30, and one time the *Sparganium emersum* with a frontal area per canopy volume of 2.94. The study findings revealed several key insights.

Firstly, the density of the vegetation patch was found to play a crucial role in the vegetation drag and the development of the flow velocity inside the vegetation patch. The degree of velocity reduction depended on the density of the vegetation patch, with denser patches resulting in more significant

flow velocity differences. The variation between slow flow within the vegetation and faster flow in the open channel leads to the development of a shear layer. This mixing layer generates turbulence and increases flow resistance, elevating water levels. This observation shows that the density of distinctively different vegetation patches affects the distribution of the mean flow velocity and the turbulence characteristics differently.

The analysis of normalized turbulent kinetic energy and Reynolds stress components revealed that streamwise normal Reynolds stress contributed the most to the turbulent kinetic energy. The densest vegetation patch exhibited higher normal stresses in all directions compared to the other locations. Furthermore, the inflection point in the transverse distribution of the mean streamwise flow velocity almost coincides with the peak in the transverse Reynolds shear stresses ($\overline{u'v'}$). There is no clear peak visible in the transverse shear Reynolds stresses if there is no clear inflection point in the transverse streamwise flow velocity distribution. However, the inflection point does not necessarily coincide with the side edge of the vegetation patch but can also be located outside the vegetation patch. The exact mechanism causing the inflection point to be shifted into the channel is still unknown.

Normalized transverse flow velocity fluctuations provided further insight into the formation of coherent Kelvin-Helmholtz vortices. This manifestation of Kelvin-Helmholtz vortices is also visible in the frequency analysis. In the power density spectra of the transverse fluctuations in the outer layer, a notable peak with a -3 slope corresponding to the formation of large horizontal Kelvin-Helmholtz vortices is visible. Furthermore, dominant frequencies of the natural frequency of the shear-induced vortices were observed for one of the measurement locations, suggesting the possibility of vortex formation. The analysis of the characteristic length of vortex shedding indicated that the vortex size outside the vegetation patch was not influenced by the vegetation patch characteristics.

Lastly, quadrant analysis of Reynolds shear stress highlighted that the sweeps and ejections are the most dominant contributions of the momentum exchange to the turbulent shear stresses from various flow events. The dominance of Kelvin-Helmholtz vortices in the total transverse shear stress was evident, with their contribution exceeding 90%. The penetration of these vortices into the vegetation patch was observed as a sharp decrease in Reynolds stress at the edge of the inner layer. These observations match well the observations in the flume study of studies of Huai et al. (2019) and Truong and Uijttewaal (2019) with artificial and rigid vegetation, in which the ejections and sweeps dominate at the interface between the vegetated and the non-vegetated zone.

3. **How applicable are the existing semi-empirical relations describing the longitudinal and cross-sectional flow velocity distributions from flume experiments to measurements in a natural stream, and how could these relations be adjusted to be more accurate for the field?**

Different conclusions can be drawn based on the results obtained in the analysis of the field data and the comparison of various semi-empirical relations describing longitudinal, cross-sectional flow velocity distribution and turbulent shear stress.

The applicability of the two layered vortex-based model of White and Nepf (2008) and the hybrid eddy viscosity model of Truong and Uijttewaal (2019) have been demonstrated. The model of White and Nepf (2008) presents a model that demonstrates relatively accurate results compared to the actual measured transverse momentum exchange. However, it should be noted that the model tends to overestimate the peak of the lateral momentum exchange around the inflection point and inside the vegetation patch. This overestimation is particularly prominent in the second measurement location, where the inner layer eddy viscosity is considerably higher compared to the eddy viscosity modelled by the hybrid model. In contrast, the hybrid model developed by Truong and Uijttewaal (2019)

performs effectively in capturing the transverse momentum exchange. These findings suggest that the hybrid model offers a more accurate and satisfactory representation of the flow dynamics and momentum exchange in the studied system.

The existing analytical exponential-based model proposed by Liu et al. (2022) is another model which could be used to predict the transverse flow velocity profile. The model demonstrates the best predictions when utilizing mixing width derived from the 90% transverse flow velocity change instead of the empirical estimates. Furthermore, the model is quite sensitive to incoming flow conditions and the width of the channel.

Another aspect examined was the comparison of the measured penetration depth into the vegetation with the estimated values from empirical formulas proposed by White and Nepf (2008) and Liu et al. (2022). The empirical method of White and Nepf (2008) shows that the measured penetration depth falls within the error margin of the estimated penetration depths. However, the method of Liu et al. (2022) overestimates the penetration depth into the vegetation for both locations, which is because the method cannot handle flow velocity measurement lower than the time-averaged flow velocity in the vegetated zone. Therefore, the method of Liu et al. (2022) is unsuitable for vegetation patches in the field as it does approach a uniform time-averaged flow velocity inside the vegetation. Another downside of this model is that actual flow measurements are needed to calibrate and adjust the parameters. Therefore, the analytical exponential-based model proposed by Liu et al. (2022) performs poorly when using the empirical estimate mixing layer widths are used as proposed by White and Nepf (2008) and Liu et al. (2022). Therefore, new empirical formulae are required to capture accurately and to use the practical analytical exponential-based model to predict flow velocity distributions without using the results of direct field measurements.

The limitation of the hybrid eddy viscosity model is that it still relies on flow velocity measurements, to overcome this downside, the transverse flow velocity field of the exponential-based model of Liu et al. (2022) based on the mixing length widths estimates of White and Nepf (2008) and Liu et al. (2022) could be used to as input for the hybrid eddy viscosity model. This combination shows reasonable results but has a much larger potential for a better understanding of flow-vegetation interactions without performing actual flow velocity measurements. However, to get more accurate results, the empirical estimates of the inner and outer mixing layers should be improved.

The scaling relation between the water depth and bed roughness is tested using a simple scaling relation depending on a newly introduced constant. However, it turns out that this simple scaling relation does not hold. So underlying phenomena or processes might impact the penetration depth into the channel. In order to get insight into this, more measurements are needed. However, Liu et al. (2022) have proposed an empirical formula in which the mixing width of the outer layer is constant with the vegetation patch width, and it can be seen that this constant does not hold in this field study. As shown, the theoretically derived penetration depth into the outer channel is far off from the measured penetration depths. Even the patch with a smaller width has a larger measured penetration depth which is not the case according to Liu et al. (2022).

7 Recommendations

Different regions of a channel affect the formation of a shear layer and, thus, the formation of Kelvin-Helmholtz vortices. For example, the bottom roughness affects the mixing layer and the formation of Kelvin-Helmholtz vortices (Uijttewaal and Booij, 2000). Furthermore, the slope of the riverbank preserves the formation of the shear layer (Fernandes et al., 2014; Truong and Uijttewaal, 2019). Lastly, a vegetation patch locally increases the roughness compared to a bare flatbed, leading to the deflection of the flow approaching the vegetation patch. This flow divergence significantly increases the magnitude of the velocity gradient between the vegetation and the open channel flow (White and Nepf, 2007). However, in this field study, it is hard to distinguish the contribution of the components mentioned above on the formation of the shear layer, the total transverse momentum exchange, and which component is the most dominant. The contribution of the different components can be investigated by performing a flume study with different natural vegetation patches and different types of bed materials and slopes. Furthermore, these experiments could give insight into the missing parameters influencing the outer mixing widths for which only a scaling relationship currently exists. Another option is to perform field-scale measurements in which a riverbank is first planted with riverbank vegetation, and then the vegetation is removed.

It turns out that the empirical formulae to describe the inner and outer mixing layer widths are far off from the actual measured mixing widths. This shows that the empirical relations do not sufficiently capture the natural circumstances in natural streams. However, the current analytical models, such as the exponential-based model for predicting the velocity fields in partially vegetated channels and the eddy viscosity models for predicting the turbulent shear stress, depend highly on these mixing widths. More research is needed to derive new empirical formulae for the width of the outer and inner mixing layers, such that detailed flow measurements in the field are not needed to determine these parameters. For the inner layer mixing width, which primarily depends on the characteristics of the vegetation patch, a new empirical relationship can be established by measuring this mixing for different densities of sloping riverbank vegetation in a flume study. Regarding the outer mixing layer, its width depends on channel characteristics, such as the bed roughness and channel width. Therefore, to develop a new empirical relationship, the flume study must incorporate bed roughness and channel width variations.

8 Bibliography

Aberle, J., & Järvelä, J. (2015). Hydrodynamics of vegetated channels. *GeoPlanet: Earth and Planetary Sciences*, 519–541. https://doi.org/10.1007/978-3-319-17719-9_21

Bouma, T. J., De Vries, M. B., Low, E., Peralta, G., Tánczos, I. C., van de Koppel, J., & Herman, P. M. J. (2005). Trade-offs related to ecosystem engineering: a case study on stiffness of emerging macrophytes. *Ecology*, *86*(8), 2187–2199. https://doi.org/10.1890/04-1588

Caroppi, G., Gualtieri, P., Fontana, N., & Giugni, M. (2020). Effects of vegetation density on shear layer in partly vegetated channels. *Journal of Hydro-Environment Research*, *30*, 82–90. https://doi.org/10.1016/j.jher.2020.01.008

Caroppi, G., & Järvelä, J. (2022). Shear layer over floodplain vegetation with a view on bending and streamlining effects. *Environmental Fluid Mechanics*, *22*(2–3), 587–618. https://doi.org/10.1007/S10652-022-09841-W

Caroppi, G., Västilä, K., Gualtieri, P., Järvelä, J., Giugni, M., & Rowiński, P. M. (2021). Comparison of Flexible and Rigid Vegetation Induced Shear Layers in Partly Vegetated Channels. *Water Resources Research*, *57*(3). https://doi.org/10.1029/2020WR028243

Caroppi, G., Västilä, K., Järvelä, J., Lee, C., Ji, U., Kim, H. S., & Kim, S. (2022). Flow and wake characteristics associated with riparian vegetation patches: Results from field-scale experiments. *Hydrological Processes*, *36*(2), e14506. https://doi.org/10.1002/HYP.14506

Caroppi, G., Västilä, K., Järvelä, J., Rowiński, P. M., & Giugni, M. (2019). Turbulence at water-vegetation interface in open channel flow: Experiments with natural-like plants. *Advances in Water Resources*, *127*, 180–191. https://doi.org/10.1016/J.ADVWATRES.2019.03.013

Chanson, H. (2004). *Hydraulics of Open Channel Flow* (Second). Elsevier. https://doi.org/10.1016/B978-0-7506-5978-9.X5000-4

Chen, Z., Jiang, C., & Nepf, H. (2013). Flow adjustment at the leading edge of a submerged aquatic canopy. *Water Resources Research*, *49*(9), 5537–5551. https://doi.org/10.1002/WRCR.20403

Clarke, S. J. (2002). Vegetation growth in rivers: influences upon sediment and nutrient dynamics. *Progress in Physical Geography: Earth and Environment*, *26*(2), 159–172. https://doi.org/10.1191/0309133302pp324ra

Cornacchia, L., Lapetoule, G., Licci, S., Basquin, H., & Puijalon, S. (2023). How to build vegetation patches in hydraulic studies: a hydrodynamic-ecological perspective on a biological object. *Journal of Ecohydraulics*, 1–16. https://doi.org/10.1080/24705357.2023.2176375

Cornacchia, L., Licci, S., Nepf, H., Folkard, A., van der Wal, D., van de Koppel, J., Puijalon, S., & Bouma, T. J. (2019). Turbulence-mediated facilitation of resource uptake in patchy stream macrophytes. *Limnology and Oceanography*, *64*(2), 714–727. https://doi.org/10.1002/LNO.11070

Cornacchia, L., van de Koppel, J., van der Wal, D., Wharton, G., Puijalon, S., & Bouma, T. J. (2018). Landscapes of facilitation: how self-organized patchiness of aquatic macrophytes promotes diversity in streams. *Ecology*, *99*(4), 832–847. https://doi.org/10.1002/ecy.2177

de Langre, E. (2008). Effects of Wind on Plants. *Annual Review of Fluid Mechanics*, *40*, 141–168. https://doi.org/10.1146/ANNUREV.FLUID.40.111406.102135

Ervine, D. A., Babaeyan-Koopaei, K., & Sellin, R. H. J. (2000). Two-Dimensional Solution for Straight and Meandering Overbank Flows. *Journal of Hydraulic Engineering*, *126*(9), 653–669. https://doi.org/10.1061/(ASCE)0733-9429(2000)126:9(653)

Feenstra, J. J., & Vertegaal, P. (1976). *De Dinkel: krom of recht?* (1ste druk). Nederlandse jeugdbond voor natuurstudie en de natuurbeschermingskommissie jeugdbonden voor natuurstudie. https://edepot.wur.nl/387759

Fernandes, J. N., Leal, J. B., & Cardoso, A. H. (2014). Improvement of the Lateral Distribution Method based on the mixing layer theory. *Advances in Water Resources*, *69*, 159–167. https://doi.org/10.1016/j.advwatres.2014.04.003

Fischer, H., List, J., Koh, C., Imberger, J., & Brooks, N. (1979). *Mixing in Inland and Coastal Waters* (1st Edition). CA: Academic Press.

Forman, R. T. T. (1995). Some general principles of landscape and regional ecology. *Landscape Ecology*, *10*(3), 133–142. https://doi.org/10.1007/BF00133027

Fraaije, R. G. A., Poupin, C., Jos, |, Verhoeven, T. A., Merel, |, Soons, B., Onderzoek, W., Toegepast, S., & Waterbeheer, O. (2019). Functional responses of aquatic and riparian vegetation to hydrogeomorphic restoration of channelized lowland streams and their valleys. *Journal of Applied Ecology*, *56*(4), 1007–1018. https://doi.org/10.1111/1365-2664.13326

Franca, M. J., Santos, B. O., Antico, F., & Ferreira, R. M. L. (2014). Quadrant analysis of coherent structures in open channel flows over mobile and immobile hydraulically rough beds. *ERCOFTAC Bull*, *100*, 29–36.

Ghisalberti, M., & Nepf, H. M. (2002). Mixing layers and coherent structures in vegetated aquatic flows. *Journal of Geophysical Research*, *107*(C2), 3011. https://doi.org/10.1029/2001JC000871

Goring, D. G., & Nikora, V. I. (2002). Despiking Acoustic Doppler Velocimeter Data. *Journal of Hydraulic Engineering*, *128*(1), 117–126. https://doi.org/10.1061/(ASCE)0733-9429(2002)128:1(117)

Ho, C., & Huerre, P. (1984). Perturbed Free Shear Layers. *Annual Review of Fluid Mechanics*, *16*(1), 365–422. https://doi.org/10.1146/annurev.fl.16.010184.002053

Hopkinson, L., & Wynn, T. (2009). Vegetation impacts on near bank flow. *Ecohydrology*, *2*(4), 404–418. https://doi.org/10.1002/ECO.87

Horstman, E. M., Bryan, K. R., Mullarney, J. C., Pilditch, C. A., & Eager, C. A. (2018). Are flow-vegetation interactions well represented by mimics? A case study of mangrove pneumatophores. *Advances in Water Resources*, *111*, 360–371. https://doi.org/10.1016/j.advwatres.2017.11.018

Huai, W. X., Zhang, J., Wang, W. J., & Katul, G. G. (2019). Turbulence structure in open channel flow with partially covered artificial emergent vegetation. *Journal of Hydrology*, *573*, 180–193. https://doi.org/10.1016/J.JHYDROL.2019.03.071

Huai, W., Xue, W., & Qian, Z. (2015). Large-eddy simulation of turbulent rectangular open-channel flow with an emergent rigid vegetation patch. *Advances in Water Resources*, *80*, 30–42. https://doi.org/10.1016/J.ADVWATRES.2015.03.006

Jalonen, J., & Järvelä, J. (2014). Estimation of drag forces caused by natural woody vegetation of different scales. *Journal of Hydrodynamics 2014 26:4*, *26*(4), 608–623. https://doi.org/10.1016/S1001-6058(14)60068-8

Jesson, M. A., Bridgeman, J., & Sterling, M. (2015). Novel software developments for the automated post-processing of high volumes of velocity time-series. *Advances in Engineering Software*, *89*, 36–42. https://doi.org/10.1016/j.advengsoft.2015.06.007

Jesson, M., Sterling, M., & Bridgeman, J. (2013). Despiking velocity time-series—Optimisation through the combination of spike detection and replacement methods. *Flow Measurement and Instrumentation*, *30*, 45–51. https://doi.org/10.1016/j.flowmeasinst.2013.01.007

Kalloe, S. A., Hofland, B., Antolínez, J. A. A., & van Wesenbeeck, B. K. (2022). Quantifying Frontal-Surface Area of Woody Vegetation: A Crucial Parameter for Wave Attenuation. *Frontiers in Marine Science*, *9*. https://doi.org/10.3389/fmars.2022.820846

Kean, J. W., & Smith, J. D. (2004). *Flow and boundary shear stress in channels with woody bank vegetation* (pp. 237–252). https://doi.org/10.1029/008WSA17

Kitsikoudis, V., Kirca, V. S. O., Yagci, O., & Celik, M. F. (2017). Clear-water scour and flow field alteration around an inclined pile. *Coastal Engineering*, *129*, 59–73. https://doi.org/10.1016/j.coastaleng.2017.09.001

Kitsikoudis, V., Yagci, O., & Kirca, V. S. O. (2020). Experimental analysis of flow and turbulence in the wake of neighboring emergent vegetation patches with different densities. *Environmental Fluid Mechanics*, *20*(6), 1417–1439. https://doi.org/10.1007/s10652-020-09746-6

Kitsikoudis, V., Yagci, O., Kirca, V. S. O., & Kellecioglu, D. (2016). Experimental investigation of channel flow through idealized isolated tree-like vegetation. *Environmental Fluid Mechanics*, *16*(6), 1283–1308. https://doi.org/10.1007/s10652-016-9487-7

Kolasa, J. (2014). Ecological boundaries: a derivative of ecological entities. *Web Ecology*, *14*(1), 27–37. https://doi.org/10.5194/we-14-27-2014

Ku, H. H. (1966). Notes on the use of propagation of error formulas. *Journal of Research of the National Bureau of Standards, Section C: Engineering and Instrumentation*, *70C*(4), 263. https://doi.org/10.6028/jres.070C.025

Kundu, P., Cohen, I., & Dowling, D. (2015). *Fluid Mechanics* (6th ed.). Academic Press.

Lambert, M. F., & Sellin, R. H. J. (1996). Discharge prediction in straight compound channels using the mixing length concept. *Journal of Hydraulic Research*, *34*(3), 381–394. https://doi.org/10.1080/00221689609498487

Landsemant für Natur Umwel und Verbraucherschutz Nordrhein-Westfalen. (2023). *Wasserstand des Pegels Gronau*. http://luadb.it.nrw.de/LUA/hygon/pegel.php?stationsname=Gronau&yAchse=Standard&nachSuche=&hoehe=468&breite=724&datum=2023-06-29&progn=&meindatum=29.06.2023&yAchse=Standard&erstesJahr=jaarlijkse+lijn&meifocus=&neuname=

Lightbody, A. F., & Nepf, H. M. (2006). Prediction of velocity profiles and longitudinal dispersion in salt marsh vegetation. *Limnology and Oceanography*, *51*(1), 218–228. https://doi.org/10.4319/LO.2006.51.1.0218

Liu, C., & Shan, Y. (2019). Analytical model for predicting the longitudinal profiles of velocities in a channel with a model vegetation patch. *Journal of Hydrology*, *576*, 561–574. https://doi.org/10.1016/j.jhydrol.2019.06.076

Liu, C., Yan, C., Shan, Y., & Guo, Y. (2022). An exponential-based model for predicting velocity fields in partially vegetated channels. *Journal of Hydraulic Research*, *60*(6), 864–879. https://doi.org/10.1080/00221686.2022.2067084

Liu, C., Yan, C., Sun, S., Lei, J., Nepf, H., & Shan, Y. (2022). Velocity, Turbulence, and Sediment Deposition in a Channel Partially Filled With a Phragmites australis Canopy. *Water Resources Research*, *58*(8). https://doi.org/10.1029/2022WR032381

Liu, D., Diplas, P., Fairbanks, J. D., & Hodges, C. C. (2008). An experimental study of flow through rigid vegetation. *Journal of Geophysical Research*, *113*(F4), F04015. https://doi.org/10.1029/2008JF001042

Liu, D., Valyrakis, M., & Williams, R. (2017). Flow Hydrodynamics across Open Channel Flows with Riparian Zones: Implications for Riverbank Stability. *Water 2017, Vol. 9, Page 720*, *9*(9), 720. https://doi.org/10.3390/W9090720

Liu, M.-Y., Huai, W.-X., Yang, Z.-H., & Zeng, Y.-H. (2020). A genetic programming-based model for drag coefficient of emergent vegetation in open channel flows. *Advances in Water Resources*, *140*, 103582. https://doi.org/10.1016/j.advwatres.2020.103582

Nepf, H., & Ghisalberti, M. (2008). Flow and transport in channels with submerged vegetation. *Acta Geophysica*, *56*(3), 753–777. https://doi.org/10.2478/s11600-008-0017-y

Nepf, H. M. (1999). Drag, turbulence, and diffusion in flow through emergent vegetation. *Water Resources Research*, *35*(2), 479–489. https://doi.org/10.1029/1998WR900069

Nepf, H. M. (2012a). Flow and Transport in Regions with Aquatic Vegetation. *Annual Review of Fluid Mechanics*, *44*(1), 123–142. https://doi.org/10.1146/annurev-fluid-120710-101048

Nepf, H. M. (2012b). Flow Over and Through Biota. *Treatise on Estuarine and Coastal Science*, *2*, 267–288. https://doi.org/10.1016/B978-0-12-374711-2.00213-8

Nepf, H. M. (2012c). Hydrodynamics of vegetated channels. *Journal of Hydraulic Research*, *50*(3), 262–279. https://doi.org/10.1080/00221686.2012.696559

Nezu, I., & Sanjou, M. (2008). Turburence structure and coherent motion in vegetated canopy open-channel flows. *Journal of Hydro-Environment Research*, *2*(2), 62–90. https://doi.org/10.1016/j.jher.2008.05.003

Nikora, V. (2010a). Hydrodynamics of aquatic ecosystems: An interface between ecology, biomechanics and environmental fluid mechanics. *River Research and Applications*, *26*(4), 367–384. https://doi.org/10.1002/rra.1291

Nikora, V. (2010b). Hydrodynamics of Aquatic Ecosystems: Current state, challenges, and prospects. *17th Australasian Fluid Mechanics Conference 2010*, 1–6.

Nortek. (2022). *The Comprehensive Manual - Velocimeters*. https://support.nortekgroup.com/hc/en-us/articles/360029839351-The-Comprehensive-Manual-Velocimeters

Parsheh, M., Fotis Sotiropoulos, ;, & Porté-Agel, F. (2010). Estimation of Power Spectra of Acoustic-Doppler Velocimetry Data Contaminated with Intermittent Spikes. *Journal of Hydraulic Engineering*, *136*(6), 368–378. https://doi.org/10.1061/(ASCE)HY.1943-7900.0000202

Plew, D. R. (2010). Depth-Averaged Drag Coefficient for Modeling Flow through Suspended Canopies. *Journal of Hydraulic Engineering*, *137*(2), 234–247. https://doi.org/10.1061/(ASCE)HY.1943-7900.0000300

Poggi, D., Katul, G. G., & Albertson, J. D. (2004). Momentum Transfer and Turbulent Kinetic Energy Budgets within a Dense Model Canopy. *Boundary-Layer Meteorology*, *111*(3), 589–614. https://doi.org/10.1023/B:BOUN.0000016502.52590.af

Przyborowski, Ł., Łoboda, A. M., & Bialik, R. J. (2019). Effect of two distinct patches of Myriophyllum species on downstream turbulence in a natural river. *Acta Geophysica*, *67*(3), 987–997. https://doi.org/10.1007/s11600-019-00292-4

Raupach, M. R., Finnigan, J. J., & Brunei, Y. (1996). Coherent eddies and turbulence in vegetation canopies: The mixing-layer analogy. *Boundary-Layer Meteorology*, *78*(3–4), 351–382. https://doi.org/10.1007/BF00120941

Rominger, J. T., & Nepf, H. M. (2011). Flow adjustment and interior flow associated with a rectangular porous obstruction. *Journal of Fluid Mechanics*, *680*, 636–659. https://doi.org/10.1017/jfm.2011.199

Rowiński, P., & Radecki-Pawlik, A. (2015). *Rivers – Physical, Fluvial and Environmental Processes* (P. Rowiński & A. Radecki-Pawlik, Eds.; 1st ed.). Springer International Publishing. https://doi.org/10.1007/978-3-319-17719-9

Sand-Jensen, K., & Vindbaek Madsen, T. (1992). Patch dynamics of the stream macrophyte, Callitriche cophocarpa. *Freshwater Biology*, *27*(2), 277–282. https://doi.org/10.1111/j.1365-2427.1992.tb00539.x

Schmitt, F. G. (2007). About Boussinesq's turbulent viscosity hypothesis: historical remarks and a direct evaluation of its validity. *Comptes Rendus Mécanique*, *335*(9–10), 617–627. https://doi.org/10.1016/J.CRME.2007.08.004

Schneider, C. A., Rasband, W. S., & Eliceiri, K. W. (2012). NIH Image to ImageJ: 25 years of image analysis. *Nature Methods 2012 9:7*, *9*(7), 671–675. https://doi.org/10.1038/nmeth.2089

Schoelynck, J., Creëlle, S., Buis, K., De Mulder, T., Emsens, W.-J., Hein, T., Meire, D., Meire, P., Okruszko, T., Preiner, S., Roldan Gonzalez, R., Silinski, A., Temmerman, S., Troch, P., Van Oyen, T., Verschoren, V., Visser, F., Wang, C., Wolters, J.-W., & Folkard, A. (2018). What is a macrophyte patch? Patch identification in aquatic ecosystems and guidelines for consistent delineation. *Ecohydrology & Hydrobiology*, *18*(1), 1–9. https://doi.org/10.1016/j.ecohyd.2017.10.005

Siniscalchi, F., Nikora, V. I., & Aberle, J. (2012). Plant patch hydrodynamics in streams: Mean flow, turbulence, and drag forces. *Water Resources Research*, *48*(1), 1513. https://doi.org/10.1029/2011WR011050

Stone, B. M., & Shen, H. T. (2002). Hydraulic Resistance of Flow in Channels with Cylindrical Roughness. *Journal of Hydraulic Engineering*, *128*(5), 500–506. https://doi.org/10.1061/(ASCE)0733-9429(2002)128:5(500)

Sukhodolov, A. N., & Sukhodolova, T. A. (2009). Case Study: Effect of Submerged Aquatic Plants on Turbulence Structure in a Lowland River. *Journal of Hydraulic Engineering*, *136*(7), 434–446. https://doi.org/10.1061/(ASCE)HY.1943-7900.0000195

T. Tsujimoto, T. Kitamura, & T. Okada. (1991). *Turbulent Structure of Flow over Rigid Vegetation-Covered Bed in Open Channels*.

Tanino, Y., & Nepf, H. M. (2008). Laboratory Investigation of Mean Drag in a Random Array of Rigid, Emergent Cylinders. *Journal of Hydraulic Engineering*, *134*(1), 34–41. https://doi.org/10.1061/(ASCE)0733-9429(2008)134:1(34)

Tinoco, R. O., San Juan, J. E., & Mullarney, J. C. (2020). Simplification bias: lessons from laboratory and field experiments on flow through aquatic vegetation. *Earth Surface Processes and Landforms*, *45*(1), 121–143. https://doi.org/10.1002/ESP.4743

Truong, S. H., & Uijttewaal, W. S. J. (2019). Transverse Momentum Exchange Induced by Large Coherent Structures in a Vegetated Compound Channel. *Water Resources Research*, *55*(1), 589–612. https://doi.org/10.1029/2018WR023273

Uijttewaal, W. S. J., & Booij, R. (2000). Effects of shallowness on the development of free-surface mixing layers. *Physics of Fluids*, *12*(2), 392–402. https://doi.org/10.1063/1.870317

Umeyama, M., & Gerritsen, F. (1992). Velocity Distribution in Uniform Sediment-Laden Flow. *Journal of Hydraulic Engineering*, *118*(2), 229–245. https://doi.org/10.1061/(ASCE)0733-9429(1992)118:2(229)

van Prooijen, B. C., Battjes, J. A., & Uijttewaal, W. S. J. (2005). Momentum Exchange in Straight Uniform Compound Channel Flow. *Journal of Hydraulic Engineering*, *131*(3), 175–183. https://doi.org/10.1061/(ASCE)0733-9429(2005)131:3(175)

Van Rijn, L. C. (1990). *Principles of fluid flow and surface waves in rivers, estuaries, seas and oceans* (2011th ed., Vol. 12). Aqua Publications.

Villota, S. U., Ghisalberti, M., Philip, J., & Branson, P. (2023). Characterizing the Three-Dimensional Flow in Partially Vegetated Channels. *Water Resources Research*, *59*(1), e2022WR032570. https://doi.org/10.1029/2022WR032570

Vogel, S. (2020). *Life in Moving Fluids*. Princeton University Press. https://doi.org/10.2307/j.ctvzsmfc6

Wallace, J. M. (2016). Quadrant Analysis in Turbulence Research: History and Evolution. *Annual Review of Fluid Mechanics*, *48*(1), 131–158. https://doi.org/10.1146/annurev-fluid-122414-034550

Welch, P. (1967). The use of fast Fourier transform for the estimation of power spectra: A method based on time averaging over short, modified periodograms. *IEEE Transactions on Audio and Electroacoustics*, *15*(2), 70–73. https://doi.org/10.1109/TAU.1967.1161901

White, B. L., & Nepf, H. M. (2007). Shear instability and coherent structures in shallow flow adjacent to a porous layer. *Journal of Fluid Mechanics*, *593*, 1–32. https://doi.org/10.1017/S0022112007008415

White, B. L., & Nepf, H. M. (2008). A vortex-based model of velocity and shear stress in a partially vegetated shallow channel. *Water Resources Research*, *44*(1), 1412. https://doi.org/10.1029/2006WR005651

Widdows, J., Pope, N., & Brinsley, M. (2008). Effect of Spartina anglica stems on near-bed hydrodynamics, sediment erodability and morphological changes on an intertidal mudflat. *Marine Ecology Progress Series*, *362*, 45–57. https://doi.org/10.3354/meps07448

Yagci, O., Celik, M. F., Kitsikoudis, V., Ozgur Kirca, V. S., Hodoglu, C., Valyrakis, M., Duran, Z., & Kaya, S. (2016). Scour patterns around isolated vegetation elements. *Advances in Water Resources*, *97*, 251–265. https://doi.org/10.1016/J.ADVWATRES.2016.10.002

Yan, C., Shan, Y., Sun, W., Liu, C., & Liu, X. (2020). Modeling the longitudinal profiles of streamwise velocity in an open channel with a model patch of vegetation. *Environmental Fluid Mechanics*, *20*(6), 1441–1462. https://doi.org/10.1007/s10652-020-09747-5

Zong, L., & Nepf, H. (2010). Flow and deposition in and around a finite patch of vegetation. *Geomorphology*, *116*(3–4), 363–372. https://doi.org/10.1016/J.GEOMORPH.2009.11.020

Zong, L., & Nepf, H. (2012). Vortex development behind a finite porous obstruction in a channel. *Journal of Fluid Mechanics*, *691*, 368–391. https://doi.org/10.1017/JFM.2011.479

Appendices

Appendix A – Longitudinal Development of Streamwise flow velocities aligned and staggered configurations.

Aligned Configurations

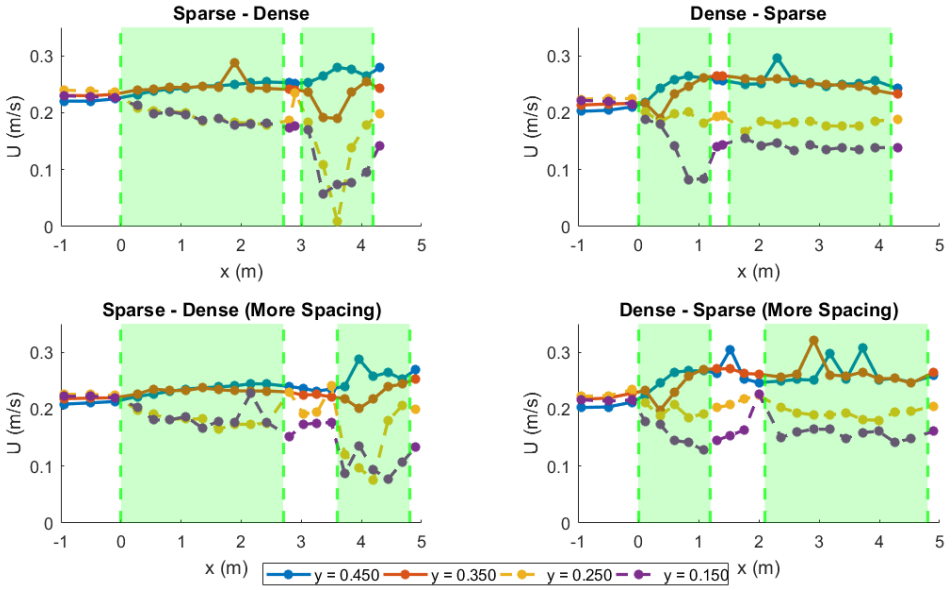

Figure 35 Longitudinal development of the streamwise depth-averaged flow velocities of the aligned configurations (Run B, Run D, Run F, Run G). The flow direction is from left to right. The solid lines represent the two longitudinal profiles along the adjacent unvegetated area. The dashed lines are the longitudinal profile along the sparse and dense vegetation patch. The locations of the vegetation patches are indicated with green shaded rectangles.

Staggered Configurations

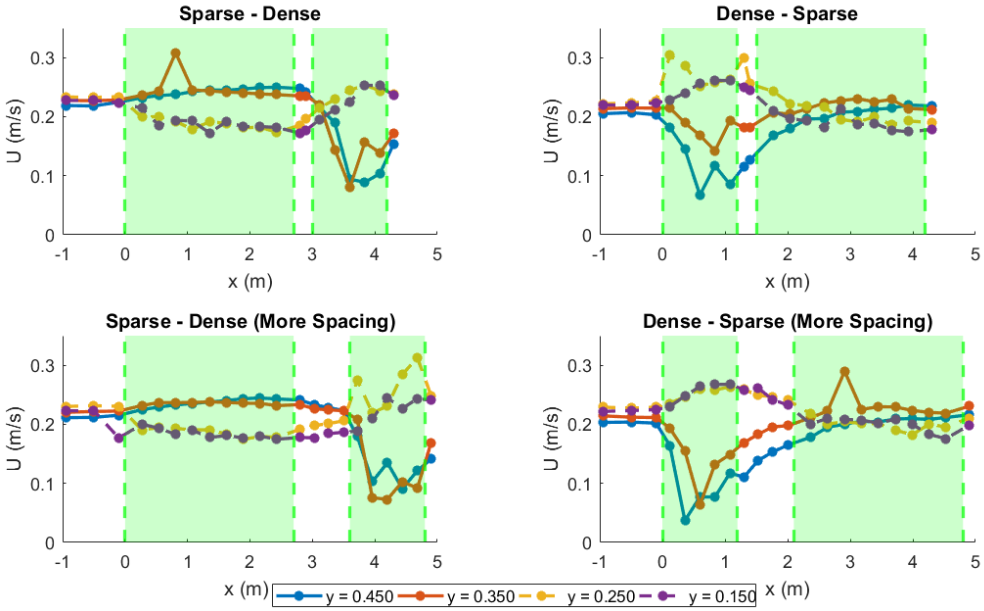

Figure 36 Longitudinal Development of the streamwise flow velocities of the staggered configurations (Run A, Run C, Run E, Run H). The flow direction is from left to right. The solid lines represent the two longitudinal profiles along the dense vegetation patch. The dashed lines are the longitudinal profiles along the sparse vegetation patch. The locations of the vegetation patches are indicated with green shaded rectangles.